

## ABSTRACT

PANDYA, NAIMISH SANJAYBHAI. Internal Cooling of Gas Turbine Blade with High Performance Features Under High Reynolds Number Condition. (Under the direction of Dr. Srinath V. Ekkad).

As modern gas turbine engines advance toward higher thermal efficiencies, the need for effective internal cooling strategies becomes increasingly critical to ensure blade durability and system reliability under extreme thermal loads. This study presents a comprehensive numerical and experimental investigation into the thermal-hydraulic performance of advanced rib and fin turbulator configurations designed to enhance internal cooling within turbine blade mid-core passages. The work targets extremely high Reynolds numbers ( $Re = 100,000$  to  $600,000$ ), representative of real-world operating conditions in both land-based and aviation engines.

The study begins with high-fidelity Computational Fluid Dynamics (CFD) simulations using the  $k-\varepsilon$  turbulence model family to evaluate conventional and modified rib geometries. Among the evaluated designs, the Broken V Rib configuration emerged as the most thermally efficient, delivering up to 26% greater heat transfer compared to previously benchmarked W-shaped ribs, while maintaining relatively moderate pressure penalties. To further explore performance improvements, three novel turbulator geometries—Continuous Chevron Pattern Fins (CCPF), V-Shaped Double Broken Ribs (VSDBR), and Broken Chevron Pattern Fins (BCPF)—were analyzed using the Realizable  $k-\varepsilon$  model. These simulations, validated by experimental data, demonstrated that VSDBR provided the highest enhancement ( $Nu/Nu_0 \approx 2.4$ ), albeit at a pressure drop increase of up to 34%. In contrast, BCPF showed balanced thermal-hydraulic performance with lower friction losses and a THP consistently greater than one, especially at high Reynolds numbers.

Based on these CFD insights, an experimental campaign was designed and executed in three phases to systematically optimize the rib geometry. In the first phase, continuous and broken V-rib configurations were compared at three angles—30°, 45°, and 60°—with fixed rib height ( $e/D_h = 1/20$ ) and pitch ratio ( $p/e = 10$ ). The results confirmed that broken ribs significantly outperformed their continuous counterparts across all angles, particularly at 45°, due to enhanced flow disruption and mixing. The second phase focused on identifying the optimal rib height by testing the best-performing rib structure and angle from Phase 1 at four different blockage ratios ( $e/D_h = 1/10, 1/20, 1/25, \text{ and } 1/30$ ), revealing that  $e/D_h = 1/20$  offered the best trade-off between heat transfer and pressure drop. The third phase investigated the impact of pitch by testing two values ( $p/e = 10$  and 15) with the previously optimized structure, angle, and height. The tighter pitch ( $p/e = 10$ ) was found to maintain stronger flow reattachment and superior thermal-hydraulic performance.

All experiments were conducted under steady-state forced convection using infrared thermography within a reduced-blockage rectangular duct. The findings from the experimental work closely aligned with the CFD predictions, confirming that broken rib configurations consistently yield higher heat transfer coefficients and favorable thermal-hydraulic performance ( $\text{THP} > 1$ ) across all tested Reynolds numbers.

This integrated study provides deep insights into the role of rib structure, angle, height, and pitch in governing flow dynamics, heat transfer, and pressure loss in high-speed internal cooling channels. The results offer practical design guidance for improving cooling effectiveness in advanced turbine blade systems and highlight the importance of CFD-guided experimental validation in the development of next-generation thermal management strategies.

© Copyright 2025 by Naimish Sanjaybhai Pandya

All Rights Reserved

Internal Cooling of Gas Turbine Blade with High Performance Features Under High Reynolds  
Number Condition

by  
Naimish Sanjaybhai Pandya

A dissertation submitted to the Graduate Faculty of  
North Carolina State University  
in partial fulfillment of the  
requirements for the degree of  
Doctor of Philosophy

Mechanical Engineering

Raleigh, North Carolina  
2025

APPROVED BY:

---

Dr Srinath V. Ekkad  
Committee Chair

---

Dr Sajjad Bigham

---

Dr. Tim Horn

---

Dr Cristopher Rocks

## DEDICATION

I offer my PhD Thesis with deep reverence to my Guru, H.D.H. Pramukh Swami Maharaj, and his current successor, H.D.H. Mahant Swami Maharaj, whose blessings and spiritual guidance have illuminated my path. Their teachings have inspired me not only to grow as a researcher but also to strive toward becoming a better human being.

This work is also equally dedicated to my parents, who have sacrificed everything to ensure I receive an education and have the opportunity to establish myself in this world as a researcher. Their unwavering love, hard work, and constant support have shaped the foundation of who I am, and I will always carry their strength and values with me. I also dedicate this thesis to my beloved grandparents, with whom I shared a deep emotional bond. They raised me with the highest moral values and instilled in me a strong sense of pride, ethics, and humility—gifts that continue to guide me every day.

Without the blessings of my Gurus and the tireless sacrifices of my parents, none of this would have been possible. This journey, and this thesis, are as much theirs as they are mine.

## **BIOGRAPHY**

Naimish was born in Porbandar, located in the western Indian state of Gujarat. He earned his bachelor's degree in mechanical engineering from Gujarat Technological University in 2017. In Fall 2021, he began his Ph.D. in Mechanical Engineering at North Carolina State University, where he is pursuing research under the guidance of Dr. Srinath Ekkad in the field of heat transfer. Throughout his doctoral studies, Naimish has focused on exploring the fundamentals of heat transfer in stationary systems and applying those principles to a wide range of engineering applications—from advanced thermal management for semiconductor cooling to internal cooling in gas turbine engines. His work bridges theoretical understanding with practical innovation across high-performance thermal systems. Outside of his research, Naimish enjoys gardening, volunteering at community events and temples, and spending quality time with family and friends.

## ACKNOWLEDGMENTS

My journey toward earning a doctoral degree would not have been possible without the unwavering support and encouragement of many people. Though words often fall short in capturing the depth of my gratitude, I would like to take this opportunity to express my sincere appreciation to all those who have been part of this journey.

First and foremost, I am deeply grateful to my advisor, Dr. Srinath Ekkad, for giving me the opportunity to work under his guidance. His trust in my abilities, his mentorship, and the academic freedom he provided have been instrumental in shaping my research and personal growth. His belief in me encouraged me to take initiative, explore ideas that excited me, and embrace a wide range of responsibilities. His support created a sense of responsibility and ownership in my work, and I know many of my lab mates would echo this feeling.

I would also like to thank my doctoral committee members—Dr. Sajjad Bigham, Dr. Tim Horn, and Dr. Cris Rocks—for generously offering their time, thoughtful insights, and constructive feedback. Their guidance has played a meaningful role in shaping my research and helping me grow both academically and personally. I'm also grateful to my former advisor, Dr. Arun Kota, who believed in my potential and welcomed me into his lab during the early stages of my Ph.D. journey at NC State and, I truly appreciate the trust he placed in me.

To my lab mates, thank you for being more than just colleagues. The thoughtful (and sometimes intense) discussions we've shared, both in and outside the lab, have helped me think critically and brought out the best in me. I am equally thankful to all other graduates and undergraduate students in our lab—working with you has been a pleasure.

To my friends, thank you for the laughter, motivation, and meaningful conversations that have shaped my journey. Some of you were the very reason I found the courage to pursue a Ph.D. in another country, and for that, I am forever grateful.

I'd also like to thank the professors at NC State whose courses I took—your teachings have been foundational to my growth. A special thanks goes to Mr. Vince Chicarelli, whose skill and patience in fabricating key components of my experimental setups were essential to this work. I am grateful to the Mechanical and Aerospace Engineering Department staff for your behind-the-scenes work that keeps everything running and supports students every day.

To my parents, Sanjay and Riddhi Pandya—no words can fully express the depth of my gratitude. You have overcome unimaginable challenges—both financial and social—to support my education and dreams. I owe everything to you. To my grandparents, who are no longer with us but whose values still guide me, you gave me a moral foundation that I carry with pride. I know you're watching over me with pride. To the BAPS community, thank you for being a home away from home. Your warmth and support over the past 12 years have meant the world to me, especially when I was far from my family and parents.

I've had the privilege to learn from and work with many mentors, teachers, supervisors, and peers along the way. I may not be able to name everyone, but I carry a deep sense of gratitude for each and every one of you. Your encouragement has made a lasting impact on me, and I hope to carry your support forward by making you proud.

— **Naimish Sanjaybhai Pandya**

## TABLE OF CONTENTS

|                      |     |
|----------------------|-----|
| ABSTRACT.....        | 1   |
| DEDICATION.....      | ii  |
| BIOGRAPHY.....       | iii |
| ACKNOWLEDGMENTS..... | iv  |
| Appendix A.....      | 91  |

## LIST OF TABLES

|  |    |
|--|----|
| Table 1: Reynolds number for tested each continuous ribs .....                 | 39 |
| Table 2: Reynolds number for tested each broken ribs.....                      | 42 |
| Table 3: Reynolds number for tested each broken ribs placed at 45° angle ..... | 51 |
| Table 1: Mesh parameters.....  | 71 |

## LIST OF FIGURES

|            |   |    |
|------------|---|----|
| Figure 1:  | Schematic of computational domain .....   | 5  |
| Figure 2:  | Mesh generated for this study .....   | 7  |
| Figure 3:  | Normalized overall Nusselt number for different grid .....  | 7  |
| Figure 4:  | Comparison of Numerically Predicted Normalized Nusselt Number with<br>Experimental Data for V-Shaped 45° Rib Configuration .....  | 8  |
| Figure 5:  | Design configurations of novel structures, all placed at a 45° angle with a rib height<br>to hydraulic diameter ratio $e/D_h=1/20$ : (a) Broken V rib, (b) Double broken V rib, (c) Broken V<br>rib with fins, and (d) V shaped fin array ..... | 10 |
| Figure 6:  | Normalized Nusselt number (left) and temperature (right) distribution at bottom wall<br>for broken V rib features on Reynolds number ranging from 100k to 400k .....  | 13 |
| Figure 7:  | Normalized Nusselt number (left) and temperature (right) distribution at bottom wall<br>for Double broken V rib features on Reynolds number ranging from 100k to 400k.....  | 14 |
| Figure 8:  | Normalized Nusselt number (left) and temperature (right) distribution at bottom wall<br>for broken V rib with fin features on Reynolds number ranging from 100k to 400k.....  | 15 |
| Figure 9:  | Normalized Nusselt number (left) and temperature (right) distribution at bottom wall<br>for v shape fin array features on Reynolds number ranging from 100k to 400k .....   | 16 |
| Figure 10: | Streamlines near the bottom wall for various geometries at $Re = 400k$ , showing flow<br>from inlet (bottom) to outlet (top) parallel to the wall in the test section. ....   | 17 |
| Figure 11: | Comparison of normalized Nusselt number for this study and different features from<br>Zhang at al. [14]......   | 19 |
| Figure 12: | Comparison of normalized friction factor for this study and different features from<br>Zhang at al. [14]......  | 20 |
| Figure 13: | Variation of Thermal hydraulic performance variation with Reynolds number for this<br>study and different structures from Zhang at al. [14]. ....   | 21 |
| Figure 14: | Schematic of experimental setup.....  | 32 |
| Figure 15: | Actual Experimental setup photograph .....  | 33 |
| Figure 16: | V shaped Rib turbulator photograph have been used in this study (a) Broken 60°, (b)<br>Broken 45°, (c) Broken 30°, (d) Continuous 60°, (e) Continuous 45°, (f) Continuous 30°. ....   | 36 |
| Figure 17: | Detailed normalized Nusselt number distribution in smooth wall from left to right at<br>four different Reynolds numbers, $Re_1, Re_2, Re_3, Re_4$ .....   | 38 |

|  |    |
|--|----|
| Figure 18: The local Nusselt number ratio for different regions in the smooth rectangular channel  | 39 |
| Figure 19: Detailed normalized Nusselt number distribution in (a) 30° traditional continuous ribs, (b) 45° traditional continuous ribs, (c) 60° traditional continuous ribs on bottom wall from left to right at four different Reynolds numbers, Re1, Re2, Re3, Re4.....  | 41 |
| Figure 20: Detailed normalized spanwise Nusselt number distribution in (a) 30° traditional continuous ribs, (b) 45° traditional continuous ribs, (c) 60° traditional continuous ribs on bottom wall from left to right at four different Reynolds numbers, Re1, Re2, Re3, Re4. ....  | 41 |
| Figure 21: Detailed normalized Nusselt number distribution in (a) 30° broken ribs, (b) 45° broken ribs, (c) 60° broken ribs on bottom wall from left to right at four different Reynolds numbers, Re1, Re2, Re3, Re4. ....   | 43 |
| Figure 22: Detailed normalized spanwise Nusselt number distribution in (a) 30° broken ribs, (b) 45° broken ribs, (c) 60° broken ribs on bottom wall from left to right at four different Reynolds numbers, Re1, Re2, Re3, Re4. ....  | 43 |
| Figure 23: Comparison of overall Nusselt number enhancement.....   | 44 |
| Figure 24: Comparison of overall Frictional losses.....  | 45 |
| Figure 25: Variation in Thermal hydraulic performance with Reynolds number .....   | 46 |
| Figure 26: Rib turbulator configurations evaluated in this study from left to right, the rib height-to-hydraulic diameter ratios ( $e/D_h$ ) are 1/10, 1/20, 1/25, and 1/30. ....  | 50 |
| Figure 27: Detailed normalized Nusselt number distributions on the bottom wall for 45° broken V-shaped ribs at three rib height-to-hydraulic diameter ratios: (a) $e/D_h = 1/10$ , (b) $e/D_h = 1/25$ , and (c) $e/D_h = 1/30$ . Contours are shown from left to right for four Reynolds numbers: Re <sub>1</sub> , Re <sub>2</sub> , Re <sub>3</sub> , and Re <sub>4</sub> . .... | 52 |
| Figure 28: Normalized Nusselt number distributions on the bottom wall for 45° broken V-shaped ribs with $e/D_h = 1/25$ and pitch-to-height ratio $p/e = 4$ . Results are shown from left to right for Reynolds numbers: 102,157; 200,304; 303,309; and 399,993. ....   | 53 |
| Figure 29: All combined geometry and normalized Nusselt number as a function of Reynolds number  | 54 |
| Figure 30: All combined geometry and normalized frictional losses as a function of Reynolds number   | 55 |
| Figure 31: THP for All combined geometry as a function of Reynolds number.....   | 56 |

|   |    |
|---|----|
| Figure 32: Feature configuration .....  | 66 |
| Figure 33: Computational mesh used for this study .....   | 68 |
| Figure 34: Grid Independent test .....  | 71 |
| Figure 35: Comparison of Numerically Predicted Normalized Nusselt Number with<br>Experimental Data for VSDBR features.....                                | 72 |
| Figure 36: Experimental data for Spanwise averaging of normalized Nusselt number for<br>VSDBR features.....   | 73 |
| Figure 37: Evaluation of pressure drop: Experimental measurements vs. numerical predictions<br>73   |    |
| Figure 38: Normalized Nusselt number as a function of different Reynolds number. ....   | 74 |
| Figure 39: Normalized Nusselt number contours for (a) CCPF (b) VSDBR (c) BCPF design for<br>three different Reynolds numbers. ....                        | 75 |
| Figure 40: Normalized Nusselt number comparison for three different features tested on (1)<br>100k, (b) 300k and (c) 600k Reynolds number comparison..... | 77 |
| Figure 41: Flow path and velocity distribution on different featured geometry on $Re = 100k$ . .  | 78 |
| Figure 42: Flow path and velocity distribution on different featured geometry on $Re = 300k$ . .  | 79 |
| Figure 43: Flow path and velocity distribution on different featured geometry on $Re = 600k$ . .  | 80 |
| Figure 44: frictional losses (normalized friction) as a function of Reynolds number for three<br>different tested geometry .....                          | 80 |
| Figure 45: Thermal hydraulic performance for the tested design on a wide range of Reynolds<br>number conditions.....                                      | 81 |

## CHAPTER 1

Heat transfer and fluid flow analysis in a square ribbed channel at high Reynolds numbers for gas turbine blade cooling: A numerical approach

Naimish Pandya<sup>a</sup>, Srinath V. Ekkad<sup>a,\*</sup>

<sup>a</sup>Department of Mechanical and Aerospace engineering, North Carolina State University,  
Raleigh, NC USA

Abstract:

In this study, the heat transfer and frictional characteristics of four novel rib configurations, namely Broken V Rib, Double Broken V Rib, Broken V Rib with Fins, and V Shaped Fin Array were numerically investigated on a high-Reynolds-number internal cooling channel. The rib geometries were positioned at a 45° angle to the flow, with a rib pitch-to-height ratio ( $p/e$ ) of 16 and a rib-height-to-hydraulic-diameter ratio ( $e/D_h$ ) of 1/20. High Reynolds numbers ranging from 100,000 to 400,000 were studied to evaluate performance of these rib configurations. Computational fluid dynamics (CFD) simulations were performed using the RNG k- $\epsilon$  turbulence model in ANSYS Fluent. The heat transfer and flow characteristics were analyzed to understand the interaction between rib-induced secondary flows and their effect on heat transfer enhancement. The Broken V Rib configuration exhibited a 26% higher heat transfer rate compared to W-shaped ribs in reference and a 59% improvement over rib-with-fin configurations. In addition to its enhanced heat transfer performance, the Broken V Rib configuration maintained low frictional losses, making it the most thermally efficient design. The Double Broken V Rib and Rib with Fin configurations showed moderate heat transfer performance but showed higher pressure penalties. Overall, the Broken V Rib was identified as the most effective for internal cooling in gas turbine applications, providing an optimal balance between heat transfer enhancement and frictional losses operating particularly at high Reynolds number condition for turbine blade mid core passages.

Keywords: High Reynolds number, Internal cooling channels, Gas turbine Heat Transfer, CFD, Internal flow

## 1. Introduction

The efficient cooling of gas turbine blades is a crucial factor in improving the performance and reliability of gas turbine engines, particularly under high-temperature and pressure conditions. Higher operational temperatures can significantly enhance engine efficiency, but they also demand advanced internal cooling mechanisms. Various internal cooling strategies have been developed to address these challenges, including jet impingement for leading-edge cooling, pin fins for trailing-edge cooling, and rib turbulators for mid-core cooling. Among these, rib turbulators have attracted significant attention due to their ability to augment heat transfer within the internal passages of turbine blades particularly in mid core region. The performance of ribbed surfaces is influenced by key geometrical parameters such as the rib height-to-hydraulic diameter ratio ( $e/D_h$ ), rib pitch-to-height ratio ( $p/e$ ), and channel length-to-hydraulic diameter ratio ( $L/D_h$ ), all of which critically affect the thermal and hydraulic performance of rib-roughened passages and well summarized by Han et al. [1].

Significant research has focused on the optimization of rib geometries to maximize heat transfer enhancement while minimizing pressure losses. Early work by Han and Zhang [2] demonstrated that broken ribs, particularly V-shaped configurations, can significantly enhance heat transfer compared to continuous ribs, albeit with a corresponding increase in pressure drop. Ekkad and Han [3] extended this investigation by mapping heat transfer distributions in ribbed square channels, showing that rib orientation, especially under high Reynolds number ( $Re$ ) conditions, plays a crucial role in determining thermal performance. Kamali and Binesh [4] later investigated the effects of rib shape on heat transfer and flow friction in square ducts. Their study highlighted that specific rib geometries significantly affect both thermal performance and pressure losses, with certain configurations outperforming others depending on flow conditions. Rallabandi et al. [5] focused on ribbed channels with  $45^\circ$  ribs and provided detailed correlations between heat transfer and pressure drop for square channels at high Reynolds numbers. Alam et al. [6] reviewed various turbulator designs for heat transfer augmentation in air ducts, offering a comprehensive overview of designs for turbulent flow regimes and highlighting the effectiveness of ribbed surfaces in enhancing heat transfer. Mhetras et al. [7] extended this work by examining heat transfer and pressure losses in high-aspect-ratio channels under large Reynolds numbers, providing further insights into how channel geometry impacts the overall cooling system's efficiency. Rallabandi et al. [8,9] continued their investigation into ribbed channels, specifically focusing on

45° round-edged ribs and serpentine coolant passages with ribbed walls, showing how rib geometries can enhance heat transfer in more complex flow systems. More recent studies have explored advanced rib configurations.

Singh et al. [10] investigated heat transfer and fluid flow in square ducts utilizing criss-cross rib patterns. The criss-cross ribs were found to induce strong secondary flows and promote the mixing of fluid layers, leading to enhanced heat transfer. Their results showed a 25% increase in the Nusselt number compared to smooth ducts, attributed to the disruption of the thermal boundary layer. However, this improvement came with a significant 30% increase in friction factor, demonstrating the trade-off between heat transfer enhancement and pressure losses. The study concluded that criss-cross ribs are effective for applications where heat transfer is the primary concern, but hydraulic efficiency may be compromised. Singh et al. [11] explored the thermal and flow behavior in a two-pass rib-roughened square duct with developing flow. The observations revealed that the two-pass configuration, coupled with ribbed surfaces, generated strong recirculation zones that enhanced mixing and disrupted the boundary layer. Quantitatively, the study demonstrated a 35% increase in the local Nusselt number in the first pass, followed by a moderate 15% enhancement in the second pass. This is attributed to the fact that in the second pass, flow reattachment and stabilization reduce the turbulent mixing, thus slightly lowering the overall heat transfer. The friction factor was observed to increase by 25%, highlighting the additional pressure drop induced by the ribs. Another numerical study have been carried out by Ravi et al. [12]. The authors focused on simulating turbulent flow and heat transfer in two-pass ribbed channels. The Nusselt number was observed to increase by 40% in channels with optimized rib spacing, compared to smooth channels. However, the study also reported a 35% rise in the friction factor, indicating that the improved thermal performance comes at the cost of increased pressure drop. The study recommended optimizing rib spacing ( $p/e$ ) and rib height-to-hydraulic diameter ratio ( $e/D_h$ ) to maximize heat transfer while minimizing hydraulic losses. Furthermore, the simulations revealed that smaller rib pitch-to-height ratios provided better heat transfer uniformity across the channel, although they also resulted in higher pressure penalties. Berber et al. [13] estimated forced heat convection in rectangular channels with curved-winglet vortex generators. This investigation into vortex generators opened a new area of improving heat transfer by introducing flow disruptions, which generated vortices to enhance convective heat transfer in channels. Zhang et al. [14] conducted an important study on rib turbulators at very high Reynolds

numbers, emphasizing the challenge of balancing thermal enhancement and frictional losses, especially in extreme operational conditions. Xiong et al. [15] introduced improvements to internal cooling performance by using rhombus-patterned biomimetic ribs. This bio-inspired approach was unique in that it replicated natural patterns for enhanced fluid mixing and heat transfer, offering an innovative take on rib geometries for cooling channels.

The characterization of heat transfer mechanisms at high Reynolds numbers is essential for improving the thermal performance of large-scale power systems like land-based gas turbines. The flow inside the cooling channels for these large airfoils often operate at Reynolds numbers above 100,000, reaching up to 1 million in some cases. However, most existing studies have focused on lower Reynolds numbers, typically below 100,000. As a result, there is not much information available on the complex fluid dynamics and heat transfer behaviors at higher Reynolds number flow regimes, where turbulence plays the significant role. To address this gap, the present study is focused on higher Reynolds numbers conditions inside ribbed channels.

Prior research shows the using a V shaped feature particularly on 45° angle significantly increases thermal performance in the single and double pass channels for gas turbine blade internal cooling [16,17]. Thus primary goal is to examine the heat transfer enhancement and fluid flow mechanisms in rib-roughened channels under extreme high Reynolds condition by extending our previous work with novel features [14]. This novel combination of rib features to explore at high Reynolds numbers are studied using CFD analysis. Four designs have been studied: Broken V rib, Broken double V rib, Broken V rib with fins and V shaped Fin array placed at the 45° angle of attack and maintaining constant feature height at  $e/D_h = 1/20$ . The results are focused on providing an overall cooling effectiveness understanding for these rib configurations at high Reynolds numbers.

## 2. Computational setup

This section provides a comprehensive overview of the computational methodology, covering key aspects such as the computational domain, grid generation, solver settings, turbulence modeling, and applied boundary conditions.

### 2.1. Turbulence model

The computational domain utilized for the numerical simulations in this study is depicted in Figure 1, with names of the channel walls and features inside the duct. The numerical simulations were performed using the commercial solver ANSYS Fluent 2022 R2. The solution of the steady-state Reynolds-Averaged Navier-Stokes (RANS) equations employed second-order discretization schemes, considering an incompressible working fluid, and utilizing a pressure-based solver. The pressure-velocity coupling utilized the SIMPLE algorithm. Acknowledging insights from diverse computational studies in literature, RANS models were deemed proficient in accurately predicting flow and heat transfer in a square channel.

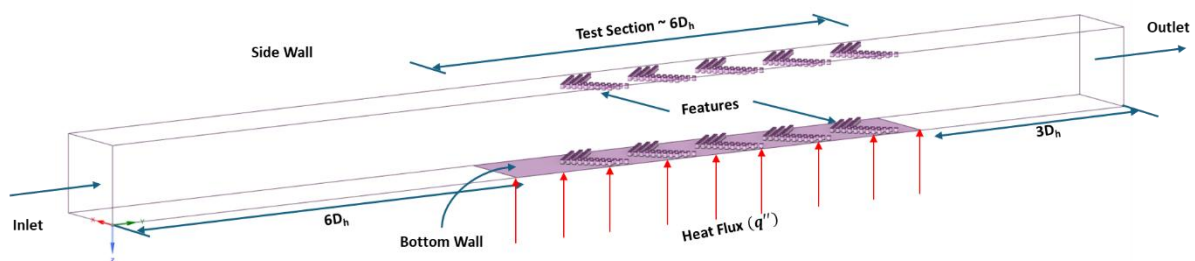


Figure 1: Schematic of computational domain

In this study, computational simulations were carried out using the commercial computational fluid dynamics (CFD) software, ANSYS Fluent 2022R2, to model the flow behavior. A 3D steady-state analysis was conducted, utilizing a pressure-based solver to resolve the governing equations for turbulent flow. The turbulence was modeled using the realizable  $k-\epsilon$  (RKE) model with enhanced wall treatment. To account for flow separation along the duct passage, features such as thermal effects and corner correction were activated in this Reynolds-Averaged Navier-Stokes (RANS) model. This allowed for improved prediction of flow separation and reattachment,

particularly behind rib structures and in complex flow regions. The RKE model has been shown to perform effectively in such scenarios [18,19]. Convergence of the solution was determined by monitoring the residuals of several governing equations. The convergence criteria were set to  $10^{-5}$  for the continuity, momentum, and turbulent transport equations, while a more stringent criterion of  $10^{-8}$  was applied to the energy equation. Additionally, the average bottom wall temperature was continuously monitored throughout the simulation to ensure the solution achieved a steady-state phase and stable convergence. This methodology ensured an accurate representation of the turbulent flow behavior and associated thermal effects within the simulated system, providing reliable and physically meaningful results.

## 2.2. Mesh Refinement and Grid Selection

To ensure the accurate capture of the boundary layer and near-wall flow physics, a very fine mesh was generated near the bottom wall and features, which is the main area of interest, using the Fluent Meshing software. A face size function was employed near the walls and key features to accurately capture the steep velocity profile and boundary layer phenomena. To accurately model the complex ribbed geometry, unstructured meshes were used, with refinement concentrated near the boundary layer. As shown in Figure 2, very fine mesh elements and 12-15 inflation layers were applied to all four walls within the computational domain, which was modeled exclusively as a fluid domain. Furthermore, the growth rate for the very fine cells near the features was selected to 1.1, ensuring that the volume of each adjacent cell does not differ significantly from the previous one, which is crucial for accurately capturing near-wall physics. In all cases, the  $y^+$  value was maintained below 5, which is essential for the performance of this turbulence model [20].

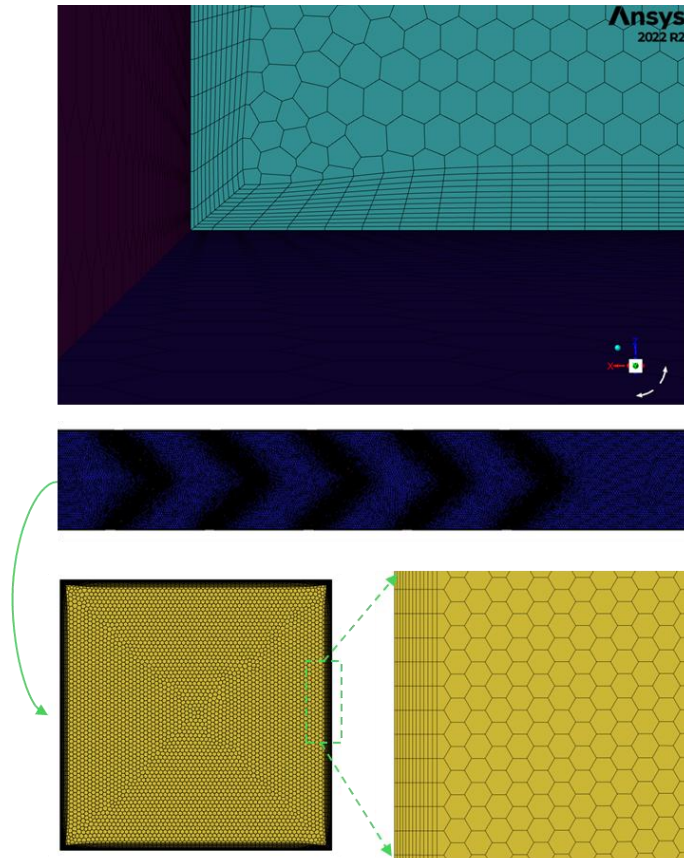


Figure 2: Mesh generated for this study

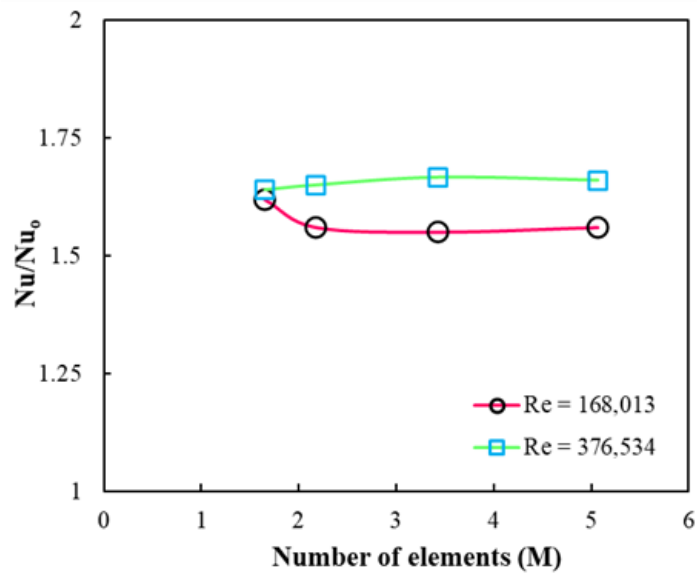


Figure 3: Normalized overall Nusselt number for different grid

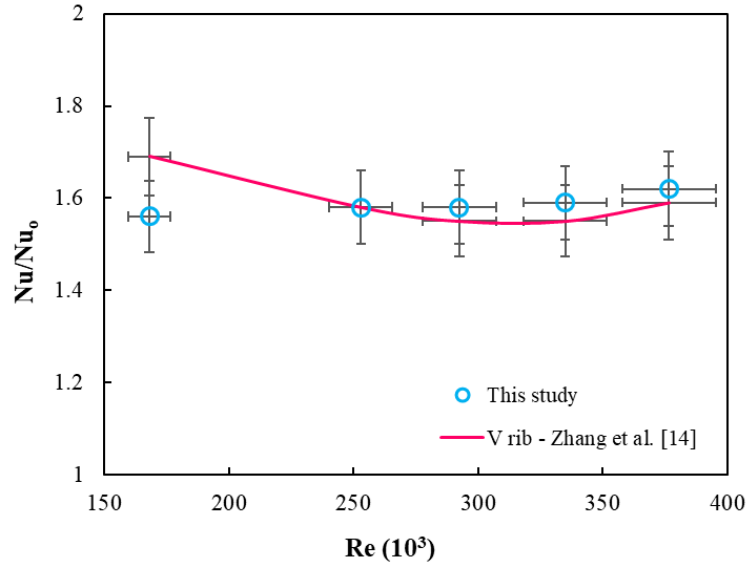


Figure 4: Comparison of Numerically Predicted Normalized Nusselt Number with Experimental Data for V-Shaped 45° Rib Configuration

A grid independence study was conducted to ensure accurate and reliable results across different Reynolds numbers. Simulations were initially performed at  $Re = 168,013$  and  $Re = 376,534$ , using four different mesh densities of 1.65, 2.18, 3.43, and 5.07 million elements. As shown in Figure 3. The results indicated a 2.4% variation in the overall normalized Nusselt number ( $Nu/Nu_0$ ) between the coarsest and finest meshes, confirming minimal sensitivity to further mesh refinement. After evaluating both accuracy and computational efficiency, the mesh with 2.18 million elements was selected for all simulations. For model validation, the Nusselt number distribution within the channel was compared with experimental data from [14]. Figure 4 presents the normalized Nusselt numbers for the V rib configuration at Reynolds numbers of 168013, 252900, 292468, 334912, and 376534. The comparison shows an overall agreement in trends between the numerical and experimental results. While the CFD simulation effectively captures the trend of the normalized Nusselt number across various Reynolds numbers, it slightly overpredicts the values at higher Reynolds number conditions. The maximum mean error was found to be 8%, with a minimum error of 2%. This overprediction may be attributed to the limitations of the turbulence model in accurately predicting complex flow physics at extremely high Reynolds numbers ( $> 90,000$ ).

### 2.3. Boundary conditions

Air was used as the working fluid in the simulations. It was assumed to be incompressible with constant properties at an inlet temperature of 300 K. The air flow inside the duct was modeled as steady, three-dimensional, and turbulent. At the inlet, a uniform velocity and temperature were applied. The inlet velocity was calculated based on the Reynolds number from a previous experimental study on the V ribs configuration [14]. The turbulence intensity at the inlet was set to 5%. A zero-gauge pressure boundary condition was applied at the outlet. The bottom wall of the duct was subjected to a uniform heat flux of 5000 W/m<sup>2</sup>, while the remaining walls were treated with no-slip and adiabatic conditions. The Nusselt number was calculated on the bottom wall to evaluate the heat transfer performance.

### 2.4. Novel features

This study introduces a series of novel configurations, including the Broken V Rib, Double Broken V Rib, Broken V Rib with Fins, and the V Shaped Fin Array, all oriented at a 45° angle. These designs are aimed at modifying flow behavior within the channel, maintaining a blockage ratio of  $e/D_h=1/20$ , as shown in Figure 5. The airflow direction is from left to right, interacting with the four distinct bottom wall configurations, each exposed to a constant heat flux. The primary objective of these configurations is to enhance heat transfer by inducing flow separation and reattachment, which are critical for improving thermal performance. Additionally, the focus is on minimizing the blockage ratio, which becomes particularly important at high Reynolds numbers where the boundary layer thickness is significantly thinner compared to lower Reynolds number regimes (typically up to  $Re = 90,000$ ). This careful balance of enhancing heat transfer while reducing pressure losses is essential for achieving efficient cooling in high-performance turbine blade internal cooling applications.

The total channel length for all designs was set to six times the hydraulic diameter ( $D_h$ ). In design (b), the distances  $d_1/D_h$ ,  $d_2/D_h$ , and  $d_3/D_h$  were specified as 1/5, 1/4, and 1/3, respectively. For design (c), the distances  $l_1/D_h$ ,  $l_2/D_h$ ,  $l_3/D_h$ ,  $l_4/D_h$ ,  $l_5/D_h$ , and  $l_6/D_h$  were defined as 1/10, 1/5, 1/6.6, 1/3, 1/10, and 1/5, respectively. These distance ratios were selected to account for manufacturing constraints and ease of fabrication, while ensuring that the design maintains its functional integrity.

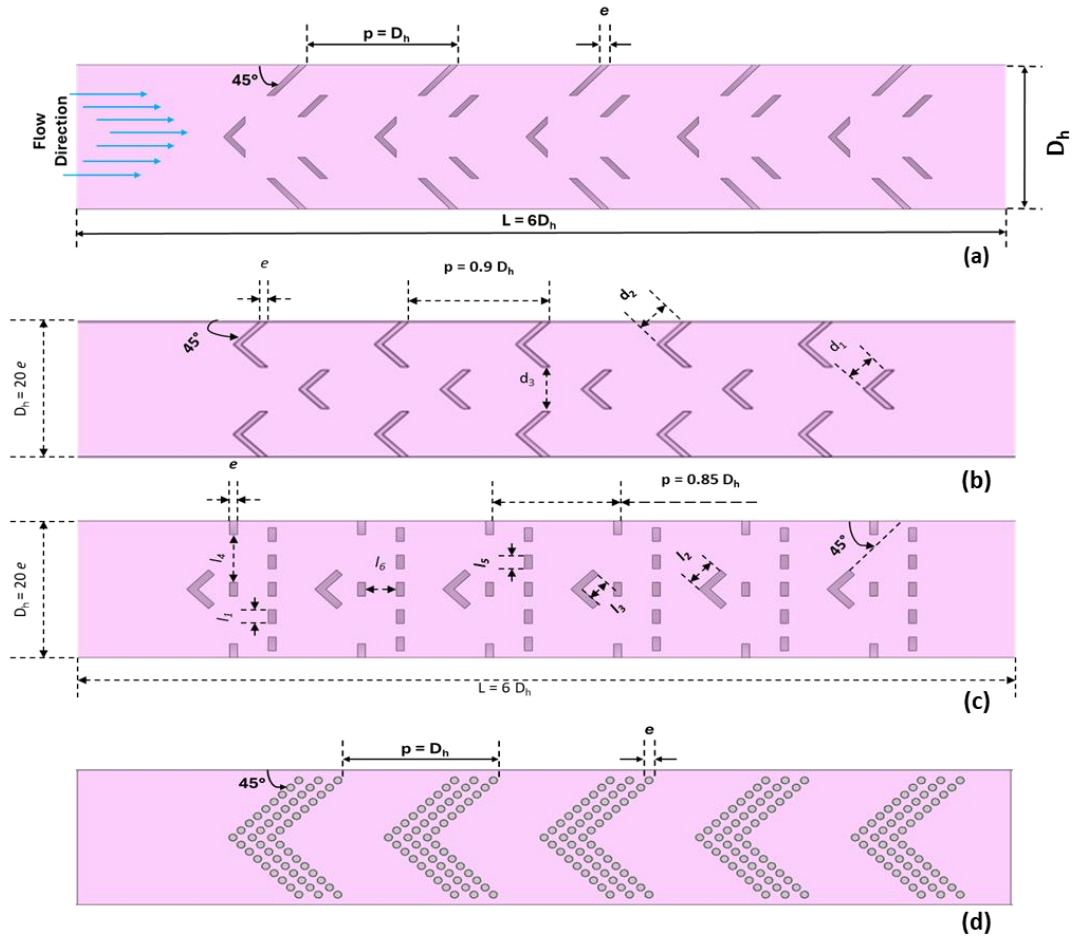


Figure 5: Design configurations of novel structures, all placed at a  $45^\circ$  angle with a rib height to hydraulic diameter ratio  $e/D_h=1/20$ : (a) Broken V rib, (b) Double broken V rib, (c) Broken V rib with fins, and (d) V shaped fin array

### 3. Data reduction

The local heat transfer coefficient was computed using Equation 1, utilizing the known heat flux ( $q''$ ), the local bulk fluid temperature ( $T_\infty$ ) and the wall temperature ( $T_{wall}$ ), which were obtained from the numerical methodology by averaging the bottom wall temperature. The local bulk fluid temperature was derived using linear interpolation across the spanwise direction within the square channel in mid plane inside the duct.

$$h = \frac{q''}{(T_{wall} - T_\infty)} \quad (1)$$

Subsequently, the Nusselt number was calculated using Equation 2. The thermal conductivity of air was determined at the film temperature  $T_f = 0.5 (T_{wall} + T_\infty)$ .

$$Nu = \frac{h D_h}{k} \quad (2)$$

To evaluate the overall thermal performance, the computed Nusselt number was normalized using the Nusselt number for fully developed turbulent flow in a smooth circular tube, based on the Dittus-Boelter correlation, as shown in Equation 3. The normalized Nusselt number, calculated using Equation 4, was then used to assess the thermal performance of the ribbed internal cooling passage.

$$Nu_0 = 0.023 Re^{0.8} Pr^{0.4} \quad (3)$$

$$\frac{Nu}{Nu_0} = \frac{h D_h}{k \times 0.023 Re^{0.8} Pr^{0.4}} \quad (4)$$

The baseline frictional losses were determined using the Blasius equation, as expressed in Equation 5. The total pressure drops across the test channel, used to obtain the friction factor, was calculated according to Equation 6 that, represents the Fanning friction factor, which is calculated using the pressure drop from the simulation. This friction factor was then normalized with the baseline friction loss, as provided in Equation 7.

$$f_0 = 0.079 Re^{-0.25} \quad (5)$$

$$f = \frac{\Delta P D_h}{2 \rho u^2 L} \quad (6)$$

$$\frac{f}{f_0} = \frac{\Delta P D_h}{2 \rho u^2 L (0.079 Re^{-0.25})} \quad (7)$$

Finally, the thermal hydraulic performance (THP) of the system was evaluated using Equation 8, providing a comprehensive measure of the heat transfer enhancement relative to the pressure losses within the cooling passage. The temperature distribution was normalized by determining the ratio of the wall temperature to the fluid inlet temperature, as described in Equation 9. This normalization allows for a dimensionless evaluation of the temperature distribution, facilitating consistent comparison across various configurations and operating conditions.

$$THP = \frac{\frac{Nu}{Nu_0}}{\left(\frac{f}{f_0}\right)^{1/3}} \quad (8)$$

$$T_{norm} = \frac{T_{wall}}{T_{inlet}} \quad (9)$$

#### 4. Results and Discussion

In this section, a detailed discussion of the flow field and heat transfer characteristics of different novel features is presented.

##### 4.1. Heat transfer study

To better understand the flow behavior, heat transfer augmentation, and temperature uniformity on the bottom wall, normalized Nusselt number and temperature contour plots were generated. These plots offer critical insights into the temperature distribution across the duct span, helping to identify localized hotspots caused by the implemented design features. The contour plots effectively illustrate how the fluid moves from the inlet (indicated by the green arrow) at the bottom surface, to the outlet (indicated by the black arrow) at the top, representing the actual flow behavior in the computational domain. This analysis underscores the thermal performance of each

configuration, providing a clear visual representation of how the flow impacts heat transfer. The ability to identify regions of suboptimal temperature uniformity or localized hot spots enables targeted improvements to the design. Such insights are essential for optimizing the overall system performance and achieving more efficient cooling in practical applications.

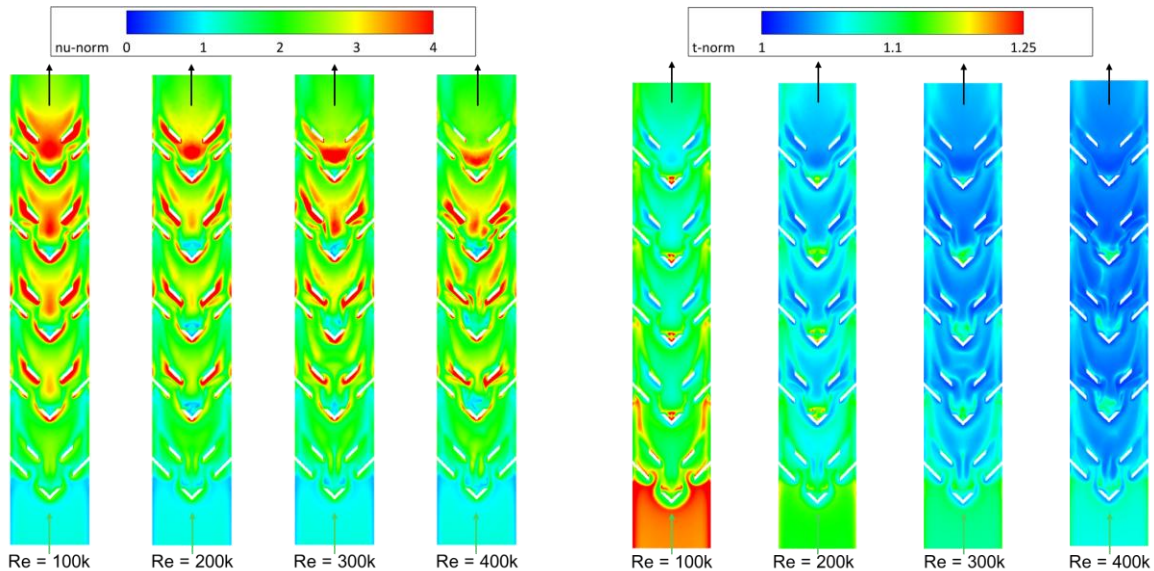


Figure 6: Normalized Nusselt number (left) and temperature (right) distribution at bottom wall for broken V rib features on Reynolds number ranging from 100k to 400k

In ribbed channels featuring V shape broken ribs oriented at  $45^\circ$ , the greatest heat transfer enhancement was observed near the roughness of adjacent passages, where flow detachment and reattachment occur downstream, as depicted in Figure 6 (left). However, enhancement diminishes along the rib due to boundary layer development. Maximum heat transfer occurs near the reattachment point on the inner wall (downstream of the rib features), with the transition from green to red regions indicating an increase in the normalized Nusselt number. In regions where higher wall temperatures coincide with hotspots, lower heat transfer coefficients were observed, resulting in reduced normalized Nusselt numbers. Additionally, it can be noted that the flow may not fully developed upon encountering the first rib, a typical behavior in turbine internal cooling channels, where the normalized Nusselt number was found to be less than unity in these areas. Additionally, a significant decrement in the wall temperature was observed as the Reynolds number increased, showing a  $\sim 5\%$  reduction at  $Re = 400k$  compared to  $Re = 100k$ . At lower Reynolds numbers, the initial high wall temperatures transitioned into substantial reductions in

mid-range operating conditions, as shown in Figure 6 right. This suggests that the broken ribs enhance secondary flows, resulting in improved cooling of the wall at higher Reynolds numbers, leading to an overall increase in the heat transfer coefficient. Finally, localized hotspots were identified near the side walls and ribs in the temperature contours, caused by fluid recirculation across all operational conditions.

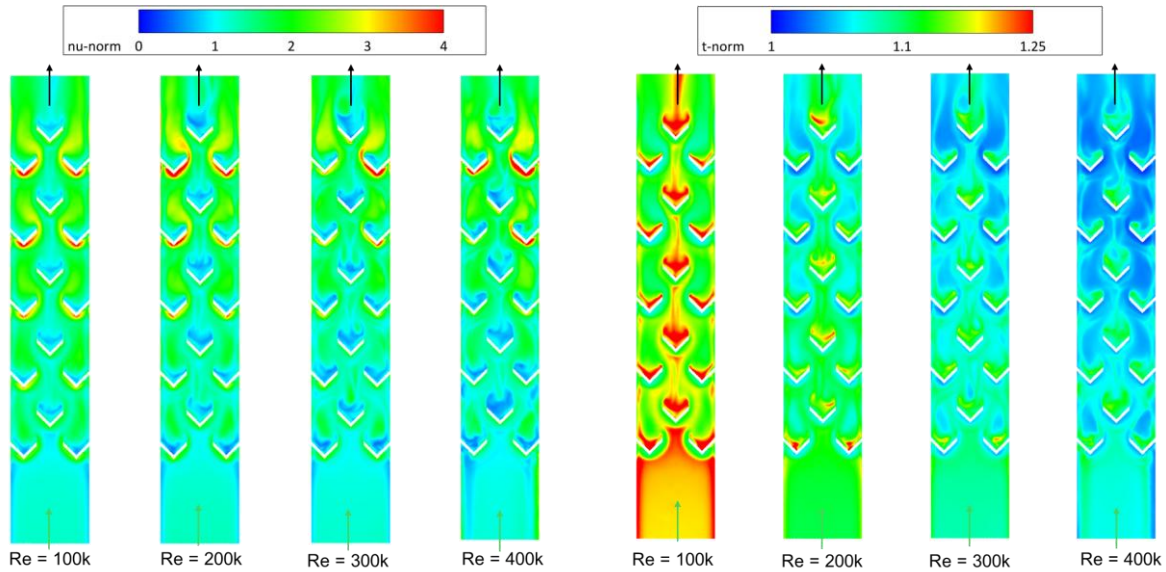


Figure 7: Normalized Nusselt number (left) and temperature (right) distribution at bottom wall for Double broken V rib features on Reynolds number ranging from 100k to 400k

The normalized temperature distribution for the double broken V rib design is shown in Figure 7 (right). At high Reynolds numbers, the normalized temperature remains relatively constant, around 1.1, with minimal variation at  $Re = 300k$ . However, localized hotspots are evident at lower Reynolds numbers, particularly along the centerline, near the front corners of the ribs, and at the trailing edges. These hotspots indicate areas of flow stagnation and recirculation, suggesting that the placement of the ribs along the centerline may be contributing to insufficient fluid mixing and delayed reattachment further downstream. Addressing these flow accumulation regions is essential for achieving a more uniform wall temperature distribution and maintaining consistent thermal performance. The heat transfer enhancement provided by the ribbed passages is further evaluated through the normalized Nusselt number distribution, as illustrated in Figure 7 (left). The spanwise Nusselt number profile is relatively uniform for both low and high Reynolds numbers, with a slight increase from the inlet. The leading edges of the ribs, oriented against the fluid flow,

show higher normalized Nusselt numbers, indicating enhanced heat transfer, while the trailing edges exhibit lower values. This pattern highlights the effectiveness of the rib configuration in promoting heat transfer augmentation, though some localized hotspots remain downstream, particularly near the ribs. This emphasizes the need for design optimization to balance heat transfer performance and temperature uniformity.

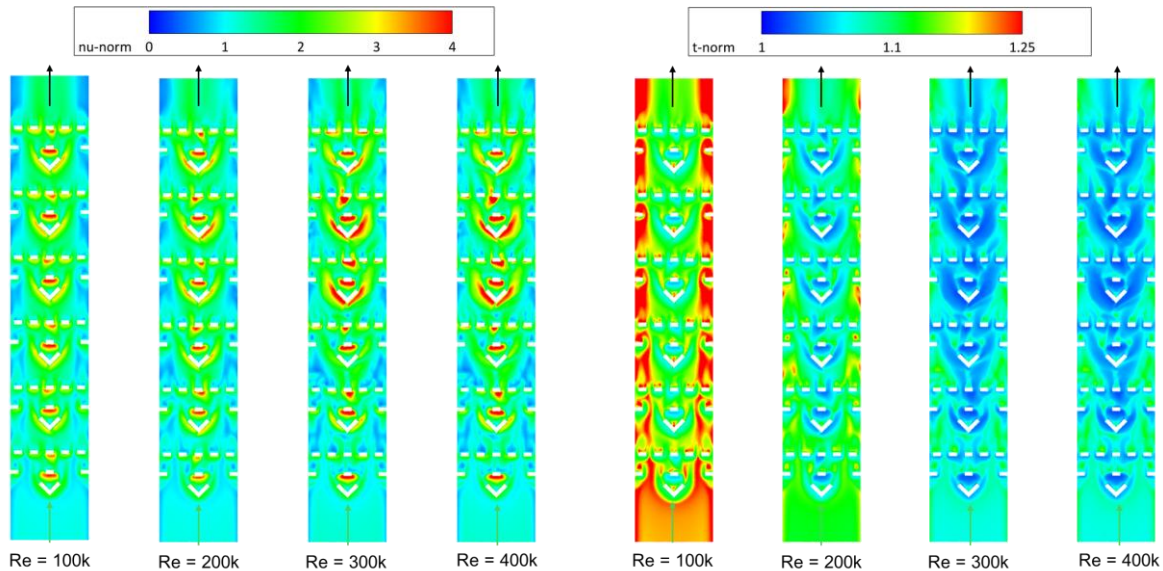


Figure 8: Normalized Nusselt number (left) and temperature (right) distribution at bottom wall for broken V rib with fin features on Reynolds number ranging from 100k to 400k

In the case of ribs with fins, oriented against the fluid flow, the trailing edges of the fins—particularly on the denser side exhibit higher normalized Nusselt numbers, as shown in Figure 8 (left). This indicates enhanced heat transfer at these locations. Comparative analysis shows that the configuration featuring V shape rib with fin combination underperformed in terms of heat transfer augmentation compared to both broken rib configuration shown above. This highlights the beneficial impact of the ribs in directing and enhancing fluid flow for improved thermal performance. Additionally, it is noteworthy that the rib-adjacent passage on the bottom wall is not properly cooled when using this non-traditional design. A significant temperature normalization difference has been observed in this case compared to the all-broken rib configuration Figure 8 (right), indicating poorer performance when uniform temperature distribution is required to effectively cool the inlet surface.

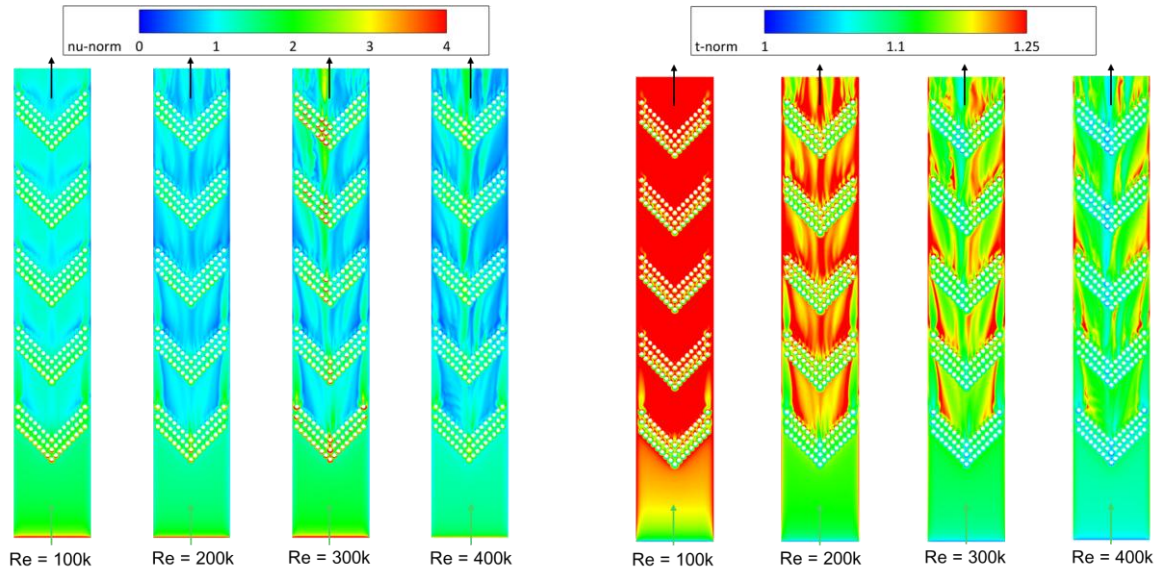


Figure 9: Normalized Nusselt number (left) and temperature (right) distribution at bottom wall for v shape fin array features on Reynolds number ranging from 100k to 400k

The discrete fin array structure, positioned at a  $45^\circ$  angle of attack, significantly underperforms in terms of fluid mixing and uniform cooling. As shown in Figure 9 (right), at  $Re = 100k$ , the normalized temperature on the bottom wall is notably higher compared to the other three designs ( $\sim 1.3$  times). This suggests poor fluid mixing downstream of the fin array, resulting in local hotspots along the channel wall. Even at  $Re = 400k$ , the fin array continues to produce higher local hotspots near the edges of the bottom wall, indicating that this non-traditional fin array is not an optimal choice for this internal cooling application. Furthermore, the Nusselt number ratio for the fin array design is considerably lower than that of the other configurations presented in this study. This indicates that the use of small extended surface fins is ineffective in handling complex turbulent flows, especially when higher cooling performance is required. The Nusselt number distribution suggests that turbulent kinetic energy remains weak across all Reynolds numbers, as the fluid fails to detach properly downstream of the fins, limiting the mixing of comparatively colder fluid with the hot fluid near the wall. This inefficiency underscores the unsuitability of the fin array for enhancing heat transfer in applications demanding high thermal performance. A detailed understanding of the complex flow dynamics, especially the generation of secondary flows due to the distribution of ribs and fins within the channel, is essential for evaluating the thermal-hydraulic performance of these designs. The intricate interactions between these features influence the overall heat transfer efficiency and pressure losses, making it crucial

to assess the role of each component in optimizing the performance of this novel rib and fin arrangement.

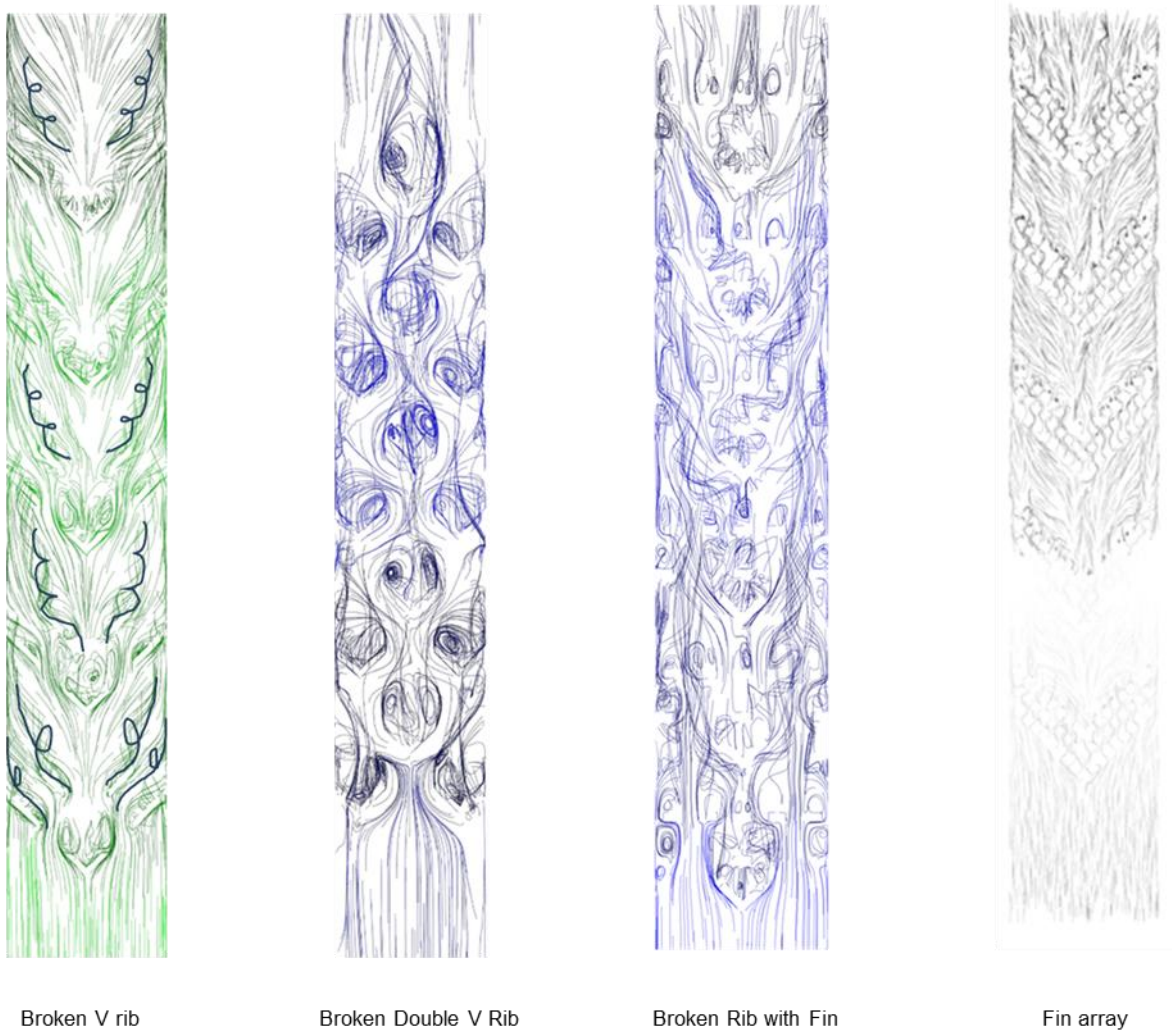


Figure 10: Streamlines near the bottom wall for various geometries at  $Re = 400k$ , showing flow from inlet (bottom) to outlet (top) parallel to the wall in the test section.

To better understand fluid flow behavior near the wall and evaluate the performance of various geometries at a Reynolds number of  $400k$ , a parallel plane positioned  $5\text{ mm}$  above the bottom wall was created for all tested configurations. Figure 10 presents the streamline patterns near the bottom wall, where the lower surface depicts fluid entry and the top represents fluid exit, aligned parallel to the bottom wall in the test section. The streamline analysis reveals distinct vortex formations in different configurations. For both the rib-with-fin and fin-only array

geometries, the added structures disrupt the boundary layer, creating small vortices and increasing turbulence within the duct. However, despite this turbulence, these configurations exhibit limited mixing with the main flow, resulting in suboptimal cooling of the bottom wall. In contrast, the double broken rib configuration, designed with ribs arranged in a V-shape and angled at  $45^\circ$ , generates multiple vortices due to the rib orientation. Although this arrangement increases local turbulence and creates secondary flow structures, the generated vortices dissipate before effectively mixing with the core flow downstream. This limitation impacts the ability of the double broken rib configuration to cool the bottom wall effectively. Notably, the  $45^\circ$  V-broken rib configuration demonstrates superior performance. This arrangement generates four distinct vortices, enhances turbulence, and promotes effective reattachment (indicated by black lines) along the bottom wall. This reattachment occurs downstream of the ribs, following the V-shaped path, which significantly improves mixing with the mainstream flow.

The heat transfer enhancement induced by V-shaped ribs can be effectively analyzed through stream trace patterns, which reveal that the flow, upon separation at the rib, undergoes immediate reattachment downstream. A similar trend has been observed in previous studies under low Reynolds number conditions as well. Previous studies [11][21] provides evidence that these features are well-designed to enhance heat transfer due to their superior geometry configuration, particularly when placed in a V-shape with a  $45^\circ$  angle of attack. Consequently, this configuration achieves more effective bottom wall cooling and provides superior heat transfer enhancement compared to the other tested geometries. In summary, the  $45^\circ$  V-broken rib configuration stands out as the most effective geometry for enhancing heat transfer in gas turbine applications, owing to its ability to generate sustained turbulence and promote fluid mixing in the duct. This feature makes it a viable choice for applications requiring efficient thermal management.

## 4.2. Overall performance

The normalized Nusselt number, friction factor, and thermal-hydraulic performance (THP) have been calculated from the methodology and equations mentioned in Section 3. All values are presented and discussed in this section as a function of the various operating Reynolds numbers chosen for this study.

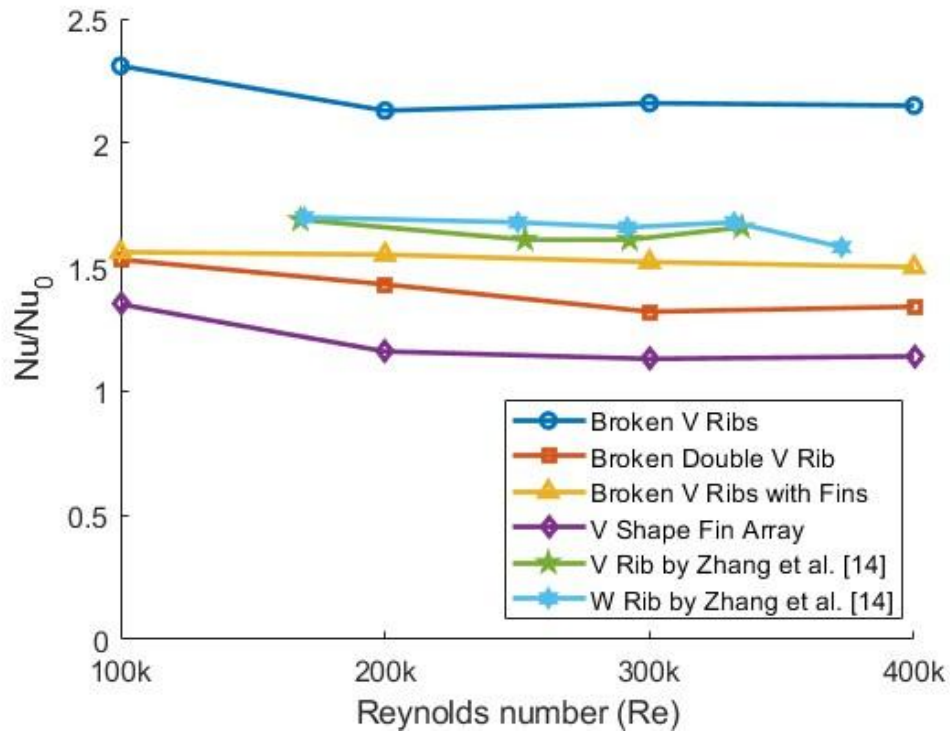


Figure 11: Comparison of normalized Nusselt number for this study and different features from Zhang et al. [14].

As shown in Figure 11, the broken rib configuration significantly surpasses all other rib designs in terms of heat transfer performance. This improvement can be attributed to the discrete rib structure, which generates Rotating Vortex Pairs (RVPs) along the spanwise direction of the bottom wall, enhancing turbulence transport. At lower Reynolds numbers, the primary heat transfer mechanism is the increase in near-wall turbulence kinetic energy (TKE) driven by secondary flows. The normalized Nusselt number for the broken ribs is 26% higher than that of the W-rib configuration, which offered the highest thermal hydraulic performance (THP) in the reference study, and 59% higher than the rib-with-fin configuration

analyzed in this study. Furthermore, the broken V-shaped ribs exhibit consistent heat transfer performance even at elevated Reynolds numbers. As the flow transitions from 200k to 400k the design maintains steady heat transfer enhancement, demonstrating its reliability for internal cooling in high-Reynolds-number conditions. This stability highlights the broken rib configuration as an excellent option for improving thermal performance in applications requiring efficient internal cooling. In contrast, the fin array shows minimal heat transfer enhancement due to its small structure, which disturbs the thermal boundary layer but fails to sufficiently mix the fluid downstream, resulting in a lower overall cooling rate.

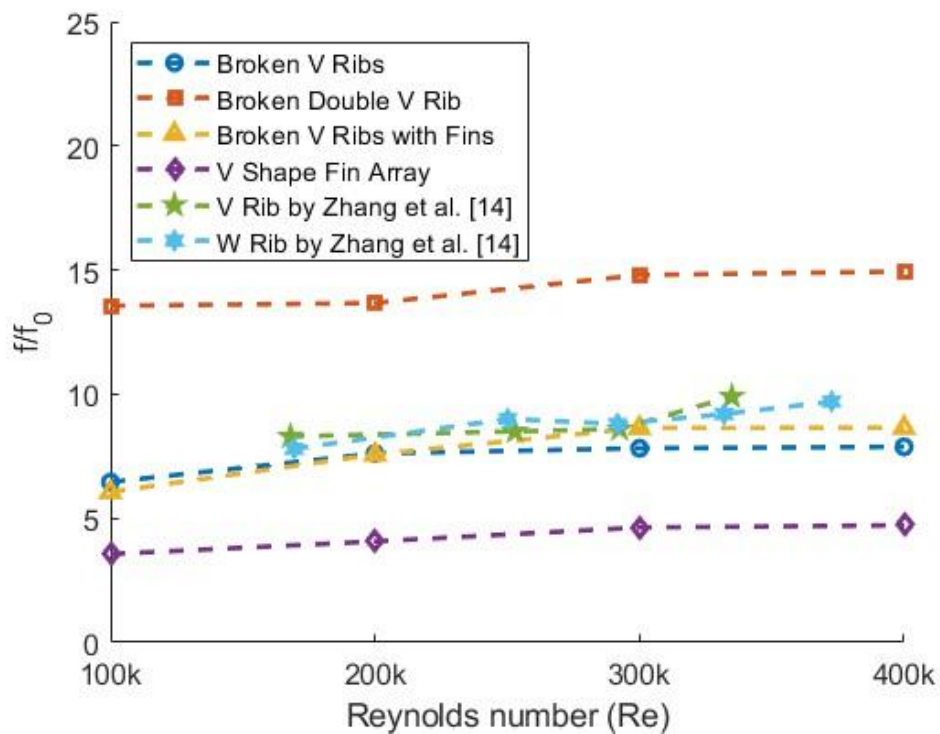


Figure 12: Comparison of normalized friction factor for this study and different features from Zhang at al. [14].

To fully assess the effectiveness of the new rib configurations, it is crucial to consider the trade-off between heat transfer enhancement and frictional losses. Figure 12 provides a detailed comparison of the frictional losses generated by the various rib features within the duct. The results clearly show that the double broken V ribs result in significant frictional losses, primarily due to the closer proximity of the ribs, which increases frictional losses without providing a proportional improvement in heat transfer. This suggests that the excessive rib placement contributes to

unnecessary flow resistance without yielding substantial thermal gains. In contrast, the broken rib configuration, which achieved the highest heat transfer enhancement, also exhibited the lowest frictional losses among the designs. The frictional losses for the broken ribs were 47% lower than those for the double broken V ribs and 20% lower than those for the W ribs from the reference study. This optimal balance of enhanced heat transfer with minimal frictional penalties makes the broken rib structure a favorable choice for internal cooling applications. Additionally, the V-shaped fin array showed the lowest frictional losses due to its small, widely spaced structures, which reduce interference with the airflow, though its heat transfer performance remained modest.

Finally, in both heat transfer augmentation and the associated frictional losses, the rib-with-fin structures fall in the mid-range compared to other configurations. Their cooling performance is notably inferior to the broken rib design and can be a poor choice due to manufacturing challenges posed by their unconventional structure.

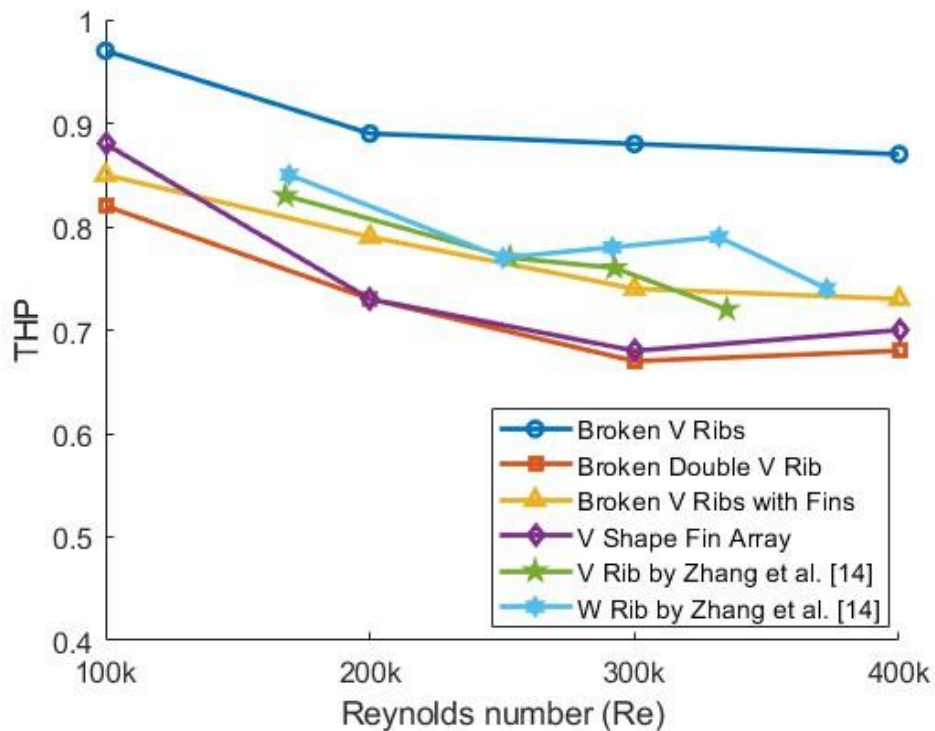


Figure 13: Variation of Thermal hydraulic performance variation with Reynolds number for this study and different structures from Zhang at al. [14].

The Thermal Hydraulic Performance (THP) in the Figure 13 shows how different rib configurations behave as Reynolds number increases. The Broken V Ribs maintain the highest THP across the range, with only a slight decline as Reynolds number rises from 100k to 200k, making it the most effective design overall. In contrast, the Broken Double V Rib experiences the steepest drop in THP, likely due to high frictional losses. The Broken V Ribs with Fins remain relatively stable but perform consistently lower than the standard Broken V Ribs, suggesting fins may disrupt optimal flow and not an ideal choice for the overall efficiency. The V Shape Fin Array offers moderate performance, while V Rib and W Rib configurations from Zhang et al. [14] show decreasing THP with increasing Reynolds numbers. Overall, the Broken V Rib stands out as the best option, combining good heat transfer and low frictional losses. It is worth noting that, out of the four designs studied in this article Broken V shaped ribs at 45° surpassed the THP of the V and W ribs from the reference, their performance did not show a steep decline at elevated Reynolds numbers. This consistent behavior at higher Reynolds numbers suggests that reducing the blockage ratio from 1/10 (as in Zhang et al. [14]) to 1/20 (as in this study) is beneficial. At high Reynolds numbers, typically above 100k, the boundary layer becomes very thin. In such conditions, larger rib heights are unnecessary and may disrupt the flow more than needed resulting in additional frictional losses. Thus, smaller rib heights can effectively improve cooling performance without excessive disturbance.

## 5. Conclusion and Future Recommendation

This study introduces a series of novel rib configurations, including the Broken V Rib, Double Broken V Rib, Broken V Rib with Fins, and V Shaped Fin Array, all positioned at a 45° angle to the fluid flow. The primary objective was to investigate the performance of these non-traditional designs with a reduced blockage ratio of  $e/D_h = 1/20$ , particularly in very high Reynolds number conditions, which have not been extensively studied before.

Among the designs, the Broken V Rib achieved the highest THP (almost 1 at 100k and 0.87 at 400k), with sustained heat transfer enhancement (2.3 times from empirical relation in lower Re and 2.2 time in higher Re) and low frictional losses. In contrast, the Double Broken V Rib exhibited substantial frictional losses (average 14 times higher in all Reynolds number range), which reduced its overall efficiency despite some improvement in heat transfer (maximum 1.53 times higher on 100k and 1.34 times higher in 400k). The Rib with Fin design demonstrated moderate performance but faced challenges in manufacturing and delivered lower heat transfer

compared to the broken rib configurations. The V Shaped Fin Array had minimal frictional losses, but its heat transfer performance was poor, resulting in inefficient cooling. The V-shaped broken ribs placed at a  $45^\circ$  angle in this study not only surpass the V and W ribs from Zhang et al. [14], but also maintain stable performance at higher Reynolds numbers.

Reducing the blockage ratio from 1/10 to 1/20 proved to enhance heat transfer without significantly increasing frictional losses, especially at high Reynolds numbers. Even though the THP for all different designs is less than unity, overall, the Broken V Rib configuration emerged as the most suitable option for internal cooling in high-Reynolds-number conditions (out of all the different non-conventional design), offering a balanced combination of effective heat transfer and minimal frictional penalties.

Nomenclature:

|            |  |
|------------|--|
| $D_h$      | Hydraulic diameter (m)                         |
| $e$        | Features height (m)                            |
| $h$        | Heat transfer coefficient (W/m <sup>2</sup> K) |
| $k$        | Thermal conductivity (W/mK)                    |
| $L$        | Channel length (m)                             |
| $Nu$       | Nusselt number                                 |
| $Nu_0$     | Nusselt number from Dittus-Boelter equation    |
| $p$        | Rib (feature) pitch (m)                        |
| $Pr$       | Prandtl number                                 |
| $q''$      | Heat flux (W/m <sup>2</sup> )                  |
| $Re$       | Reynolds number                                |
| $\Delta P$ | Pressure drop (Pa)                             |
| $u$        | Fluid velocity (m/s)                           |
| $\rho$     | Fluid density (kg/m <sup>3</sup> )             |
| $T$        | Temperature (K)                                |
| $T_\infty$ | Bulk fluid temperature (K)                     |
| $T_{wall}$ | Wall Temperature (K)                           |
| $T_{in}$   | Fluid inlet temperature (K)                    |
| THP        | Thermal hydraulic performance                  |

## CHAPTER 2

### Experimental Analysis of Rib Turbulator Configurations for Thermal Hydraulic Performance Enhancement in Gas Turbine Cooling Channels Operating at Extremely High Reynolds Numbers

Naimish Pandya<sup>a</sup>, Wesley Fisher<sup>a</sup>, Srinath V. Ekkad<sup>1,a</sup>

*<sup>a</sup>Department of Mechanical and Aerospace Engineering North Carolina State University  
Raleigh, NC, USA*

#### **Abstract**

This study presents a comprehensive experimental investigation of the thermal-hydraulic performance of six rib configurations, including Broken 30°, 45°, & 60° ribs and Continuous 30°, 45°, & 60° ribs, at extremely high Reynolds numbers ranging from 100,000 to 400,000. The baseline case for comparison is a smooth duct without features. The experiments were conducted over a wide Reynolds number range, encompassing conditions typical of both land-based and air-breathing gas turbine engines. Detailed heat transfer measurements were performed under steady-state forced convection using Infrared Thermography (IR) techniques. The tested ribs are V-shaped, with a rib-height-to-hydraulic diameter ratio ( $e/D_h$ ) of 1/20 and a rib-pitch-to-rib-height ratio ( $p/e$ ) of 10. The findings reveal that broken rib configurations result in higher heat transfer augmentation and improved thermal-hydraulic performance compared to traditional continuous ribs across the Reynolds number range studied. Additionally, the results demonstrate that broken ribs outperform their continuous counterparts, achieving greater heat transfer enhancement while simultaneously reducing pressure penalties. This study also emphasizes that reducing rib height ( $e/D_h = 1/20$ ) and incorporating broken structures are effective strategies for achieving  $THP > 1$  at extremely high Reynolds numbers, in agreement with findings from prior research. These insights provide a valuable foundation for optimizing internal cooling passage designs in land-

---

<sup>1</sup>Corresponding author:  
E-mail address: [sekkad@ncsu.edu](mailto:sekkad@ncsu.edu)

based and high-temperature gas turbines, ensuring enhanced thermal efficiency and greater operational durability for next-generation turbine applications.

**Keywords** : Heat Transfer Enhancement, Rib Turbulators, Gas Turbine Cooling, Thermal Hydraulic Performance, Extreme Reynolds number

## 1. Introduction

The continuous advancement of gas turbine technology has led to an increased demand for efficient internal cooling methodologies to manage the extreme thermal loads encountered within turbine blades. Internal cooling strategies are generally classified based on geometry, with jet impingement used for leading-edge cooling, pin fins for trailing-edge cooling, and rib-roughened turbulators for mid-region cooling within internal passages of various aspect ratios. Effective thermal management in these components is critical for improving overall turbine efficiency and ensuring long-term operational reliability. The fundamental design parameters influencing internal cooling effectiveness include the length-to-hydraulic diameter ratio ( $L/D_h$ ), rib height-to-hydraulic diameter ratio ( $e/D_h$ ), and rib pitch-to-height ratio ( $p/e$ ), all of which must be optimized to enhance heat transfer while maintaining minimal pressure losses [1,6]. Furthermore, NASA Glenn Research Center's research highlights the critical role of internal cooling mechanisms in protecting gas turbine blades operating at combustor temperatures of 1800-2000 K, while minimizing coolant flow penalties on engine efficiency. Rib turbulators, including square, V-shaped, and broken V-shaped ribs, generate recirculating vortices and reattachment zones, significantly improving cooling effectiveness. Among these, staggered V-ribs demonstrate superior heat transfer performance due to enhanced mixing and turbulence generation, making them a promising design for high-efficiency turbine cooling [22].

Previous investigations have demonstrated that rib turbulators play a crucial role in heat transfer augmentation within mid-chord passages of turbine blades. Han and Park [23] were among the first to observe that heat transfer enhancement in square internal channels, independent of aspect ratio, could be preserved by positioning rib turbulators at an optimal angle of attack relative to the flow direction. Further experimental studies by Han and Zhang [2] revealed that for Reynolds numbers in the range of 15,000 to 90,000, a 60° V-shaped broken rib configuration significantly outperformed traditional continuous ribs, achieving 2.5 to 4 times higher heat transfer enhancement but at the expense of 7–8 times greater pressure drop. Similarly, Zhang et al. [24]

investigated the impact of surface heating in a rotating, ribbed two-pass square channel and demonstrated that 60° angled ribs enhanced heat transfer by up to 3 times, though they also introduced a moderate increase in pressure losses.

Numerous studies have extended the understanding of rib-induced secondary flows and their contribution to turbulent transport mechanisms. Using liquid crystal thermography, Ekkad and Han [3] examined heat transfer distributions in a two-pass square channel with ribbed walls at Reynolds numbers ranging from 6,000 to 60,000, highlighting the superior performance of broken V-ribs in the first pass and parallel 60° ribs in the second pass. Further, Azad et al. [25] analyzed the impact of 45° angled rib turbulators in stationary and rotating two-pass rectangular channels, reporting a 2–3 times increase in heat transfer on ribbed walls relative to smooth walls.

Several recent efforts have focused on exploring novel rib geometries to optimize thermal performance and flow characteristics. Singh et al. [11] combined experimental and numerical techniques to analyze heat transfer in a two-pass ribbed square duct, demonstrating that V-shaped and 45° angled ribs yielded superior heat transfer enhancement relative to W- and M-shaped configurations. Building upon these findings, Singh et al. [26–28] explored additive manufacturing-based rib designs that integrated cylindrical dimples, reporting that hybrid rib-dimple configurations achieved 25% greater heat transfer than conventional rib structures. Ravi et al. [12] conducted a computational study on 45°, V-shaped, W-shaped, and M-shaped ribs, concluding that V-shaped ribs outperformed others by 7% in heat transfer enhancement, albeit with a 19% higher pressure penalty. Singh et al. [10] examined a square duct featuring a crisscross rib topology and found similar Nusselt number ratios ( $Nu/Nu_0$ ) of 2.7–3.1 across Reynolds numbers ranging from 30,000 to 60,000. Maurer et al. [18] analyzed V-shaped features and their performance under extremely high Reynolds number conditions using both CFD and experimental approaches. Their main findings reveal that reducing the pitch-to-rib height ratio by 10 decreases the pressure drop penalty while enhancing heat transfer and thermal performance. Thianpong et al. [29] examines heat transfer enhancement in a square duct with V-shaped flapped baffles for Reynolds numbers 3,000–21,000 using the finite volume method and Realizable  $k$ - $\epsilon$  model. Their key parameters include blockade ratio ( $BR = 0.05$ – $0.3$ ), flap angle ( $\beta = 0^\circ$ – $90^\circ$ ), hole diameter ratio ( $dR = 0.5$ – $0.8$ ), and attack angle ( $\alpha = 60^\circ$ – $30^\circ$ ). Results show that a flapped baffle with  $\beta = 20^\circ$  and  $BR = 0.25$  achieves  $Nu/Nu_0 = 8.4$  and thermal enhancement factor  $\sim 2.49$  at the lowest  $Re$ .

Zhang et al. [30] numerically investigates turbulent flow and convective heat transfer in turbine blade cooling channels for a wide Reynolds number  $Re = 20,000\text{--}80,000$ . Results reveal that oblique ribs outperform transverse ribs, achieving higher heat transfer and lower friction losses. The study establishes the relationship between secondary vortices and turbulent kinetic energy, optimizing heat transfer by adjusting rib height ( $e/D_h = 0.047\text{--}0.101$ ) and rib spacing ( $p/e = 10\text{--}15$ ). The optimal configuration ( $e/D_h = 0.062$ ,  $p/e = 15$ ) maximizes the performance factors. Dinh et al. [31] numerically investigate internal cooling in turbine blades using truncated-root ribs to improve heat transfer efficiency. Using Reynolds-Averaged Navier-Stokes (RANS) simulations, results show that truncated-root ribs increase Nusselt number by 8.56% at  $Re = 37,392$  and improve thermal performance by 39.24% at  $Re = 53,697$  compared to squared ribs. The findings confirm truncated-root ribs as a superior cooling strategy for turbine blade internal cooling.

Chen et al. [32] examines the thermal performance of V-type rib configurations in a rotating, two-pass cooling channel for  $Re = 10,000\text{--}45,000$  in the first pass ( $16,000\text{--}73,500$  in the second pass), and  $Ro = 0.39$  (first pass),  $0.16$  (second pass), results show that rotation slightly reduces heat transfer in the first pass but enhances it on the leading surface in the second pass. The staggered, discrete V-ribs outperform traditional V-ribs and standard  $45^\circ$  ribs, yielding higher heat transfer and thermal efficiency while mitigating frictional losses, making them a promising cooling strategy. Kumar and Pathak [33] investigates heat transfer enhancement in a rectangular cooling channel ( $AR = 4:1$ ) using  $45^\circ$  V-ribs and broken V-ribs with spherical dimples for  $Re = 20,000\text{--}80,000$ . The highest heat transfer enhancement factor (2.46) occurs for a  $45^\circ$  V-rib (1.5 mm height) with a dimple  $\sim 4.0$  mm depth, while the maximum thermal performance factor  $\sim 1.205$  is achieved with a  $45^\circ$  V-rib with 1.0 mm height and, dimple 2.0 mm depth, confirming their efficiency in turbine cooling. Fang et al. [34] investigate turbulent flow structures in a square duct with V-shaped ( $60^\circ$  and  $45^\circ$ ) and perpendicular ( $90^\circ$ ) ribs using large-eddy simulation (LES). Their results show that perpendicular ribs generate streamwise-elongated vortices, while V-shaped ribs form turbulent packets near the sidewalls regions. Spatial and temporal autocorrelations indicate that turbulence is more isotropic in V-shaped ribs, with a higher energy spectrum, confirming the significant impact of rib geometry on vortex formation, velocity fluctuations, and energy distribution in confined duct flows.

Notably, high Reynolds number conditions are often encountered within high-pressure turbine blade passages in industrial gas turbine engines. In this context, Rallabandi et al. [5] investigated the heat transfer and frictional characteristics of 45° ribs at Reynolds numbers ranging from 30,000 to 400,000, concluding that thermal hydraulic performance (THP) decreases at higher Reynolds numbers due to increasing frictional losses associated with large  $e/D_h$  ratios. Their subsequent work [9] extended this analysis to rotating blade-shaped serpentine coolant passages, emphasizing that while heat transfer enhancement of up to 2.5 times was achievable, increasing rib height led to excessive pressure drops, making conventional designs less effective for high Reynolds number applications. Furthermore, they extend this study by examining the influence of round-edged ribs on heat transfer performance at high Reynolds numbers [8]. Their findings indicate that heat transfer enhancement is more pronounced with a decrease in rib-to-rib spacing, typically useful by a lowering a  $p/e$  ratio in high Reynolds number regimes. This improvement is attributed to the increased surface area available for heat transfer. Additionally, they observed that round-edged ribs are more effective in mitigating frictional losses while promoting greater fluid recirculation in the flow domain. For very high Reynolds numbers (150,000–400,000), Zhang et al. [14] analyzed the effectiveness of continuous ribs, demonstrating significant thermal performance enhancement, though at the cost of substantial frictional losses. Pandya and Ekkad [16] numerically analyzes broken V-shaped ribs (45°) for gas turbine cooling channels at high Reynolds numbers ( $> 90,000$ ) using a high fidelity CFD and RANS approach. The prior results shows that the broken V-ribs outperform continuous V-ribs in thermal efficiency, making them ideal for land-based turbines operating at extremely high Reynolds number range  $Re = 100,000$ –650,000.

Despite substantial advancements in rib-enhanced internal cooling, the majority of research has focused on Reynolds numbers below 90,000, leaving a critical gap in understanding turbine blade cooling performance at extremely high Reynolds numbers (100,000 – 400,000). The present study aims to bridge this gap by investigating the thermal-hydraulic performance (THP) of rib-roughened cooling channels under steady-state, non-rotational conditions at high Reynolds numbers. It has been observed that rib turbulator configurations optimized for low Reynolds number conditions are not effective at high Reynolds numbers [8,14,35]. At extreme high Reynolds numbers, the boundary layer thickness inside a duct flow decreases significantly, which necessitates modifications to the rib geometries to mitigate the associated frictional losses while

maintaining thermal performance. Given the inherently high baseline heat transfer at these conditions and the increasingly thinner boundary layers, substantial heat transfer enhancement becomes increasingly challenging. A key approach to improving thermal hydraulic performance at high Reynolds numbers involves minimizing the structural height of the rib turbulators, irrespective of their geometric shape. Reducing rib height not only decreases frictional losses but also effectively trips the comparatively thin velocity boundary layer near the wall, optimizing the interaction between secondary flows and heat transfer enhancement. Additionally, the implementation of broken rib structures presents a viable strategy to further reduce frictional losses. These structures introduce multiple vortices that enhance secondary flow development while minimizing the significant pressure drop typically associated with continuous ribs. The objective of this research study is to systematically investigate and address the limitations of existing rib turbulator configurations at high Reynolds numbers. First, we analyze three widely used rib inclination angles  $30^\circ$ ,  $45^\circ$ , and  $60^\circ$  for both traditional continuous rib designs and broken rib configurations, while maintaining a reduced rib height ratio of  $e/D_h = 1/20$ . This investigation aims to establish optimized design guidelines for rib turbulators that maximize heat transfer while minimizing frictional losses, ultimately improving the efficiency of high Reynolds number internal cooling applications.

## **2. Experimental setup**

To systematically investigate the thermal-hydraulic performance of rib turbulators in high Reynolds number flows, a custom-designed experimental setup was developed. All experimental calculations, device selection, and instrumentation methodology have been based on standardized and fundamental practices in this field [1][36]. A schematic diagram and an actual photograph of our rig are shown in Figure 14 and Figure 15, respectively. The test section, constructed from Plexiglass, was meticulously designed to facilitate precise thermal and flow measurements while ensuring minimal disturbances to the airflow. In this experiment, air at laboratory conditions flow into a duct test section through a high-speed pressure blower (The New York Blower Company, wheel type 1710 ALUM), driven by a 20 HP electric motor. This blower provided a stable and adjustable flow rate, which was carefully regulated by a variable frequency drive (VFD), allowing for fine-tuned control of airflow velocity to achieve the desired Reynolds number range. A custom nozzle was additively manufactured to join the blower outlet to the entry region of the channel,

which is a uniform 4" × 4" cross section along the entire length of the channel. This cross section was chosen based on scaling factors relating engine conditions to the ambient experimental conditions. The entry region is  $6D_h$  long to provide a flow development region prior to the actual test section. The rib turbulators are then placed in an  $6D_h$  long section immediately after the inlet section. This is where the measurements are taken and hence will be referred to as the test section. Lastly, another  $3D_h$  long exit region exhausting into the atmosphere is placed after the test section to ensure that the flow inside the test section still behaves like an enclosed duct with no influence from the exhaustion process.

The bottom wall of the test section is heated by a KHA-412/10-P polyimide film flexible heater, which is placed on the inside of the bottom test section surface. The input heat flux is controlled by a Variac TDGC-0.5KM (std. 5% error) and is kept constant at  $5000 \text{ W/m}^2$  for all experiments. A thin aluminum sheet is placed on top of the heater to uniformly distribute the input heat flux across the entire test section surface. The rib turbulators, which are additively manufactured from ABS, are glued on top of the aluminum sheet. The aluminum sheet is spray painted black to give stronger emissions for the IR camera. The ribs are specifically printed in a white color to reduce their emissions, making them more obvious as seen from the IR camera. Since ABS has a low thermal conductivity of  $0.19 \text{ W/mK}$ , heat transfer data cannot be reported on the rib surfaces since it voids the heat flux assumption in the calculation method as discussed in the following section, so clearly distinguishing the locations of the ribs is quite important for data processing purposes. A crucial aspect of the study was the measurement of wall temperature, which was accomplished using a high-resolution FLIR SC 325 infrared (IR) camera with a spatial resolution of  $320 \times 240$  pixels and a measurement accuracy of  $\pm 2\%$ . The top wall of the Plexiglass test section has an  $18'' \times 4''$  cut out, which is replaced with a Vinylidene Chloride-Vinyl Chloride co-polymer (Saran Wrap) to provide an infrared-transparent window for the IR camera to observe the test section temperature distribution. This  $18'' \times 4''$  window, carefully positioned on the top wall of the wind tunnel, provided an unobstructed view, ensuring that the IR camera captured highly precise temperature data of the heated bottom wall. The IR camera readings are calibrated for each different aluminum sheet using thermocouples attached to the test surface.

The flow velocity was measured using a Dwyer 166-6-CF pitot-static tube, which protrudes into the inlet section of the channel and is connected to a Dwyer 477AV digital manometer provide real-time total and static pressure measurements. These pressure values are used to calculate flow

velocity ( $v$ ) using the Bernoulli equation and the corresponding Reynolds number ( $Re$ ). A static pressure tap was placed in the bottom wall of the channel  $0.5''$  upstream and downstream of the test section to evaluate pressure losses. Dwyer A-421 metallic static pressure probes were used for this, and the probes are connected to the same digital manometer. Several small holes are placed along the test section to insert thermocouples to measure bulk fluid temperature for data reduction purposes, as discussed in the following section. These thermocouples are J-KEM Scientific K type TWT Thermocouple measured by Omega 2 channel HH912T Thermometers with  $\pm 0.04\%$  accuracy.

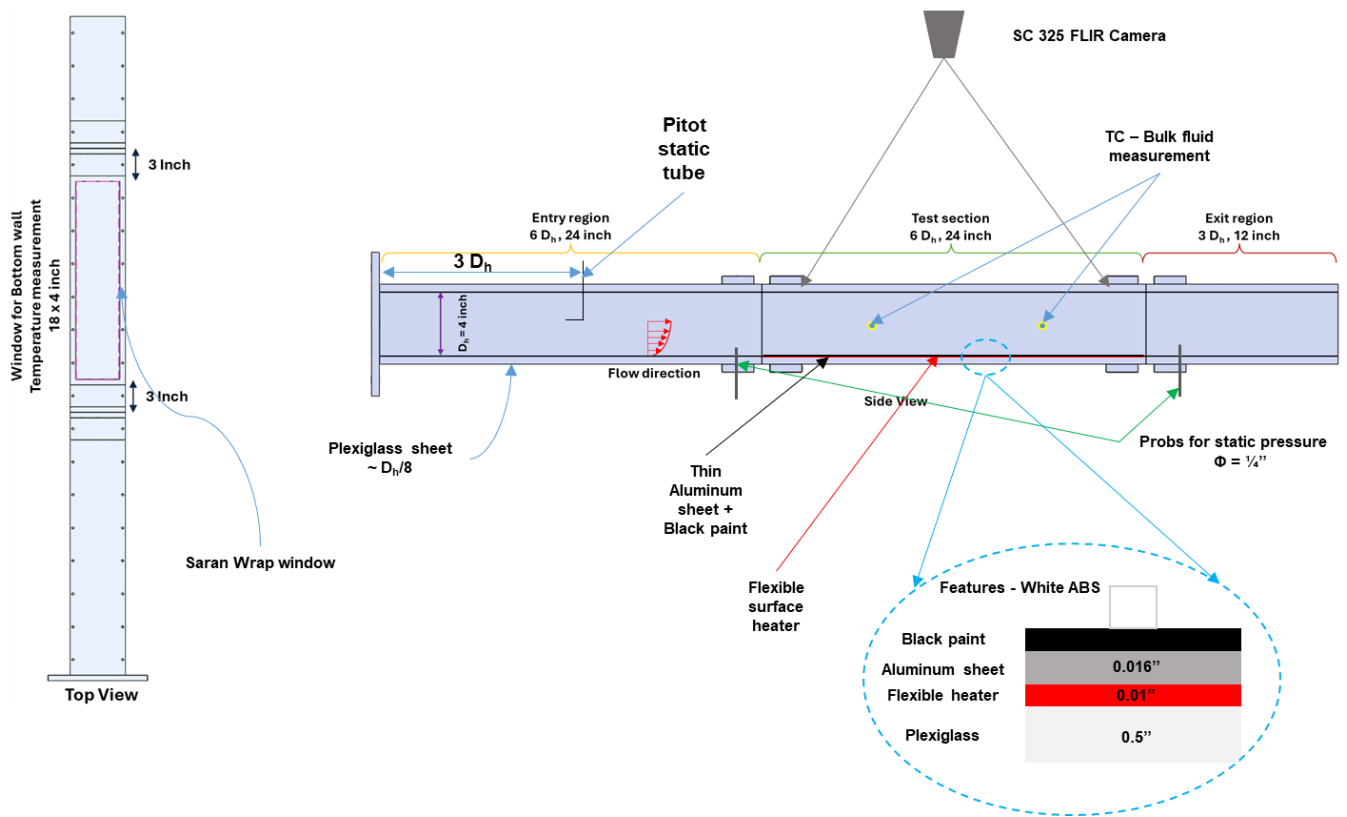


Figure 14: Schematic of experimental setup

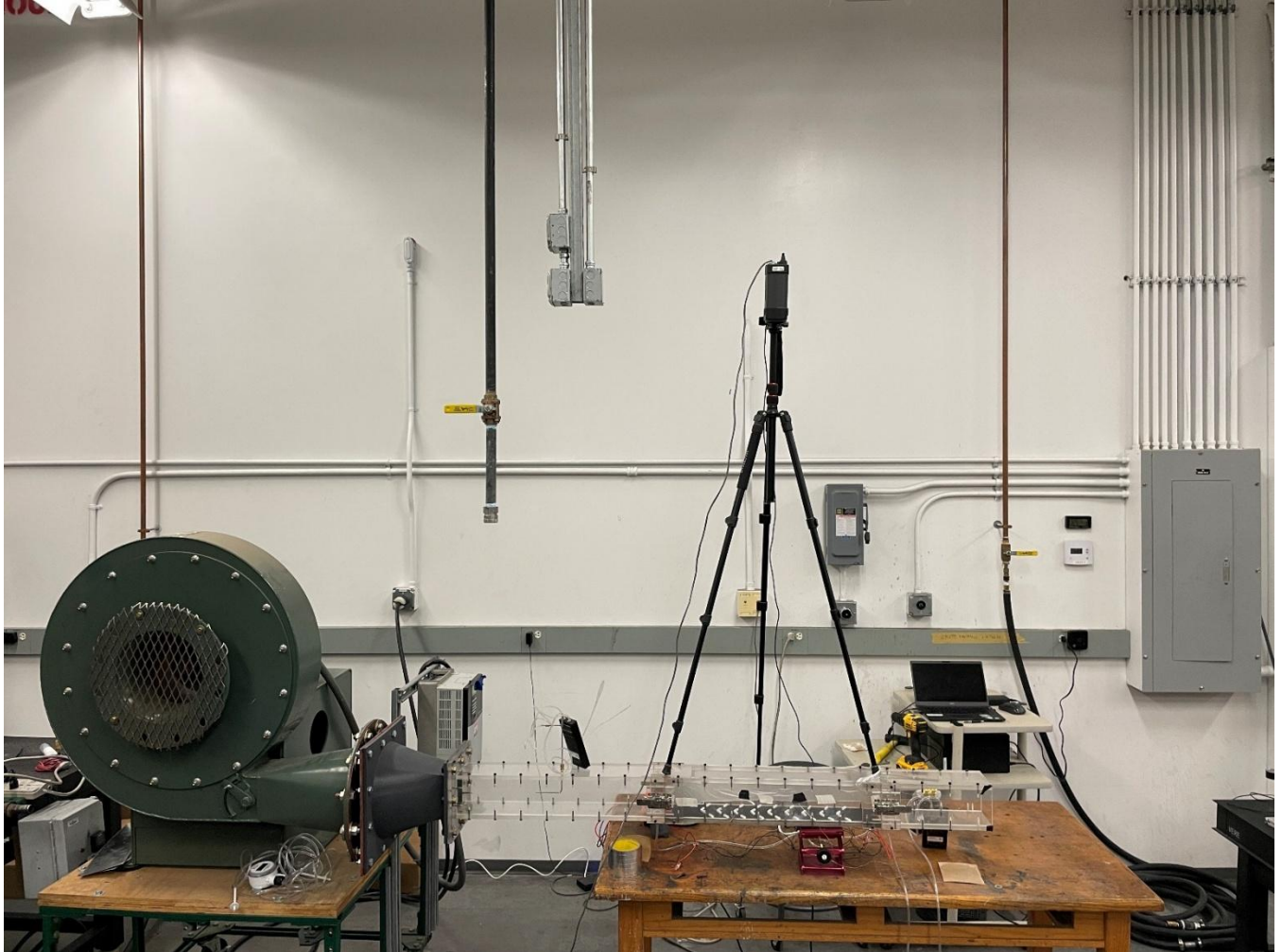


Figure 15: Actual Experimental setup photograph

### 2.1. Heat transfer co-efficient & overall thermal performance measurement

Before conducting the forced convection heat transfer experiments, a heat loss experiment was first performed to establish an accurate heat loss coefficient ( $\alpha$ ). This step was critical in ensuring accurate convective heat transfer coefficient ( $h$ ) calculations. In this preliminary experiment, multiple constant heat flux levels were applied to a smooth bottom wall, and steady-state temperature changes were recorded using the IR camera. Although the very thin aluminum sheet was surrounded by insulating materials (i.e. Plexiglass channel walls), there was considerable heat loss which had to be accounted for in the heat transfer coefficient calculations. To that extent, multiple heat loss experiments were carried out prior to carrying out forced convection experiments. During the heat loss experiments, the duct exit was blocked to prevent any continuous

flow of contained air to the laboratory ambient. A correlation was then developed by plotting the recorded temperature ( $T_w - T_\infty$ ) against applied constant heat flux, which allowed for a precise estimation of heat loss ( $q''_{loss}$ ). The heat loss coefficient was calculated using the Equation 10 for ( $\alpha$ ):

$$\alpha = \frac{q''_{loss}}{(T_{wall}(x,y) - T_\infty)} \quad (1)$$

The bulk fluid temperatures  $T_{bulk}$  were measured 8'' after the inlet and 8'' before the outlet of the test section. Due to the addition of heat into the fluid domain, bulk fluid temperature is expected to increase with increasing streamwise distance. However, the total heat addition into the fluid domain was negligible compared with the energy required to raise the fluid temperature by 0.25 – 0.3 °C considering very high heat capacity of the fluid flow.

$$h = \frac{q''_{flow}}{(T_{wall}(x,y) - T_{bulk})} - \alpha \quad (2)$$

Once the heat loss was quantified, the forced convection heat transfer coefficient ( $h$ ) was determined by Equation 11. At steady state, three snapshots were taken from the reference IR camera window and the mean of these multiple images was used and processed to obtain  $T_w(x,y)$ . The normalized Nusselt number was calculated using Equation 12 where the obtained Nusselt number was normalized with the Dittus-Boelter correlation for Nusselt number in a developed turbulent internal flow.

$$\frac{Nu}{Nu_o} = \frac{h D_h}{k_f(0.023 Re^{0.8} Pr^{0.4})} \quad (3)$$

Where the  $k_f$  is the fluid (air) thermal conductivity measured at the temperature of  $T_f = 0.5 (T_{wall}(x,y) + T_{bulk})$ . The baseline frictional losses were determined using the Blasius equation, as expressed in Equation 13.

$$f_0 = 0.079 Re^{-0.25} \quad (4)$$

$$f = \frac{\Delta P D_h}{2 \rho u^2 L} \quad (5)$$

$$\frac{f}{f_0} = \frac{\Delta P D_h}{2 \rho u^2 L (0.079 Re^{-0.25})} \quad (6)$$

The total pressure drops across the test channel, used to obtain the friction factor, was calculated according to Equation 14 that, represents the Fanning friction factor, which is calculated using the static pressure drop calculated through a static pressure probs across the test section. This friction factor was then normalized with the baseline friction loss, as provided in Equation 15. Once the heat transfer and pressure drop characteristics were determined, the thermal-hydraulic performance (THP) of the test channel was assessed using a dimensionless THP according to Equation 16:

$$THP = \frac{\frac{Nu}{Nu_0}}{\left(\frac{f}{f_0}\right)^{1/3}} \quad (7)$$

This equation provided a comprehensive metric to evaluate the effectiveness of the rib turbulator configurations, by quantifying the balance between heat transfer enhancement and pressure penalties.

## 2.2. Description of test configuration with different ribs

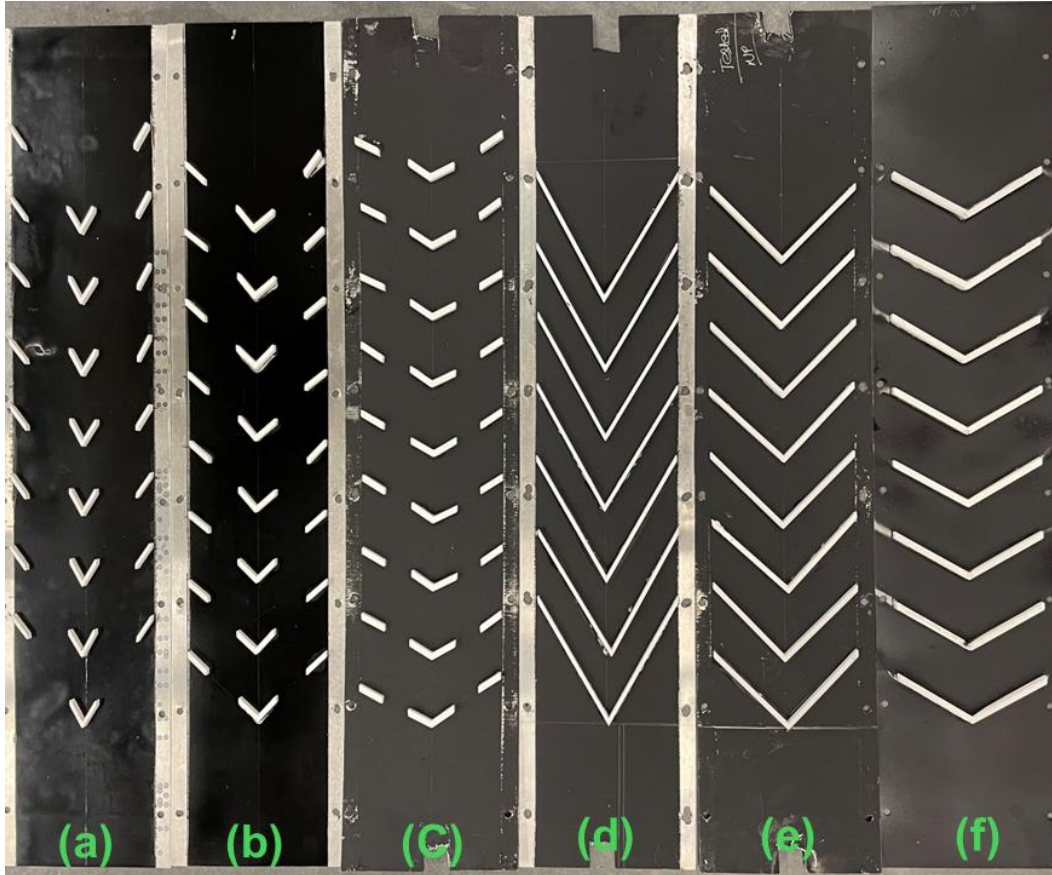


Figure 16: V shaped Rib turbulator photograph have been used in this study (a) Broken 60°, (b) Broken 45°, (c) Broken 30°, (d) Continuous 60°, (e) Continuous 45°, (f) Continuous 30°.

In this experimental study a total set of 6 different rib turbulators have been studied at extremely high Reynolds number ranging from 100,000 – 400,000. The rib shapes include 30°, 45°, 60° V shaped, both traditional continuous and broken ribs, as shown in Figure 16. The first rib feature was positioned 4 inches downstream from the test section beginning, with a rib height-to-hydraulic diameter ratio ( $e/D_h$ ) of 1/20 and a rib height-to-pitch ratio ( $e/p$ ) of 10. These parameters were held constant to primarily examine the effect of the angle of attack and to compare the thermal-hydraulic performance of broken versus traditional rib configurations by minimizing channel blockage by decreasing feature height. The tested rib features were additively manufactured (AM) using ABS material.

### 2.3. Uncertainty analysis

The present study reports heat transfer and pressure drop results at varying Reynolds numbers. The uncertain quantities include Reynolds number, friction factor, normalized friction factor, Nusselt

number, Nusselt number ratio ( $Nu/Nu_0$ ), and thermal-hydraulic performance. The sequential perturbation method prescribed by Moffat [37] was employed for uncertainty estimation. The uncertainty in the Reynolds number, ranging from 100,000 to 400,000, varied between 18% and 1.9%. The uncertainty in the Nusselt number ratio ( $Nu/Nu_0$ ) ranged between 18% and 2%, while the uncertainty in the normalized friction factor ( $f/f_0$ ) was approximately 4.1%. Additionally, the uncertainty in the thermal-hydraulic performance calculation varied between 18% and 1.2%.

### **3. Results and discussion**

#### 3.1. Experimental results for smooth channel

First, smooth channels (i.e. the same setup but without rib turbulators) were studied to verify the experimental procedure using the Dittus-Boelter correlation. Figure 17 shows the detailed normalized Nusselt number distribution in the smooth channel for four distinct Reynolds number for  $Re_1 = 100,903$ ,  $Re_2 = 201,089$ ,  $Re_3 = 308,068$ ,  $Re_4 = 398,855$ . Note that the thin green colored hair-like features extending into the center of the test section in Figure 4 are the bulk fluid thermocouples, which are obstructing a small portion of the test surface and will be present in every data set.

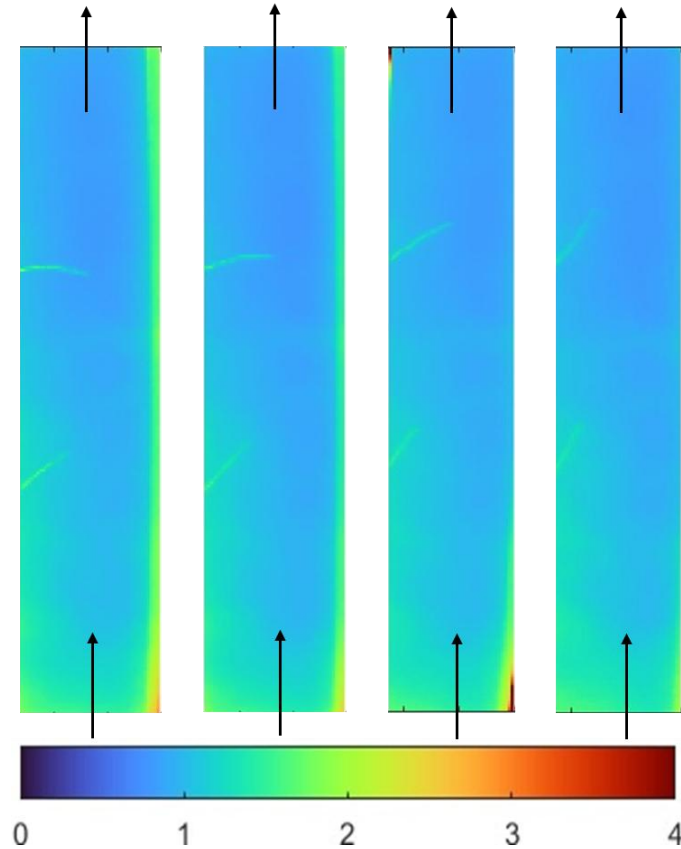


Figure 17: Detailed normalized Nusselt number distribution in smooth wall from left to right at four different Reynolds numbers,  $Re_1$ ,  $Re_2$ ,  $Re_3$ ,  $Re_4$

To gain a more comprehensive understanding of the flow dynamics, the 18-inch-wide test section was subdivided into nine distinct regions, with each region representing a 2-inch span along the bottom wall. A dense data acquisition strategy was employed, capturing 96 discrete measurement points within these nine regions. Figure 18 represents the spanwise normalized Nusselt number ratio for the smooth duct.

At the beginning of the test section in region # 0-1, the normalized Nusselt ratio is well above the value predicted by the Dittus-Boelter correlation, but along the length of the test section, the ratio displays the characteristic decay indicative of a developing boundary layer, eventually leveling out right at the Dittus-Boelter value for all smooth wall experiments. This suggests that despite the entry region, the flow is still not fully developed at the beginning of the test region, which is most likely due to inevitable misalignments between the channel sections. Nonetheless, towards the end of the test section in regions #5-9, the Nusselt number for the square channel is 2-8% lower than the values predicted by the Dittus-Boelter's correlation for fully developed turbulent tube flow

characteristics. This deviation aligns with the findings reported in References [36] and [23], which attribute such variations to marginal errors arising from differences in experimental techniques and instrumentation. Hence, these smooth wall tests demonstrate that the experimental setup is accurately predicting the heat transfer characteristics within an acceptable uncertainty range.

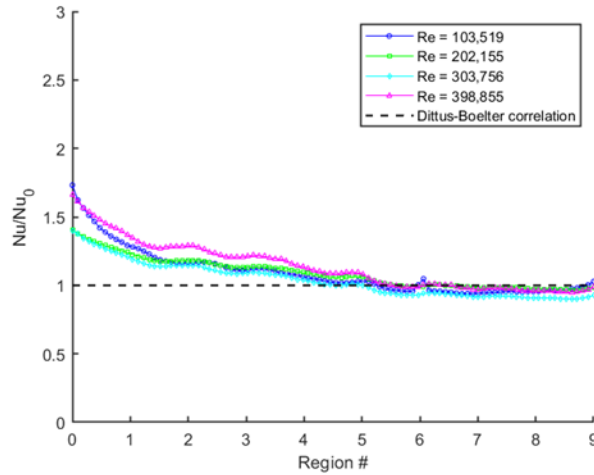


Figure 18: The local Nusselt number ratio for different regions in the smooth rectangular channel

### 3.2. Experimental results for traditional ribs and their performance

This section presents a detailed analysis of normalized local Nusselt numbers for various traditional rib configurations across four different Reynolds numbers. The Table 1 below provides data for the four Reynolds number cases.

Table 1: Reynolds number for tested each continuous ribs

| Sr. # | Rib name       | Re      |         |         |         |
|-------|----------------|---------|---------|---------|---------|
|       |                | 1       | 2       | 3       | 4       |
| 1     | 30° Continuous | 100,853 | 198,986 | 304,353 | 392,919 |
| 2     | 45° Continuous | 99,999  | 199,997 | 301,506 | 398,855 |
| 3     | 60° Continuous | 100,541 | 198,132 | 302,342 | 392,910 |

The normalized Nusselt number contours for the traditional V shaped ribs at 30°, 45° and 60° at bottom wall have been shown in Figure 19 (a), (b) and (c) respectively. Here, the flow direction is upward. As shown in this contour representation for the normalized Nusselt number distribution

for different ribs, it is noticeable that when the flow directly comes in contact with the first ribs, the flow is pushed towards the side walls due to the V shape of the ribs, which indicate the formation of the secondary flow consisting of counterrotating vortices that have been shown to greatly enhance heat transfer characteristics.

For each traditional rib configuration, as the Reynolds number increases, the normalized Nusselt ratio decreases as shown by the spanwise averaged Nusselt ratio values in Figure 20. This means that the relative enhancement specifically from the ribs is having less of an effect at higher Reynolds numbers compared to lower Reynolds numbers, indicating that the increasing turbulent strength is becoming the more dominant factor on the heat transfer performance as compared to the flow features generated by the ribs, such as boundary layer tripping and the counterrotating vortices. This results in a more uniform cooling at higher Reynolds numbers, which is reflected in the contour plots of Figure 19 which show that the surface has a quite uniform Nusselt distribution. This trend of diminishing heat transfer augmentation with increasing Reynolds number is consistent across both low Reynolds number regimes ( $\sim 90,000$ ) and extremely high Reynolds numbers ( $100,000\text{--}400,000$ ) for the continuous rib configurations, even when the rib height is reduced in this study. With that being said, the enhancement is still significant as compared to the Dittus-Boelter values, with the  $45^\circ$  V-shaped ribs outperforming the other configurations. This must be attributed to the modifications in vortex dynamics and the increased formation of secondary flow cells in the  $45^\circ$  V-shaped ribs, compared to the  $30^\circ$  and  $60^\circ$  angled ribs, which have a good agreement to prior results as well [38,39]. Furthermore, the results from both figures confirm that more homogeneous cooling is achieved with  $45^\circ$  V-shaped rib features.

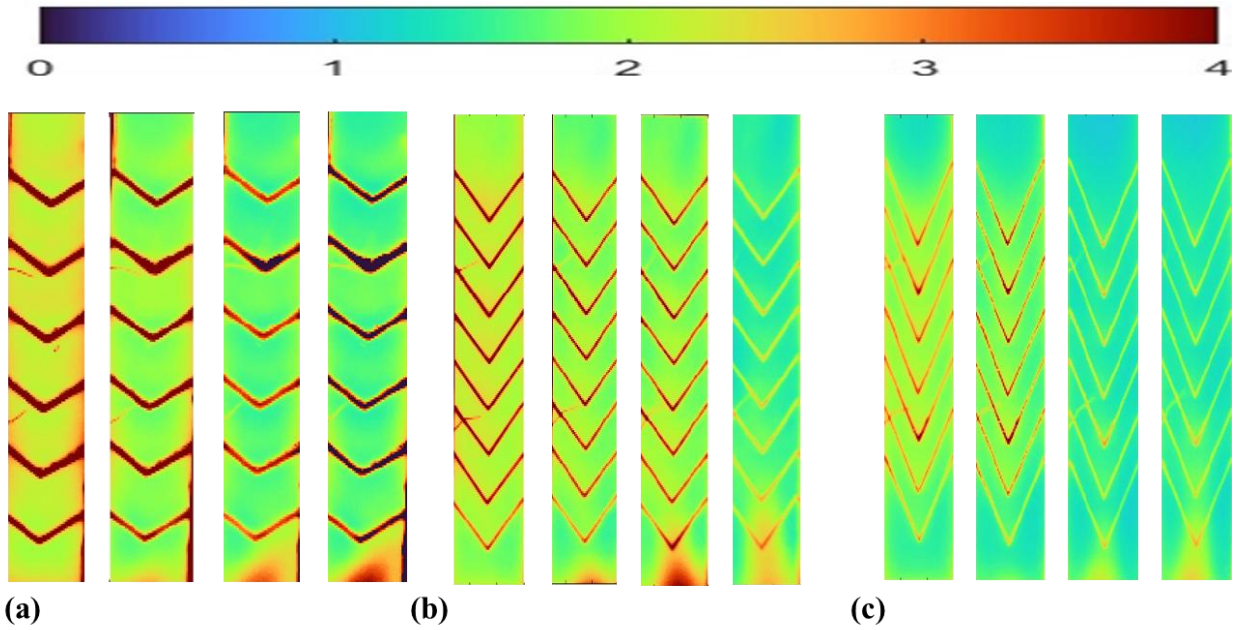


Figure 19: Detailed normalized Nusselt number distribution in (a) 30° traditional continuous ribs, (b) 45° traditional continuous ribs, (c) 60° traditional continuous ribs on bottom wall from left to right at four different Reynolds numbers,  $Re_1$ ,  $Re_2$ ,  $Re_3$ ,  $Re_4$ .

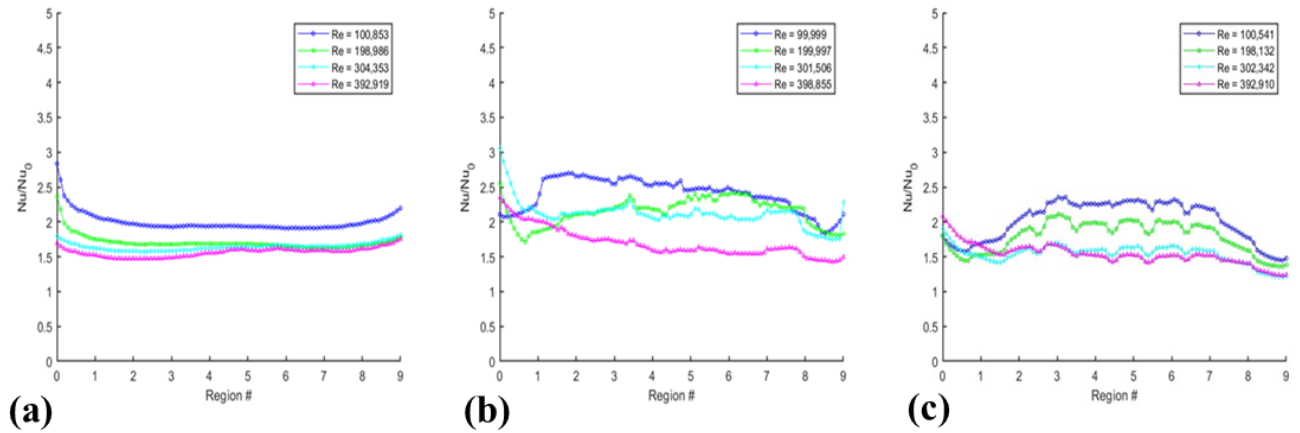


Figure 20: Detailed normalized spanwise Nusselt number distribution in (a) 30° traditional continuous ribs, (b) 45° traditional continuous ribs, (c) 60° traditional continuous ribs on bottom wall from left to right at four different Reynolds numbers,  $Re_1$ ,  $Re_2$ ,  $Re_3$ ,  $Re_4$ .

### 3.3. Experimental results for broken ribs and their performance

This section presents a detailed analysis of normalized Nusselt numbers for various broken rib configurations across four different Reynolds numbers. Table 2 below shows the actual test conditions for the four Reynolds number cases.

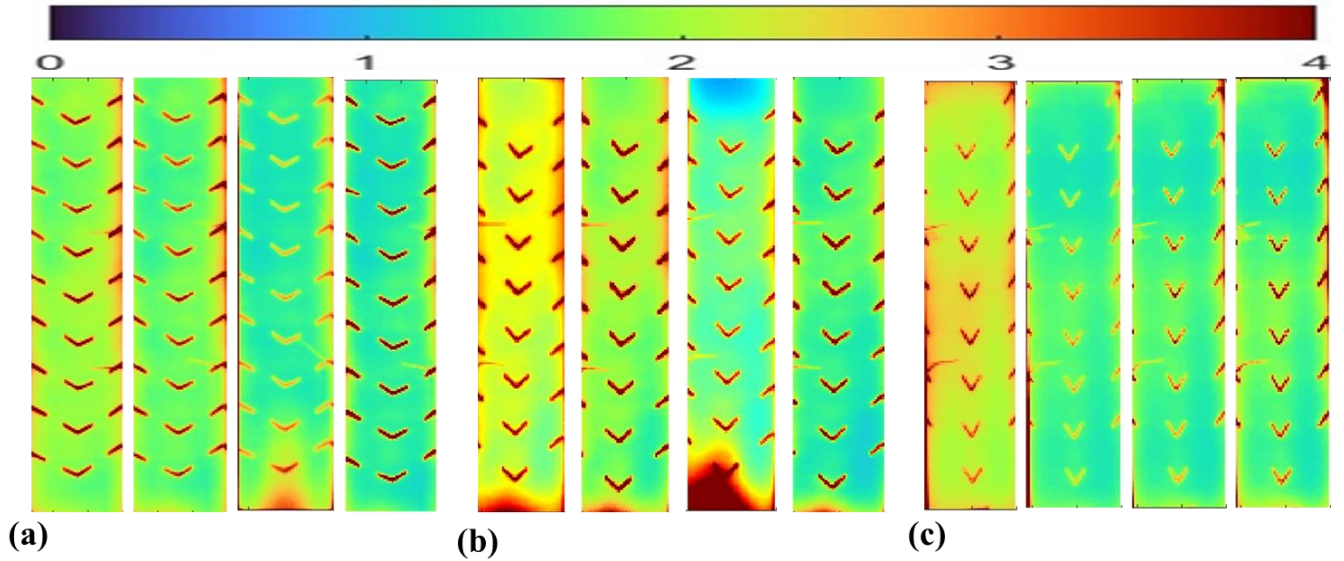
Table 2: Reynolds number for tested each broken ribs

| Sr. # | Rib name   | Re      |         |         |         |
|-------|------------|---------|---------|---------|---------|
|       |            | 1       | 2       | 3       | 4       |
| 1     | 30° Broken | 101,749 | 197,612 | 299,238 | 398,883 |
| 2     | 45° Broken | 101,749 | 200,803 | 304,950 | 399,793 |
| 3     | 60° Broken | 100,903 | 201,089 | 308,068 | 399,993 |

The normalized Nusselt number contours for the broken V shaped ribs features on 30°, 45° and 60° at bottom wall have been shown in Figure 21 (a), (b) and (c) respectively. It is evident that 45° angled ribs with broken features provide superior cooling performance compared to other configurations. From the normalized contours, it is observed that, for any given Reynolds number, the broken structures exhibit more efficient cooling performance than their traditional features at the same rib height. The broken rib structures enhance thermal performance by generating stronger swirl flow within the duct, which results in higher heat transfer coefficients at given Reynolds numbers compared to traditional features. Additionally, an alternative explanation could be that the 45° angle disrupts and redirects the flow symmetrically from the mainstream toward the sidewalls. This diversion, combined with the broken structure, promotes a more effective fluid mixing process, further enhancing heat transfer performance.

Figure 22 provides a comprehensive analysis of the spanwise normalized Nusselt number for broken rib structures. It is evident that, for any given Reynolds number, the normalized Nusselt number is highest for the 45° angled ribs, followed by the 30° and 60° rib configurations. Another key observation regarding the broken rib structure is that, at a given rib height, the 45° broken ribs offer a larger effective projected area, which systematically disrupts the velocity boundary layer and promotes stronger swirl generation. In contrast, the 60° broken rib structures exhibit reduced

Figure 21: Detailed normalized Nusselt numb



er distribution in (a) 30° broken ribs, (b) 45° broken ribs, (c) 60° broken ribs on bottom wall from left to right at four different Reynolds numbers,  $Re_1$ ,  $Re_2$ ,  $Re_3$ ,  $Re_4$ .

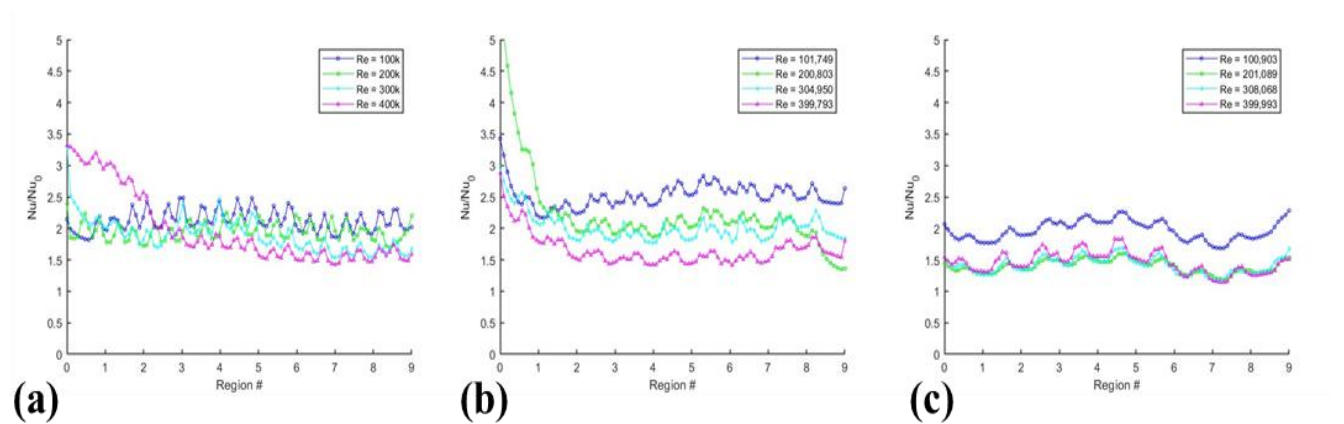


Figure 22: Detailed normalized spanwise Nusselt number distribution in (a) 30° broken ribs, (b) 45° broken ribs, (c) 60° broken ribs on bottom wall from left to right at four different Reynolds numbers,  $Re_1$ ,  $Re_2$ ,  $Re_3$ ,  $Re_4$ .

vortex formation due to their comparatively lower projected surface area on the bottom wall and their angle of attack. The 45° broken ribs, being evenly distributed along the bottom wall, not only enhance thermal performance but also provide better structural support for gas turbine hollow mid-core passages compared to the 30° and 60° broken ribs. This explains why the 45° configuration

results in more homogeneous cooling, making it a superior design choice for mid-core passages. Achieving homogeneous cooling efficiency can significantly extend the operational lifespan of gas turbine blades by minimizing thermal stress within the narrow hollow passages, thereby enhancing their durability and reliability during prolonged operation.

### 3.4. Comparison of overall thermal and hydraulic performance for the broken & traditional ribs

The previous sections described only the thermal performance of the rib configurations. However, there is always a tradeoff between enhancing thermal performance and increasing the pressure drop penalty. Hence, this section is dedicated to evaluating the overall thermal-hydraulic performance of the various rib configurations.

The globally averaged normalized Nusselt numbers across regions 1–9 is presented in Figure 23. The continuous rib structures are denoted by the letter “C”, while the broken structures are represented by “B”, corresponding to their respective angles of attack. Additionally, for a fair comparison with empirical correlations, the Dittus-Boelter line is also included in black color.

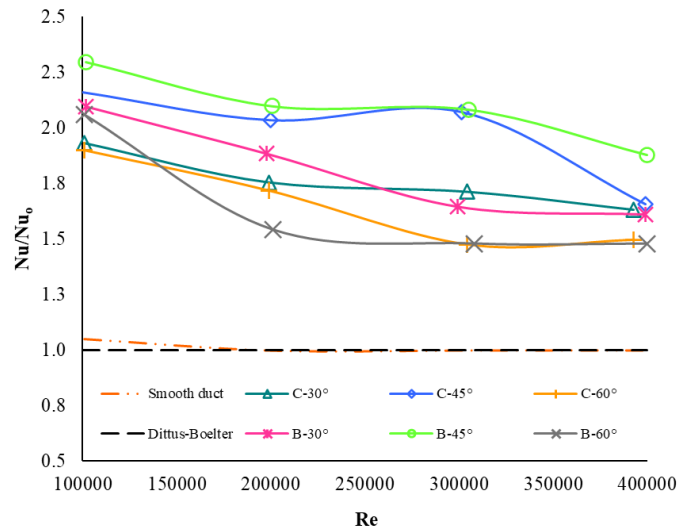


Figure 23: Comparison of overall Nusselt number enhancement.

From Figure 23, a qualitative observation suggests that heat transfer augmentation is strongly dependent on the inlet Reynolds number and its effect on cooling performance. As the Reynolds number increases, from approximately 100,000 to nearly 400,000, the boundary layer becomes progressively thinner, making it increasingly challenging to achieve a 2–3 times or higher enhancement in heat transfer (i.e., normalized Nusselt number) using rib features. Furthermore,

the broken V-shaped ribs exhibited the highest thermal performance among all tested configurations. While the continuous V-shaped ribs demonstrated comparable performance, they failed to match the thermal enhancement of the broken ribs at approximately 400,000 Reynolds number. This confirms the superior fluid mixing capabilities of the broken rib structures, as argued and scientifically justified in Section 3.3. Broken V-shaped ribs positioned at a 45° angle exhibited a heat transfer enhancement of approximately 14.47% and 19.24% compared to 30° and 60° broken ribs, respectively, at a Reynolds number of nearly 400,000 — the highest range tested in this study and a critical regime for achieving optimal heat transfer performance. The overall trend in heat transfer enhancement for the six different rib features tested at a Reynolds number of nearly 400,000 shows that the broken 45° ribs achieve the highest heat transfer enhancement, reaching 88% higher than a fully developed smooth wall flow condition.

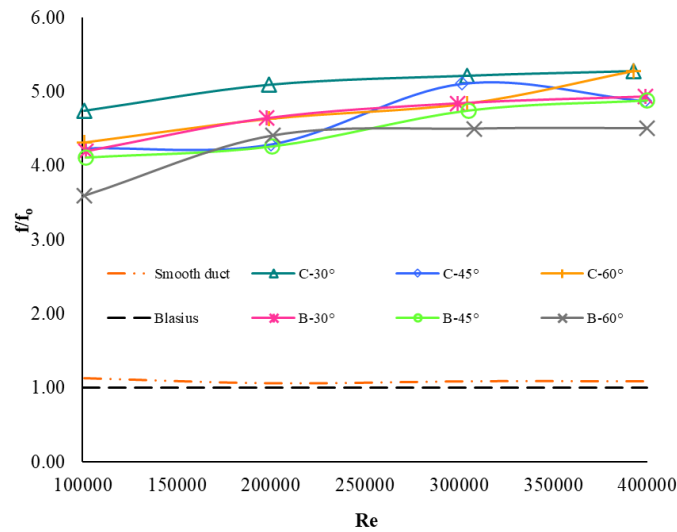


Figure 24: Comparison of overall Frictional losses.

Figure 24 presents a comparison of the normalized friction factor, as defined by the correlation provided in Equation 17, for various configurations. The friction factor was calculated based on the static pressure drop across the test section. The  $f/f_0$  ratio was observed to increase with Reynolds number, highlighting the importance of normalizing results for a ribbed channel relative to a non-ribbed channel. Among all configurations, the pressure penalty for the 30° continuous rib was the highest, while the broken 60° rib exhibited the lowest pressure drop, particularly at higher Reynolds numbers. The continuous 60° ribs (C 60°) showed the highest pressure penalty at a Reynolds number of nearly 400,000, whereas the broken 60° ribs (B 60°) had the lowest pressure

penalty at approximately 100,000 Reynolds number. Furthermore, the broken 45° ribs (B 45°) demonstrated superior thermal performance compared to the broken 30° ribs (B 30°) while also maintaining a lower pressure penalty than B 30°. This makes the B 45° ribs an optimal design choice for cooling passages, effectively balancing heat transfer enhancement and pressure drop efficiency.

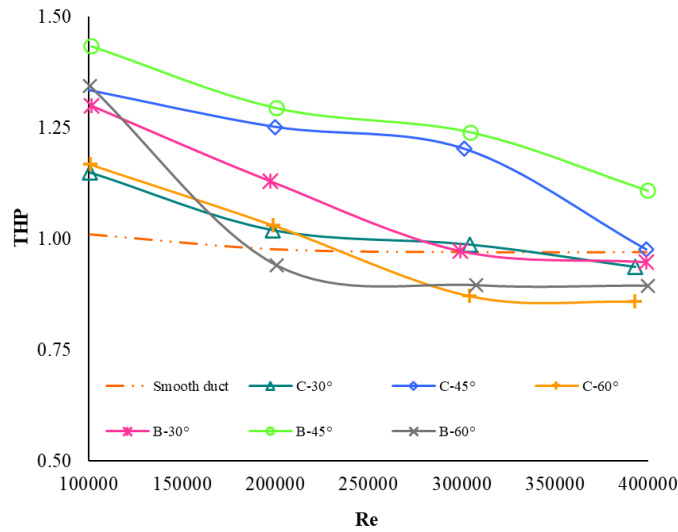


Figure 25: Variation in Thermal hydraulic performance with Reynolds number

Figure 25 illustrates the thermal-hydraulic performance (THP), calculated using Equation 7, as a function of the inlet Reynolds number. The results indicate that the thermal-hydraulic performance of broken ribs is higher than that of continuous-type ribs. The continuous-type rib configurations investigated in this study demonstrated superior thermal-hydraulic performance compared to other continuous rib shapes studied in previous research [5][8,14]. Although the THP of Broken 30° (B 30°) and Continuous 30° (C 30°) surpasses that of other configurations at higher Reynolds numbers, their values remain relatively close due to the trade-off between heat transfer enhancement and pressure drop penalty. This underscores the importance of understanding the influence of the angle of attack in gas turbine blade cooling technology and its impact on overall system performance. The present study proposes alternative rib shapes, particularly broken rib structures, which have demonstrated promising performance in terms of both heat transfer enhancement and thermal-hydraulic efficiency. Furthermore, manufacturing 45° V-shaped and 60° V-shaped ribs is often impractical, as the most commonly used rib shape in modern gas turbine

blades is the 45° parallel rib configuration, which aligns with findings from previous studies. Consequently, the broken 45° V-shaped ribs, particularly with a reduced rib height ( $e/D_h = 1/20$ ), provide an effective alternative to traditional continuous parallel rib designs, offering enhanced heat transfer and improved thermal-hydraulic performance. Additionally, it is crucial to examine the behavior of thermal-hydraulic performance at higher Reynolds numbers. Qualitative observations indicate that while THP decreases as Reynolds number increases, it remains above unity, demonstrating that reducing rib height and incorporating broken structures is an optimal solution for achieving THP values greater than 1 in gas turbine mid-core cooling passages operating at extremely high Reynolds numbers.

#### 4. Conclusion

This study presents detailed measurements of the heat transfer coefficient for six different rib configurations, with a rib-to-hydraulic diameter ratio –  $e/D_h=1/20$ , namely Broken 30°, 45°, & 60°, and Continuous 30°, 45°, & 60°. Heat transfer and pressure drop experiments were conducted over an extremely high Reynolds number range of 100,000 to 400,000, with a particular focus on land-based gas turbines and other gas turbines that operate at extremely high temperature and pressure conditions. The heat transfer measurements have been analyzed in detail and presented in spanwise-averaged, and globally averaged results. Some of the key conclusions from this study are as follows:

- Broken rib features help mitigate the pressure drop penalty by significantly reducing the overall additional surface area inside a hollow passage. As a result, thermal-hydraulic performance improves, and the pressure drop penalty can be further minimized by decreasing the rib feature size.
- The broken V-shaped 45° ribs outperform all other configurations studied in this paper, providing not only higher heat transfer augmentation across both low and high Reynolds number ranges but also superior thermal-hydraulic performance. Additionally, they offer better structural support in hollow mid-core passages and contribute to more homogeneous cooling.
- Broken V-shaped ribs positioned at a 45° angle exhibited the highest heat transfer enhancement among the six tested configurations at a Reynolds number of nearly 400,000, achieving 14.47% and 19.24% higher enhancement compared to 30° and 60° broken ribs, respectively, and 88% greater than a fully developed smooth wall flow condition.
- The heat transfer enhancement is strongly influenced by the angle of attack and the rib geometry, where broken ribs achieve greater enhancement compared to continuous ribs.

## CHAPTER 3

### Experimental Study of Rib Height and Pitch Effects on Thermal-Hydraulic Performance in Gas Turbine Cooling at High Reynolds Numbers

Naimish Pandya<sup>a</sup>, Srinath V. Ekkad<sup>a</sup>

*<sup>a</sup>Department of Mechanical and Aerospace Engineering North Carolina State University  
Raleigh, NC, USA*

This chapter builds upon the analysis presented in Chapter 2 by focusing on the thermal-hydraulic performance of the most effective rib turbulator configuration previously identified—namely, the 45° broken rib. The objective of this extended study is to evaluate the influence of varying rib height-to-hydraulic diameter ratios ( $e/D_h = 1/10, 1/25, \text{ and } 1/30$ ) at a fixed, closely spaced pitch of 2 inches. Furthermore, a comparative assessment is conducted across a broader set of configurations, encompassing  $e/D_h$  values of 1/10, 1/20, 1/25, and 1/30, at two distinct pitch to height ratio of 12.5 and 4. This parametric investigation aims to elucidate the combined effects of rib height and pitch on the thermal-hydraulic behavior of internal cooling channels subjected to extremely high Reynolds numbers. Experimental methodologies, including measurement techniques and associated uncertainty analysis, have already been detailed in Chapter 2 and are thus not reiterated here. This chapter focuses directly on the results, analyzing the thermal and hydraulic performance outcomes corresponding to the various geometric configurations tested. A total of six rib turbulator configurations were experimentally investigated under Reynolds numbers ranging from 100,000 to 400,000.

The studied geometries, all based on the 45° broken rib design, are illustrated in Figure 26, and include variations in both rib height and pitch to comprehensively assess their influence on flow and heat transfer characteristics.

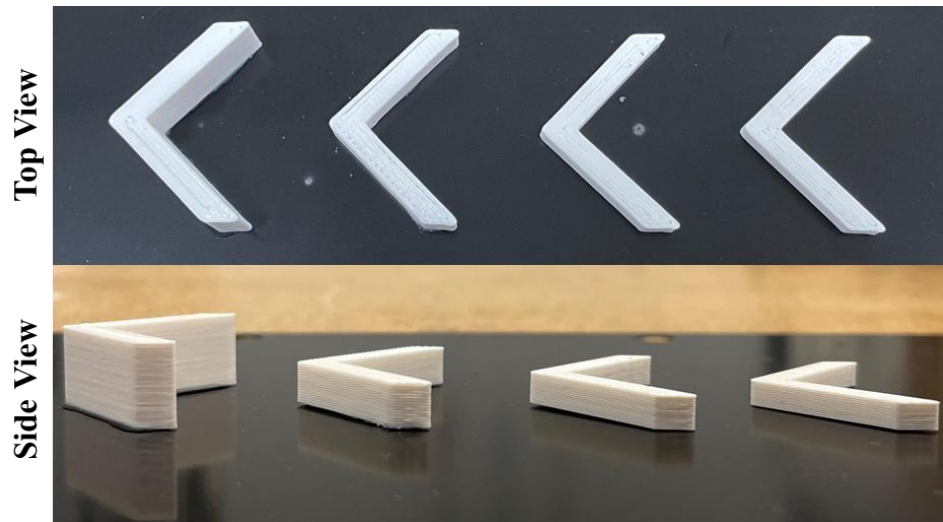


Figure 26: Rib turbulator configurations evaluated in this study from left to right, the rib height-to-hydraulic diameter ratios ( $e/D_h$ ) are 1/10, 1/20, 1/25, and 1/30.

## 1. Results and discussion

### 1.1. Experimental results for traditional ribs and their performance

This section presents a detailed analysis of normalized local Nusselt numbers for various traditional rib configurations across four different Reynolds numbers. The Table 3 below provides data for the four Reynolds cases.

Table 3: Reynolds number for tested each broken ribs placed at 45° angle

| Sr. # | Rib name                   | Re      |         |         |         |
|-------|----------------------------|---------|---------|---------|---------|
|       |                            | 1       | 2       | 3       | 4       |
| 1     | 45° Broken, $e/D_h = 1/10$ | 103,519 | 201,215 | 303,249 | 403,156 |
| 2     | 45° Broken, $e/D_h = 1/20$ | 99,999  | 199,997 | 301,506 | 398,855 |
| 3     | 45° Broken, $e/D_h = 1/25$ | 102,372 | 202,155 | 303,756 | 402,058 |
| 4     | 45° Broken, $e/D_h = 1/30$ | 103,519 | 202,189 | 301,009 | 405,129 |

Figure 27 presents the normalized Nusselt number contours on the bottom wall of the cooling channel for the broken 45° V-shaped rib configurations with three different rib height-to-hydraulic diameter ratios: (a)  $e/D_h = 1/10$ , (b)  $e/D_h = 1/25$ , and (c)  $e/D_h = 1/30$ . The results clearly indicate that the 45° broken rib design enhances cooling performance compared to the baseline and other rib geometries investigated in the previous chapter. Notably, for a given Reynolds number, reducing the rib height from  $e/D_h = 1/10$  to  $e/D_h = 1/25$  leads to an increase in the normalized Nusselt number, indicating improved heat transfer. However, a further reduction to  $e/D_h = 1/30$  does not yield significant additional enhancement, suggesting diminishing returns at lower rib heights. The contour plots reveal a relatively uniform distribution of the normalized Nusselt number, signifying homogeneous wall cooling. As the normalized Nusselt number is strongly governed by the temperature difference between the wall and the bulk fluid, which directly influences the local heat transfer coefficient, the observed spatial variation reflects the complex flow and thermal interactions induced by the rib geometry.

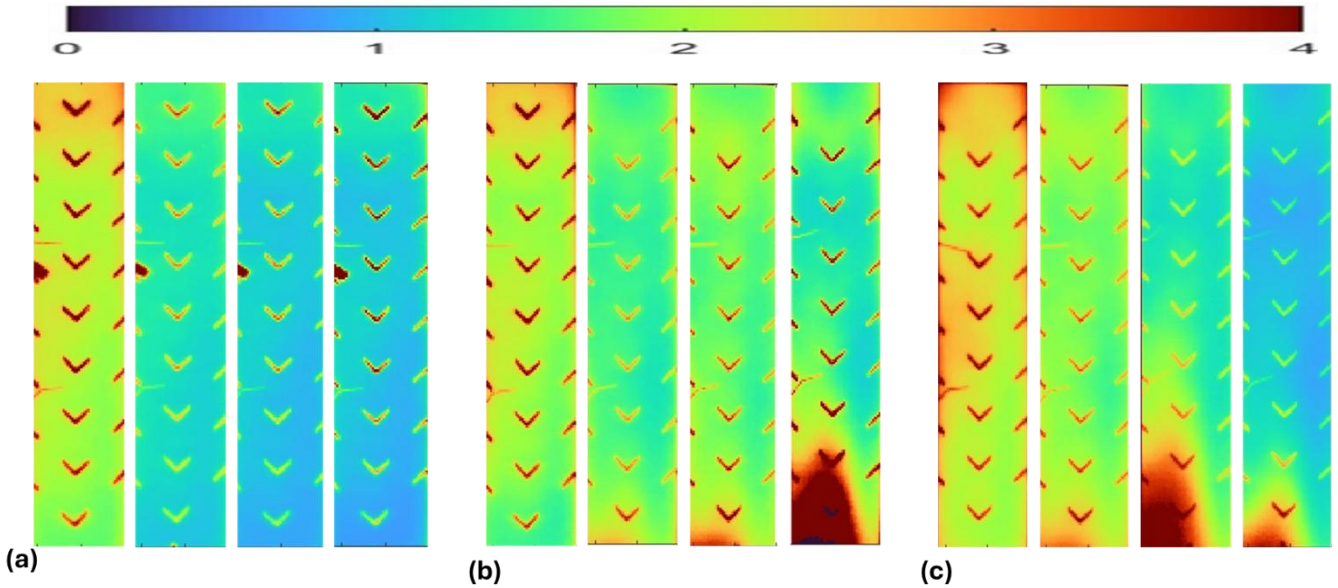


Figure 27: Detailed normalized Nusselt number distributions on the bottom wall for 45° broken V-shaped ribs at three rib height-to-hydraulic diameter ratios: (a)  $e/D_h = 1/10$ , (b)  $e/D_h = 1/25$ , and (c)  $e/D_h = 1/30$ . Contours are shown from left to right for four Reynolds numbers:  $Re_1$ ,  $Re_2$ ,  $Re_3$ , and  $Re_4$ .

The broken V-shaped ribs effectively redirect the main flow toward the sidewalls, generating strong secondary vortices. These vortical structures enhance local mixing and disrupt the thermal boundary layer, particularly near the sidewalls, resulting in localized heat transfer augmentation. This flow redirection contributes to a more effective thermal management strategy in internal cooling applications, especially under high Reynolds number conditions. To investigate the effect of rib pitch, an additional experiment was conducted with a closely spaced configuration maintaining a pitch-to-height ratio of  $p/e = 4$ . The corresponding normalized Nusselt number contours are presented in Figure 28. While reducing the pitch does not significantly increase the overall Nusselt number compared to other configurations, it results in a more uniform heat transfer distribution across the cooling surface. Such uniformity is advantageous in mitigating thermal gradients and preventing local hot spots, which are critical considerations in high-performance gas turbine cooling systems.

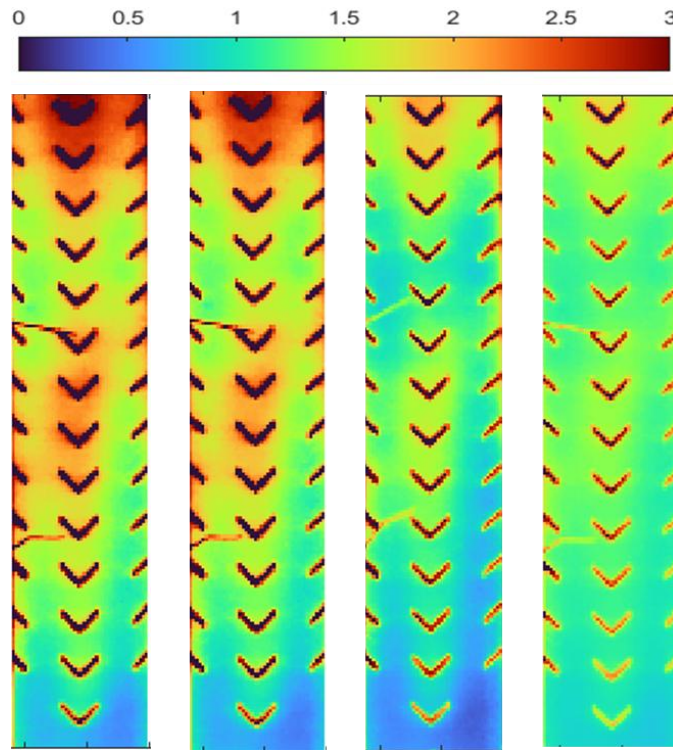


Figure 28: Normalized Nusselt number distributions on the bottom wall for 45° broken V-shaped ribs with  $e/D_h = 1/25$  and pitch-to-height ratio  $p/e = 4$ . Results are shown from left to right for Reynolds numbers: 102,157; 200,304; 303,309; and 399,993.

To comprehensively evaluate the combined influence of rib angle, height, and pitch on thermal performance, all tested configurations were compared in terms of their normalized Nusselt number behavior over a wide Reynolds number range. Figure 29 presents the variation of normalized Nusselt number ( $Nu/Nu_0$ ) as a function of Reynolds number ( $Re$ ) for both conventional (C) and broken (B) rib geometries, spanning various angles and height-to-hydraulic diameter ratios ( $e/D_h$ ). Baseline results for a smooth duct and the Dittus-Boelter correlation are also included for reference.

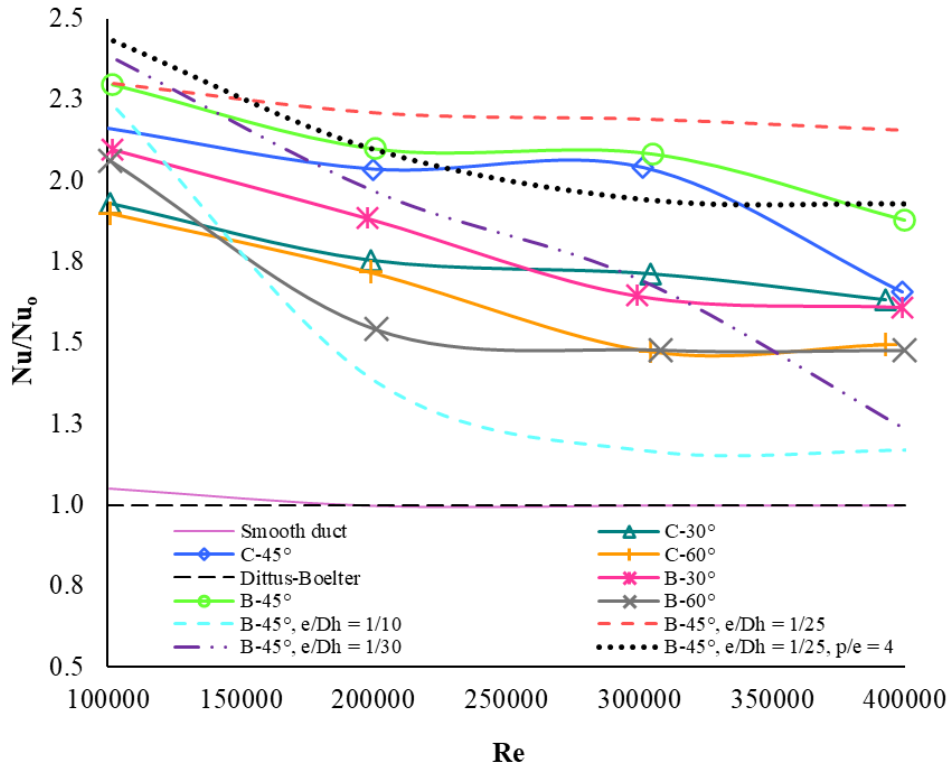


Figure 29: All combined geometry and normalized Nusselt number as a function of Reynolds number

Among all configurations, the 45° broken rib with  $e/D_h = 1/25$  and a pitch of 12.5 inches consistently demonstrates the highest thermal enhancement throughout the tested Reynolds number range of 100,000–400,000. The same rib design with a reduced pitch ( $p/e = 4$ ) also achieves strong performance, offering more uniform behavior across increasing Reynolds numbers. Conversely, the B-45°,  $e/D_h = 1/30$  case exhibits reduced enhancement, indicating a performance decline with excessive rib height reduction. This suggests that at ultra-high Reynolds numbers—where boundary layers are thin—increasing rib height beyond an optimal threshold may lead to adverse flow resistance without significant thermal benefits.

The 30° and 60° broken rib configurations, along with all continuous rib designs at 30°, 45°, and 60°, generally display lower heat transfer enhancements, reaffirming the superior performance of optimally configured 45° broken ribs. These results underscore the critical role of geometric optimization, particularly rib angle, height, and spacing—in achieving efficient thermal-hydraulic performance in internal cooling passages operating under extreme Reynolds number conditions.

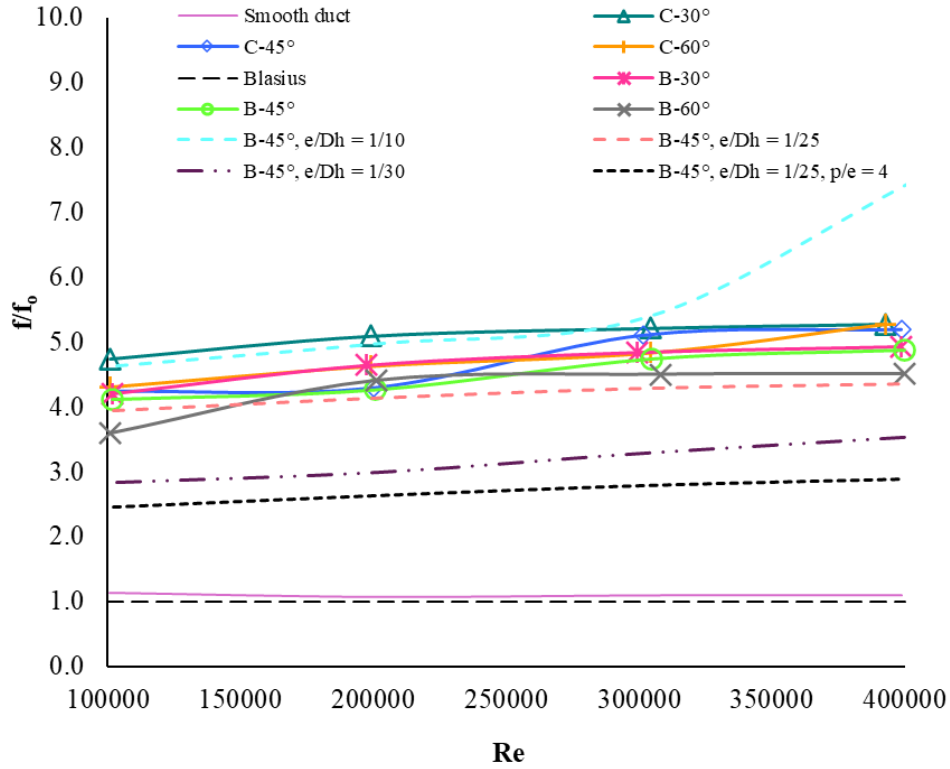


Figure 30: All combined geometry and normalized frictional losses as a function of Reynolds number

Figure 30 presents the variation of normalized friction factor ( $f/f_0$ ) as a function of Reynolds number for a range of rib turbulator configurations, including conventional (C) and broken (B) rib geometries at different angles and height-to-hydraulic diameter ratios ( $e/D_h$ ). The results are benchmarked against both a smooth duct and the classical Blasius correlation for turbulent flow in smooth pipes. As expected, all ribbed configurations exhibit significantly higher friction factors than the smooth duct due to increased surface roughness and flow obstruction. Among the tested designs, the B-45°,  $e/D_h = 1/10$  configuration exhibits the highest friction penalty, especially at higher Reynolds numbers. In contrast, the B-45°,  $e/D_h = 1/25$  with reduced pitch ( $p/e = 4$ ) demonstrates the lowest frictional resistance among all ribbed cases, maintaining  $f/f_0$  values below 3 across the entire Reynolds number range. The B-45°,  $e/D_h = 1/30$  design shows moderate pressure loss characteristics, reinforcing the idea that smaller rib heights can reduce flow resistance while still enhancing heat transfer (as seen in previous figures). Continuous rib configurations (C-30°, C-45°, C-60°) generally impose higher friction compared to their broken counterparts, particularly at steeper angles. Overall, the results emphasize the importance of geometric

optimization—not only for thermal enhancement but also for minimizing hydraulic losses, which are critical for improving the overall thermal-hydraulic performance of internal cooling systems at ultra-high Reynolds numbers.

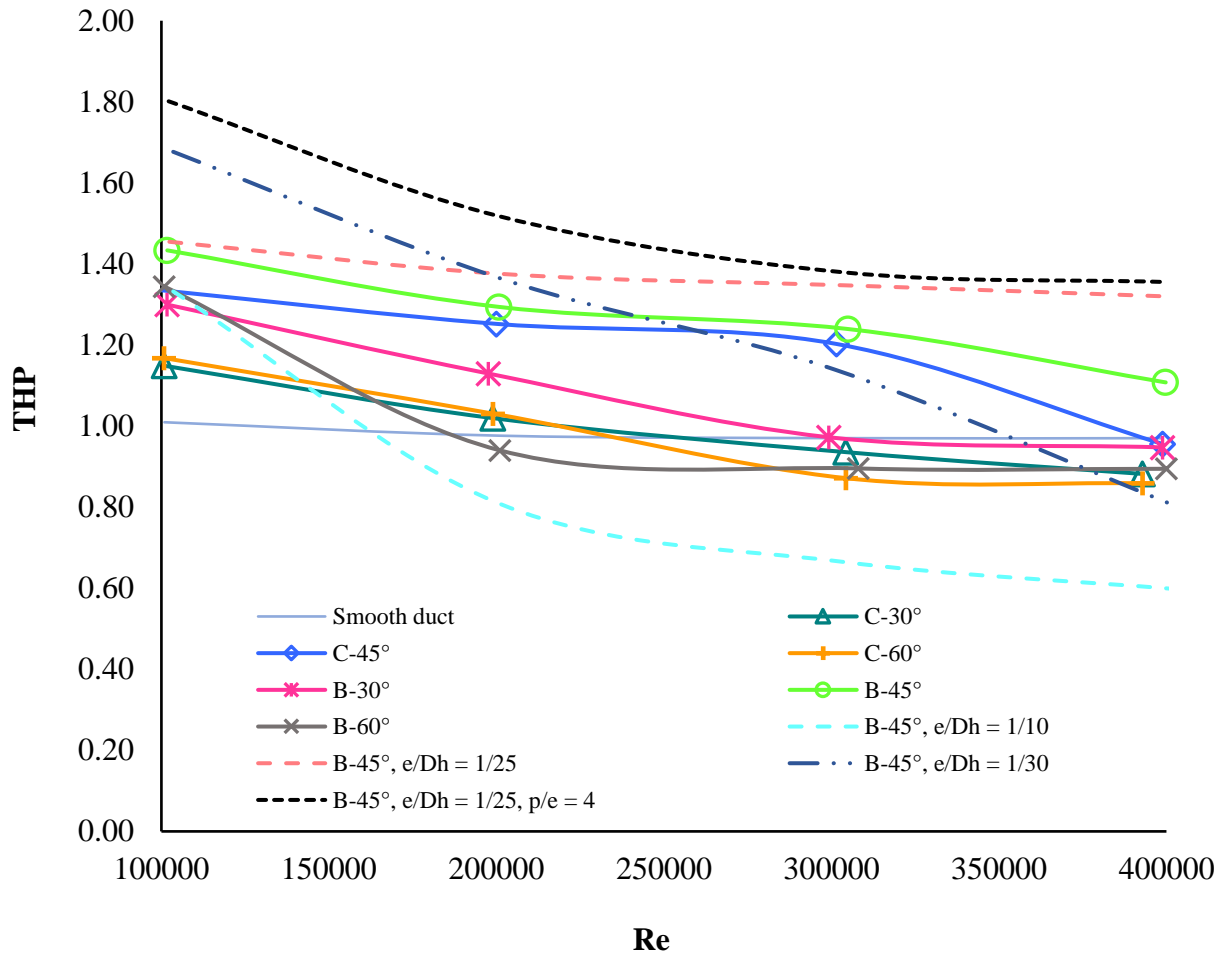


Figure 31: THP for All combined geometry as a function of Reynolds number

The comparison between Figure 29 and Figure 30 highlights the trade-off between heat transfer and pressure loss. The B-45°,  $e/D_h = 1/25$  with  $p = 12.5$  shows the best thermal performance with moderate friction, while B-45°,  $e/D_h = 1/10$  offers high heat transfer but with significant pressure drop. The B-45°,  $e/D_h = 1/25$ ,  $p/e = 4$  strikes an optimal balance, combining good thermal enhancement with low flow resistance—making it the good efficient design overall.

Figure 31 presents the variation of Thermal-Hydraulic Performance (THP) as a function of Reynolds number (Re) for all tested rib configurations. THP serves as a comprehensive metric to evaluate the overall effectiveness of a design by balancing heat transfer enhancement against frictional losses. A THP value greater than 1 indicates a net performance gain over the smooth duct baseline. Among all cases, the 45° broken rib with  $e/D_h = 1/25$  and reduced pitch ( $p/e = 4$ ) consistently exhibits the highest THP across the full Reynolds number range, clearly identifying it as the most effective configuration in achieving enhanced thermal performance with relatively low hydraulic penalty. In contrast, although the B-45°,  $e/D_h = 1/10$  configuration achieves high heat transfer, its relatively high friction factor significantly reduces THP, especially at higher Reynolds numbers. Other configurations, including continuous ribs and higher rib heights, generally exhibit declining THP values as Reynolds number increases, emphasizing the diminishing returns of aggressive geometries under ultra-high Reynolds number condition also matches with the state-of-art. This analysis highlights the importance of optimizing rib geometry not solely for maximum heat transfer, but for a balanced design that delivers superior thermal-hydraulic efficiency in practical high-speed cooling applications.

## 2. Conclusion

- The B-45°,  $e/D_h = 1/25$ ,  $p/e = 4$  configuration consistently demonstrates the highest overall thermal-hydraulic performance (THP), confirms its superior balance between thermal enhancement and pressure drop.
- The B-45°,  $e/D_h = 1/30$  configuration shows a high initial THP at low Reynolds number but a significant decline at  $Re = 405,129$ . This indicates that overly reducing rib height diminishes heat transfer at higher flow rates due to less interaction with the thinning boundary layer.
- Broken ribs consistently outperform continuous (C-type) ribs in thermal-hydraulic performance. For example, B-45°,  $e/D_h = 1/25$ ,  $p = 12.5$  maintains  $THP > 1.29$ , whereas the best-performing C-rib (C-45°) drops to 0.98 at higher Reynolds numbers.
- Reducing pitch from 12.5 to  $p/e = 4$  in the B-45°,  $e/D_h = 1/25$  case leads to higher THP across the board, improving from 1.45 (at  $Re = 102,372$ ) to 1.80 (at  $Re = 102,157$ ), indicating that closely spaced broken ribs optimize cooling uniformity while minimizing pressure losses.

## CHAPTER 4

### Enhanced Internal Cooling Performance in Gas Turbines Blades Using non-conventional features at Ultra-High Reynolds Numbers

Naimish Pandya<sup>a</sup>, Wesley Fisher<sup>a</sup>, Srinath V. Ekkad<sup>2,a</sup>

*<sup>a</sup>Department of Mechanical and Aerospace Engineering North Carolina State University  
Raleigh, NC, USA*

As turbine engines continue to operate at increasingly higher thermal loads, the need for advanced internal cooling strategies becomes critical for ensuring component durability and performance. This study investigates the thermal-hydraulic behavior of three novel rib and fin turbulator configurations—Continuous Chevron Pattern Fins (CCPF), V-Shaped Double Broken Ribs (VSDBR), and Broken Chevron Pattern Fins (BCPF)—within a single-pass rectangular cooling channel under extremely high Reynolds number conditions ( $Re = 100,000$  to  $600,000$ ). High-fidelity numerical simulations were conducted using the Realizable  $k-\epsilon$  turbulence model with non-equilibrium wall functions, validated against experimental data for VSDBR geometries. Detailed analysis of normalized Nusselt number, friction factor, and thermal-hydraulic performance (THP) was performed to evaluate the effectiveness of each design. Results show that the VSDBR configuration yields the highest heat transfer enhancement ( $Nu/Nu_0 \approx 2.4$ ) across the range but incurs the highest frictional penalties (up to 34%). BCPF, while achieving moderate heat transfer enhancement, demonstrates significantly lower friction growth and maintains THP above unity at higher Reynolds numbers. Flow visualizations reveal that VSDBR induces strong secondary vortices and enhanced mixing, leading to superior thermal augmentation, whereas BCPF facilitates favorable boundary layer reattachment and uniform flow recovery. The CCPF

---

<sup>2</sup>Corresponding author:  
E-mail address: [sekkad@ncsu.edu](mailto:sekkad@ncsu.edu)

design shows limited thermal-hydraulic efficiency due to uninterrupted surface coverage that inhibits flow reattachment. Overall, the study underscores the importance of feature distribution, rib shape, and pitch spacing in high-Re internal cooling designs and identifies BCPF as a promising configuration for balancing heat transfer and pressure drop in turbine blade mid-core cooling passages.

## 1. Introduction

The gas turbine industry continues to advance toward higher operating temperatures to enhance engine efficiency, making the effective cooling of turbine blades a critical design requirement. Among the various internal cooling strategies, rib turbulator cooling remains one of the most widely adopted techniques [1,40–42], wherein relatively cooler air, bled from the compressor, is routed through ribbed internal passages to extract heat from the blade surfaces. Most existing experimental studies on ribbed channels are performed under scaled conditions, ensuring similarity in Reynolds and Prandtl numbers, and have contributed extensively to the understanding of heat transfer and pressure loss characteristics associated with sharp-edged rib geometries. In practical applications, however, achieving such sharp-edged ribs is challenging—particularly in aviation gas turbines, where the small size of blades and coolant passages makes precise casting difficult. Moreover, casting die wear over time leads to rib rounding, a phenomenon increasingly observed even in larger land-based turbines. These systems typically operate at significantly higher Reynolds numbers, often reaching up to  $\sim 600,000$ . Despite the prevalence of rib rounding in real-world engines, there exists a limited number of studies that address its impact—especially under such extreme flow conditions—using either experimental or numerical approaches [5,8,19]. This notable gap in literature underscores the necessity for further investigation into the thermal-hydraulic behavior of suitable rib geometries, particularly under extremely high Reynolds number regimes, through advanced simulation techniques as well.

Kumar and Pathak [33] investigate heat transfer enhancement in a rectangular cooling channel using compound configurations of  $45^\circ$  V-ribs and broken V-ribs combined with spherical dimples, employing the  $k$ - $\epsilon$  turbulence model with a scalable wall function. Simulations show that the highest heat transfer enhancement ( $Nu/Nu_0 = 2.46$ ) occurs with 1.5 mm high V-ribs and 4.0 mm deep dimples, while the maximum thermal performance factor (1.205) is achieved with 1.0

mm ribs and 2.0 mm dimples. Zhang et al. [30] evaluate turbulent flow and convective heat transfer in turbine blade internal cooling channels using round-edged ribs with oblique and transverse rib arrangements. Results show that the oblique rib configuration achieves a maximum heat transfer enhancement ( $Nu/Nu_0$ ) of 2.1 and a friction factor ratio ( $f/f_0$ ) of 2.9, while the transverse ribs provide a lower  $Nu/Nu_0$  of 1.8 and a higher  $f/f_0$  of 3.4 over a Reynolds number range of 20,000 to 80,000. Thus, oblique ribs offer better thermal performance by enhancing heat transfer with relatively lower pressure loss. They also found that the Realizable  $k-\epsilon$  model exhibited the lowest deviation of 39.86% compared to experimental results in ribbed channels, making it the most accurate among the  $k-\epsilon$  model family in predicting heat transfer performance. Promvong et al. [43] investigate the thermal performance of single and innovative double V-baffles in a heat exchanger, focusing on vortex formation and flow impingement. Results show that double V-baffles enhance heat transfer by 3–10% and reduce pressure loss by 10–32% compared to single V-baffles, yielding a maximum thermal enhancement factor (TEF) of 3.21. Luo et al. [44] present a DNA-shaped twisted tape turbulator (SSTT) to enhance heat transfer in heat exchanger tubes, testing pitch ratios from 1 to 4 mm. The optimal pitch of 2 mm improves heat transfer by 125% over a plain tube. When combined with a helical coiled wire, the heat transfer coefficient increases by 142%, with a 960% rise in pressure drop, resulting in a thermal performance factor of 1.31 – a 20% gain over conventional twisted tapes. Simulations using various RANS models show that the Realizable  $k-\epsilon$  model offers the best accuracy, with only 39.86% deviation from experiments, due to its strength in predicting swirling flows and near-wall behavior at high Reynolds numbers. Srivastav et al. [45] investigates the thermal performance of a solar air heater equipped with a submerged impinging jet (SAHSIJ), focusing on optimizing jet spacing ratio, jet angle, and Reynolds number in the range of 3000–18000. Computational simulations were carried out using the Realizable  $k-\epsilon$  turbulence model, chosen for its ability to accurately predict complex flow behaviors such as jet impingement and recirculation. The best configuration jet spacing ratio of 0.217 and jet angle of  $85^\circ$  at  $Re = 15000$  – achieves a Nusselt number enhancement of 5.70–6.78, a thermo-hydraulic performance factor of 2.92, and a maximum thermal efficiency of 75.1%.

Zhang et al. [46] conducted a numerical investigation into film cooling effectiveness and flow loss associated with a shark-skin-inspired composite structure. Utilizing computational fluid dynamics (CFD) techniques, they employed the Realizable  $k-\epsilon$  turbulence model to simulate the complex flow behaviors inherent in film cooling applications. Their results demonstrated that bio-

inspired design significantly enhances cooling performance, achieving higher level of cooling effectiveness compared to traditional configurations. In their study, Maurer et al. [18] conducted experimental and CFD analyses to evaluate heat transfer and pressure loss in a rectangular channel equipped with 45° V-shaped ribs. Using CFD simulations alongside experiments, they assessed the impact of rib-induced turbulence on thermal-hydraulic performance. The results showed that the V-ribbed configuration achieved a Nusselt number ratio of up to 2.0, indicating a twofold increase in heat transfer compared to a smooth channel, while the friction factor ratio increased to 2.8, reflecting the associated pressure loss penalty. Singh et al. [11] combined experimental and numerical techniques to analyze heat transfer in a two-pass ribbed square duct, demonstrating that V-shaped and 45° angled ribs yielded superior heat transfer enhancement relative to W- and M-shaped configurations. . Ravi et al. [12] conducted a computational study on 45°, V-shaped, W-shaped, and M-shaped ribs, concluding that V-shaped ribs outperformed others by 7% in heat transfer enhancement, albeit with a 19% higher pressure penalty. Singh et al. [10] examined a square duct featuring a crisscross rib topology and found similar Nusselt number ratios ( $Nu/Nu_0$ ) of 2.7–3.1 across Reynolds numbers ranging from 30,000 to 60,000. Maurer et al. [18] analyzed V-shaped features and their performance under extremely high Reynolds number conditions using both CFD and experimental approaches. Their main findings reveal that reducing the pitch-to-rib height ratio by 10 decreases the pressure drop penalty while enhancing heat transfer and thermal performance. Thianpong et al. [29] examines heat transfer enhancement in a square duct with V-shaped flapped baffles for Reynolds numbers 3,000–21,000 using the finite volume method and Realizable  $k$ - $\epsilon$  model. Their key parameters include blockade ratio ( $BR = 0.05$ – $0.3$ ), flap angle ( $\beta = 0^\circ$ – $90^\circ$ ), hole diameter ratio ( $dR = 0.5$ – $0.8$ ), and attack angle ( $\alpha = 60^\circ$ – $30^\circ$ ). Results show that a flapped baffle with  $\beta = 20^\circ$  and  $BR = 0.25$  achieves  $Nu/Nu_0 = 8.4$  and thermal enhancement factor  $\sim 2.49$  at the lowest Re. Zhang et al. [30] numerically investigates turbulent flow and convective heat transfer in turbine blade cooling channels for a wide Reynolds number  $Re = 20,000$ – $80,000$ . Results reveal that oblique ribs outperform transverse ribs, achieving higher heat transfer and lower friction losses. The study establishes the relationship between secondary vortices and turbulent kinetic energy, optimizing heat transfer by adjusting rib height ( $e/D_h = 0.047$ – $0.101$ ) and rib spacing ( $p/e = 10$ – $15$ ). The optimal configuration ( $e/D_h = 0.062$ ,  $p/e = 15$ ) maximizes the performance factors. Dinh et al. [31] numerically investigate internal cooling in turbine blades using truncated-root ribs to improve heat transfer efficiency. Using Reynolds-Averaged Navier-

Stokes (RANS) simulations, results show that truncated-root ribs increase Nusselt number by 8.56% at  $Re = 37,392$  and improve thermal performance by 39.24% at  $Re = 53,697$  compared to squared ribs. The findings confirm truncated-root ribs as a superior cooling strategy for turbine blade internal cooling. Mhetras et al. [47] experimentally evaluated heat transfer and pressure loss in a high aspect ratio cooling channel with ribbed and dimpled surfaces at high Reynolds numbers (up to  $1.4 \times 10^6$ ). The ribbed configuration (Case 4) achieved the highest heat transfer enhancement ratio of nearly 2.0, though it also exhibited the largest friction factor. Dimpled configurations (Cases 1, 2, and 3) showed consistent performance, with Case 2 which is smaller dimples, offering slightly better heat transfer and pressure drop. The thermal performance for all cases approached unity as Reynolds number increased. Additionally, the presence of a turbulated wall improved heat transfer even on the opposite smooth side, and both local and average heat transfer results showed good agreement, confirming the reliability of the measurements.

Labbé [48] conducted large-eddy simulations (LES) to analyze turbulent flow and heat transfer in a ribbed channel, accurately replicating experimental conditions. The LES captured complex unsteady phenomena such as shear layer separation and reattachment, vortex shedding, and secondary flows that strongly influence heat transfer distribution along ribbed surfaces. Vázquez and Métais [49] used LES to study turbulent flow in a square duct with and without wall heating. They found that heating one wall reduced turbulence near it by about 25%, while increasing it on the opposite wall by 30%. This changed the flow structure and heat transfer behavior, showing how thermal conditions affect turbulence. LES effectively captured these detailed flow changes. Patil and Tafti [50] also conducted large-eddy simulations (LES) with zonal near-wall treatment to analyze turbulent flow and heat transfer in a square ribbed duct. The simulations focused on configurations with rib height to hydraulic diameter ratios of 0.1 and 0.05, and rib pitch to rib height ratios of 10 and 20. The LES approach effectively captured complex flow structures, including separation and reattachment zones, which are critical for accurately predicting heat transfer enhancement and pressure drop in ribbed duct systems. While LES offers high-fidelity insights into flow behavior, it remains computationally expensive and time-consuming, making it impractical for most industrial applications where faster turnaround and lower resource consumption are critical. As a result, Reynolds-Averaged Navier–Stokes (RANS) models are often preferred in industry despite their lower resolution of turbulent structures. In the past, we have also worked on building and validating various experimental results focused

specifically on high Reynolds number flows using different RANS techniques [16,35]. Based on our experience, the  $k$ - $\epsilon$  family of models has proven to be the most effective in predicting heat transfer characteristics, as well as capturing flow separation and reattachment, while also being computationally less expensive.

Up to this point, various rib geometries and enhancement configurations have been extensively reviewed, along with the turbulence models commonly employed in commercial CFD software under a broad range of Reynolds number operating conditions relevant to industrial applications. Among the available Reynolds-Averaged Navier–Stokes (RANS) turbulence models, the  $k$ - $\epsilon$  and  $k$ - $\omega$  families are the most widely used. The  $k$ - $\omega$  models, particularly the Shear Stress Transport (SST) variant, are well-regarded for their superior capability in resolving near-wall turbulence and accurately predicting local heat transfer characteristics. However, this increased fidelity comes at the cost of significantly higher computational demands, particularly for high Reynolds number flows. Given that the present study focuses on extremely high Reynolds number conditions ( $Re = 100,000$  to  $600,000$ ), representative of mid-core passage cooling in gas turbine blades under atmospheric, scaled experimental conditions, it is essential to strike a balance between predictive accuracy and computational efficiency. To this end, the Realizable  $k$ - $\epsilon$  turbulence model was selected due to its favorable numerical stability, improved convergence behavior, and demonstrated accuracy in predicting complex flow behavior in high-speed internal cooling flows. Moreover, to further improve the model’s predictive capability, several enhancements were introduced. The Realizable  $k$ - $\epsilon$  model offers better performance in capturing non-equilibrium flow phenomena, such as flow separation and reattachment, which are critical in ribbed cooling channels. In particular, the sharp leading edges of the rib geometries studied here induce flow divergence and generate secondary vortices that interact with the side walls and subsequently reattach downstream. These effects result in complex three-dimensional corner flow structures, which are especially significant in geometries with sharp transitions such as ribs and fins. Accurate prediction of these interactions is essential for evaluating the true thermal-hydraulic performance of the system. The use of the Realizable  $k$ - $\epsilon$  model, therefore, provides a practical yet robust computational approach for guiding and complementing future experimental investigations in rib-roughened turbine blade cooling channels.

In line with this modeling strategy, the present study aims to evaluate the thermal-hydraulic performance of three distinct surface feature configurations –  $30^\circ$  angled Continuous Chevron

Pattern Fins (CCPF), V-shaped Double Broken Ribs (VSDBR), and Broken Chevron Pattern Fins (BCPF)—within a single-pass internal cooling channel through high-fidelity numerical simulations. Although V-shaped ribs at various angles of attack have been extensively investigated in the context of turbine blade internal cooling, the literature provides limited insights into the flow and heat transfer characteristics of more complex, non-traditional rib geometries such as those explored in this study. The experiments have been carried out for the V Shaped broken rib case to validate the numerical model against the experimental data on Reynolds number range from 100,000 to 400,000. To the best of the authors' knowledge, comprehensive analyses focusing on these geometries under extremely high Reynolds number conditions (100,000 to 600,000) are scarce – particularly for scaled atmospheric simulations representative of real turbine mid-core passages, even when modeled using advanced RANS techniques. In such high Reynolds number regimes, the boundary layer becomes exceedingly thin, and baseline convective heat transfer rates are already elevated, which makes further enhancement difficult without incurring substantial frictional losses. Therefore, this study does not limit its scope to heat transfer augmentation alone, but also thoroughly examines the frictional losses associated with each configuration. This dual consideration is critical for achieving practical and meaningful improvements in thermal-hydraulic performance for real-world gas turbine cooling applications. Through this investigation, the study contributes new insights into the design of advanced rib and fin turbulator configurations tailored for high-speed, high-performance internal cooling systems.

## **2. Numerical Method and Computational Setup**

### ***2.1. Computational domain and explanation***

The computational domain replicates the experimental setup detailed in our previous study, where the test section has a total length of 6 hydraulic diameters ( $6D_h$ ), followed by an outlet length of  $3D_h$ . The hydraulic diameter ( $D_h$ ) of the rectangular duct is uniformly maintained at 4 inches and all feature height to hydraulic diameter ratio have been maintained at  $e/D_h = 1/15$ . The first cooling feature is positioned 4 inches downstream from the inlet to ensure fully developed flow before interaction.

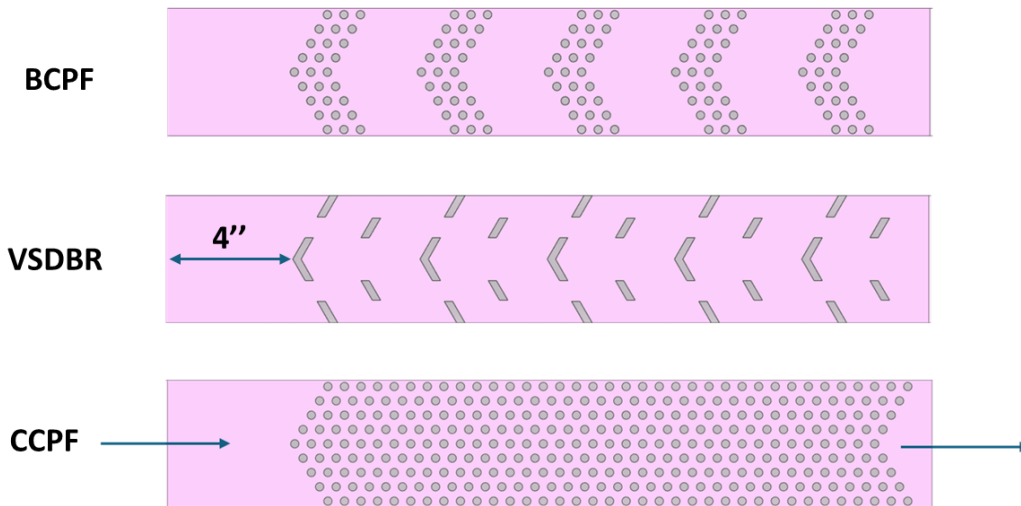


Figure 32: Feature configuration

Three geometric configurations were described in Figure 32. Continuous Chevron Pattern Fins (CCPF), configuration employs cylindrical fins arranged at a  $30^\circ$  angle of attack relative to the flow direction. The fins are placed with a pitch of  $2e$  and a streamwise spacing of  $2e$ , where  $e$  denotes the fin (or features in general) height. A total of 36 rows of fins are distributed uniformly along the entire test section in the bottom wall, aiming to induce turbulence and enhance convective heat transfer. Then after, V-shaped Double Broken Ribs (VSDBR) features broken V-shaped ribs placed at a  $30^\circ$  angle of attack, with each rib having a width equal to its height and a rib length three times its height. The pitch ( $p$ ) – defined as the distance from the leading edge of one V-shape to the next – is maintained at 4 inches. Additionally, smaller broken ribs are strategically inserted between the V-shaped ribs to intensify swirl, promote fluid mixing, and improve heat transfer. A total of five discrete broken V-shaped ribs are included in the test section. This configuration is designed to maximize turbulence and thermal performance while attempting to mitigate pressure loss typically associated with taller rib structures. Finally, Broken Chevron Pattern Fins (BCPF) case, V-shaped chevron fin arrays are incorporated at a  $30^\circ$  angle of attack as an alternative to discrete traditional V shaped ribs. The intent is to retain favorable mixing characteristics while improving pressure loss recovery at high Reynolds numbers. The spacing between adjacent fins is kept at  $2e$ , and three repeating fins form a single discrete unit. The pitch between successive chevron arrays (distance in between two single discrete unit) is set to 4 inches, consistent with Geometry 2. Each array contains three rows of chevron fins, mimicking the effect

of rib-induced roughness but with a more distributed structure to reduce flow resistance. These configurations were designed to study the influence of geometry on thermal-hydraulic performance under realistic gas turbine internal cooling conditions, especially at extremely High Reynolds numbers.

## ***2.2. Turbulence modelling and approach***

This section presents a high-fidelity RANS-based CFD simulation framework to analyze turbulent flow and heat transfer in rib-roughened ducts, focusing on non-traditional internal cooling features relevant to high Reynolds number applications. To achieve a balance between accuracy and computational efficiency, the Realizable  $k-\epsilon$  turbulence model was employed in conjunction with a non-equilibrium wall function and curvature correction adaptation. The  $k-\epsilon$  turbulence model family is well-recognized for its ability to predict separated and reattaching flows, making it particularly suitable for the current investigation of single-pass, heated ducts under forced convection conditions [18][16]. Complementing this choice, simulations were conducted using ANSYS Fluent v2024 R2 with a pressure-based SIMPLEC algorithm for pressure-velocity coupling.

Boundary conditions were defined with a velocity and room temperature inlet (corresponding to Reynolds numbers ranging from 100,000 to 400,000), zero-gauge pressure outlet, constant 5 KW/m<sup>2</sup> heat flux on the bottom wall and rib surfaces with no-slip conditions, and adiabatic, no-slip conditions on all other walls. The numerical setup was validated through experimental results for Variable Spacing Discrete Broken Ribs (VSDBR), ensuring the reliability of the model across the studied Reynolds number range. Convergence was established when residuals fell below  $10^{-5}$  for continuity, momentum, and turbulence transport equations, and  $10^{-8}$  for the energy equation. Additionally, average bottom wall temperature was monitored to ensure steady-state heat transfer was achieved, reinforcing the robustness of the simulation methodology in capturing complex flow and thermal behavior.

## ***2.3. Meshing & Boundary conditions***

To ensure a balance between computational cost and solution accuracy, and complexity of geometry, meshing was performed using ANSYS Fluent Meshing. In this study, only the fluid domain was meshed. The Body of Influence feature was applied to control mesh refinement within the test section, allowing for finer mesh near critical regions based on geometry. A high-quality

unstructured poly-hexcore mesh was used, suitable for the internal flow characteristics. Since the flow is predominantly axial and occurs at room temperature, this mesh type ensures both computational efficiency and accuracy. Inflation layers were applied to the bottom wall, the top surfaces of the features, and the side walls to resolve near-wall gradients more accurately. The computational mesh employed in this study is illustrated in Figure 33. Specifically, 12 to 15 inflation layers were generated to capture flow separation, reattachment, and wall shear effects phenomena critical for predicting local heat transfer. To maintain mesh continuity, the shared topology function was used, which ensures smooth transitions and avoids mismatches between adjacent cells. A higher mesh density was specifically maintained near the bottom wall and around rib or fin structures, using appropriate sizing functions within the Body of Influence zone. The same meshing approach and sizing strategy were consistently applied to all geometric configurations to ensure fair comparisons and uniform grid quality across different simulation cases.

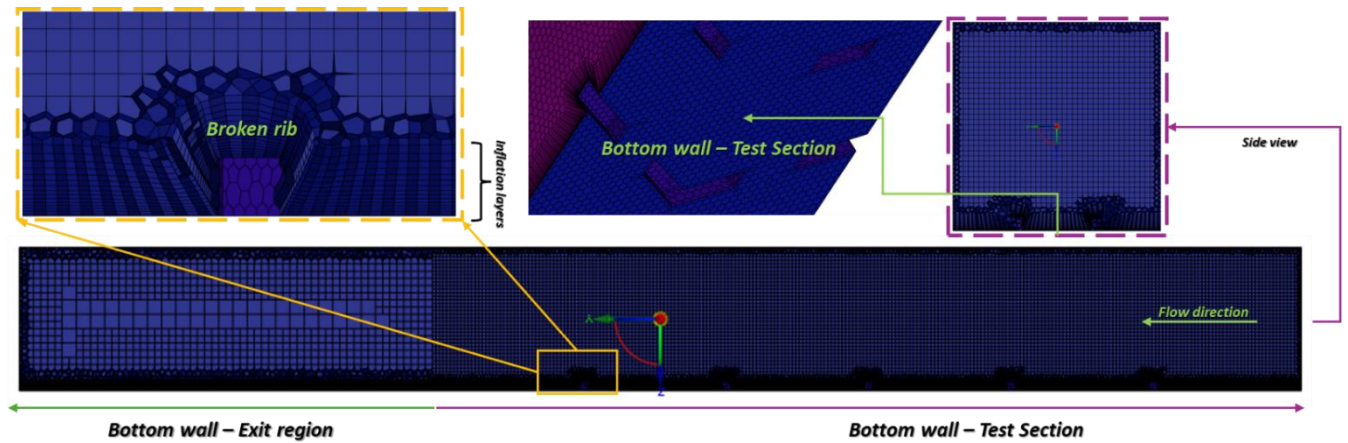


Figure 33: Computational mesh used for this study

#### ***2.4. Definitions and Data Reduction for Thermal, Flow, and Performance Parameter***

This section provides a detailed overview of the calculations used to determine the various properties essential for evaluating heat transfer, friction, and overall thermal-hydraulic performance of the different geometrical features examined in this study. The experimental measurement procedures, along with associated uncertainties and error margins, have been

thoroughly reported in chapter 2 and are therefore not reiterated here. Instead, this section focuses on the simulation data, which were obtained using post-processing equations specifically applied for the present numerical study. First, the flow's axial-averaged velocity was estimated based on the Reynolds number, which ranges from 100,000 to 600,000 – covering the entire incompressible regime (up to Mach  $\sim 0.26$ ) for the laboratory-scaled representation of a turbine blade mid-core passage. The local heat transfer coefficient was computed using Equation 18, utilizing the known heat flux ( $q''$ ), the local bulk fluid temperature ( $T_\infty$ ) and the wall temperature ( $T_{wall}$ ), which were obtained from the numerical methodology. The local bulk fluid temperature was derived using linear interpolation across the spanwise direction within the square channel in mid plane inside the duct.

$$h = \frac{q''}{(T_{wall} - T_\infty)} \quad (1)$$

Subsequently, the Nusselt number was calculated using Equation 19. The thermal conductivity of air was determined at the film temperature  $T_f = 0.5 (T_{wall} + T_\infty)$ .

$$Nu = \frac{h D_h}{k} \quad (2)$$

To evaluate the overall thermal performance, the computed Nusselt number was normalized using the Nusselt number for fully developed turbulent flow in a smooth circular tube, based on the Dittus-Boelter correlation, as shown in Equation 20. The normalized Nusselt number, calculated using Equation 21, was then used to assess the thermal performance of the ribbed internal cooling passage.

$$Nu_0 = 0.023 Re^{0.8} Pr^{0.4} \quad (3)$$

$$\frac{Nu}{Nu_0} = \frac{h D_h}{k \times 0.023 Re^{0.8} Pr^{0.4}} \quad (4)$$

The baseline frictional losses were determined using the Blasius equation, as expressed in Equation 22. The total pressure drops across the test channel, used to obtain the friction factor, was

calculated according to Equation 23. This friction factor was then normalized with the baseline friction loss, as provided in Equation 24.

$$f_0 = 0.079 Re^{-0.25} \quad (5)$$

$$f = \frac{\Delta P D_h}{2 \rho u^2 L} \quad (6)$$

$$\frac{f}{f_0} = \frac{\Delta P D_h}{2 \rho u^2 L (0.079 Re^{-0.25})} \quad (7)$$

Finally, the thermal hydraulic performance (THP) of the system was evaluated using Equation 25, providing a comprehensive measure of the heat transfer enhancement relative to the pressure losses within the cooling passage. The temperature distribution was normalized by determining the ratio of the wall temperature to the fluid inlet temperature, as described in Equation 26. This normalization allows for a dimensionless evaluation of the temperature distribution, facilitating consistent comparison across various configurations and operating conditions.

$$THP = \frac{Nu}{Nu_0} \left( \frac{f}{f_0} \right)^{1/3} \quad (8)$$

## **2.5. Mesh Independence test and model validation**

### **2.5.1. Mesh independence test**

To evaluate mesh independence, the VSDBR (V-shaped Double Broken Rib) configuration was selected, as this geometry was also validated against experimental data. Achieving mesh independence requires systematic refinement by adjusting the minimum and maximum element sizes. A series of mesh independence tests were conducted, the results of which are illustrated in Figure 34. The grid independence study was performed at a Reynolds number of 400,000, representing the highest flow condition investigated experimentally. Six different mesh densities were analyzed, with total element counts approximately 0.5M, 0.68M, 0.71M, 0.76M, 0.8M, and

0.9M for the VSDBR configuration. The area-averaged Nusselt number over the region of interest exhibited minimal variation across these mesh sizes, indicating weak dependence on grid resolution. Specifically, when refining the grid from 0.71M to 0.8M elements, the normalized Nusselt number increased only slightly from 2.14 to 2.15, corresponding to an overall percentage deviation of 0.47% and that data also has been presented in Table 4. This confirms the adequacy of the selected mesh resolution. Therefore, to ensure a practical compromise between computational accuracy and efficiency, the medium-density mesh (0.71M elements) was adopted for all subsequent simulations.

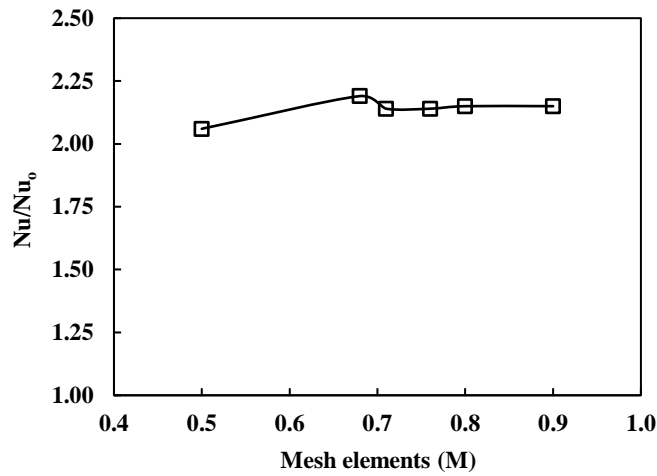


Figure 34: Grid Independent test

Table 4: Mesh parameters

| Sr # | Mesh Elements in M | Normalized Nu (Nu/Nu <sub>o</sub> ) |
|------|--------------------|-------------------------------------|
| 1    | 0.5                | 2.06                                |
| 2    | 0.68               | 2.19                                |
| 3    | 0.71               | 2.14                                |
| 4    | 0.76               | 2.14                                |
| 5    | 0.8                | 2.15                                |
| 6    | 0.9                | 2.15                                |

### 2.5.2. Validation with experimental data

In this section a normalized Nusselt number has been validated from CFD data against experimental results as well as pressure drop for the 100,000 to 400,000 Reynolds number condition.

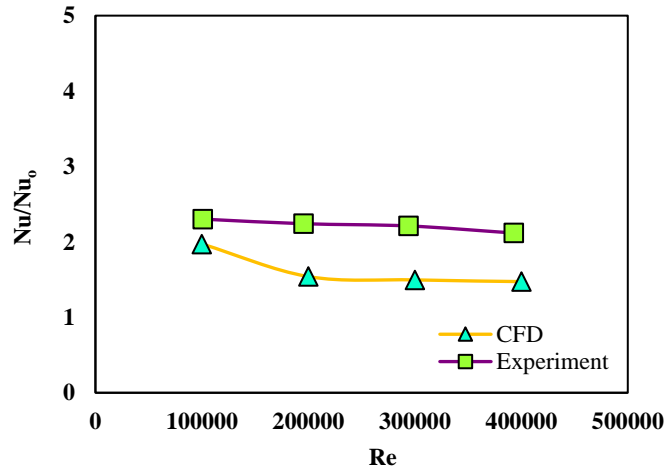


Figure 35: Comparison of Numerically Predicted Normalized Nusselt Number with Experimental Data for VSDBR features

Figure 35 presents the normalized Nusselt numbers for the VSDBR configuration at Reynolds numbers of 100853, 195300, 294034 and, 392919 for experimental condition and 100k to 400k for CFD. Additionally, the spanwise-averaged data for the VSDBR rig is presented in Figure 36. The comparison shows an overall agreement in trends between the numerical and experimental results. While the CFD simulation effectively captures the trend of the normalized Nusselt number across various Reynolds numbers, it slightly underpredicts the values at higher Reynolds number conditions. The underprediction of the normalized Nusselt number can be attributed to certain simplifying assumptions made in the numerical model. Firstly, the simulations were conducted under a steady-state framework with a constant wall heat flux applied as the thermal boundary condition. This approach does not fully capture the transient thermal behavior and complex flow dynamics present in the actual physical system. Secondly, adiabatic wall conditions were assumed, thereby neglecting any heat losses across the boundaries, which may further contribute to the deviation from experimental observations.

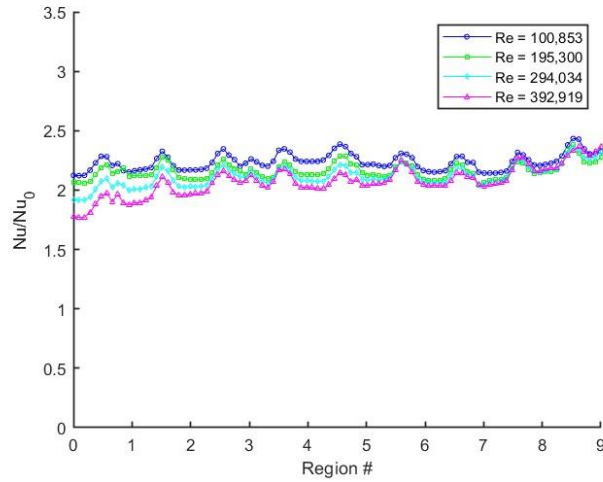


Figure 36: Experimental data for Spanwise averaging of normalized Nusselt number for VSDBR features.

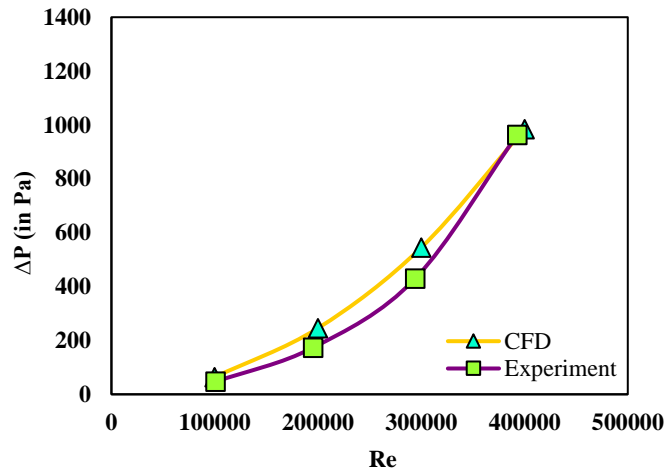


Figure 37: Evaluation of pressure drop: Experimental measurements vs. numerical predictions

Figure 37 presents the comparison between numerically predicted and experimentally measured pressure drops. The computational results show good agreement with the experimental data and can capture the trend too as the CFD is slightly above predicting frictional losses. The average percentage difference of approximately 30.65%. This level of agreement demonstrates the reliability of the numerical model in capturing the overall pressure loss characteristics, while also highlighting areas where further refinement may improve predictive accuracy.

### 3. Results and Discussion

#### 3.1. Heat transfer characteristics

This section particularly attributes the heat transfer characteristics on different Reynolds numbers.

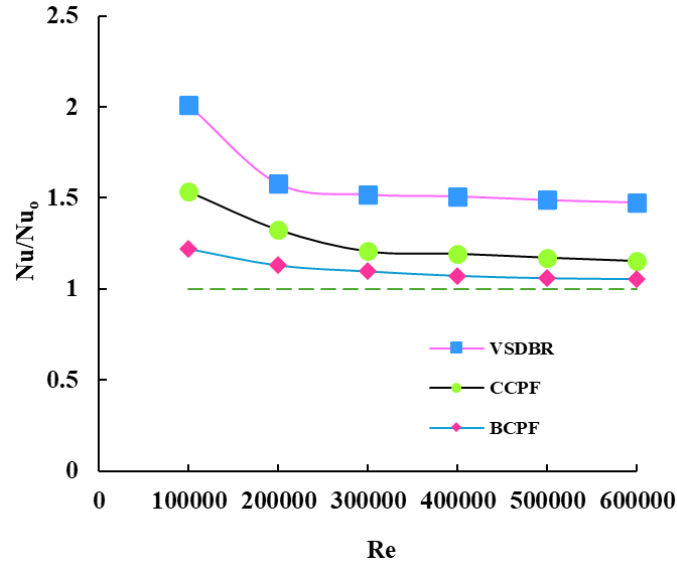


Figure 38: Normalized Nusselt number as a function of different Reynolds number.

As illustrated in Figure 38, the trend of the normalized Nusselt number demonstrates a clear reduction with increasing Reynolds number across all tested configurations. This behavior is particularly pronounced in the low Reynolds number regime, aligning with existing literature on transitional flow characteristics. The thickening of the thermal boundary layer at higher Reynolds numbers reduces the convective heat transfer capability, resulting in a noticeable decline in normalized heat transfer performance. Notably, a steep drop in augmentation occurs between Reynolds numbers of 100,000 and 200,000, beyond which the decrease becomes more gradual and approximately linear, indicating that at higher Reynolds numbers, the heat transfer enhancement becomes less sensitive to surface geometry variations.

Quantitative analysis reveals a normalized Nusselt number reduction of 26.87% for the VSDBR configuration, 25.32% for the CCPF configuration, and 13.11% for the BCPF configuration, over the Reynolds number range of 100,000 to 600,000. These results suggest that while the VSDBR configuration achieves the highest overall heat transfer enhancement in the examined range, the BCPF configuration is more effective in sustaining heat transfer augmentation

at extreme high Reynolds numbers. This performance highlights the robustness of discrete broken-fin designs in maintaining thermal performance across a broader range of flow conditions. In terms of recovering the heat transfer augmentation while VSDBR ribs work best in terms of achieving highest heat transfer enhancement on this Reynolds number range from 100k to 600k.

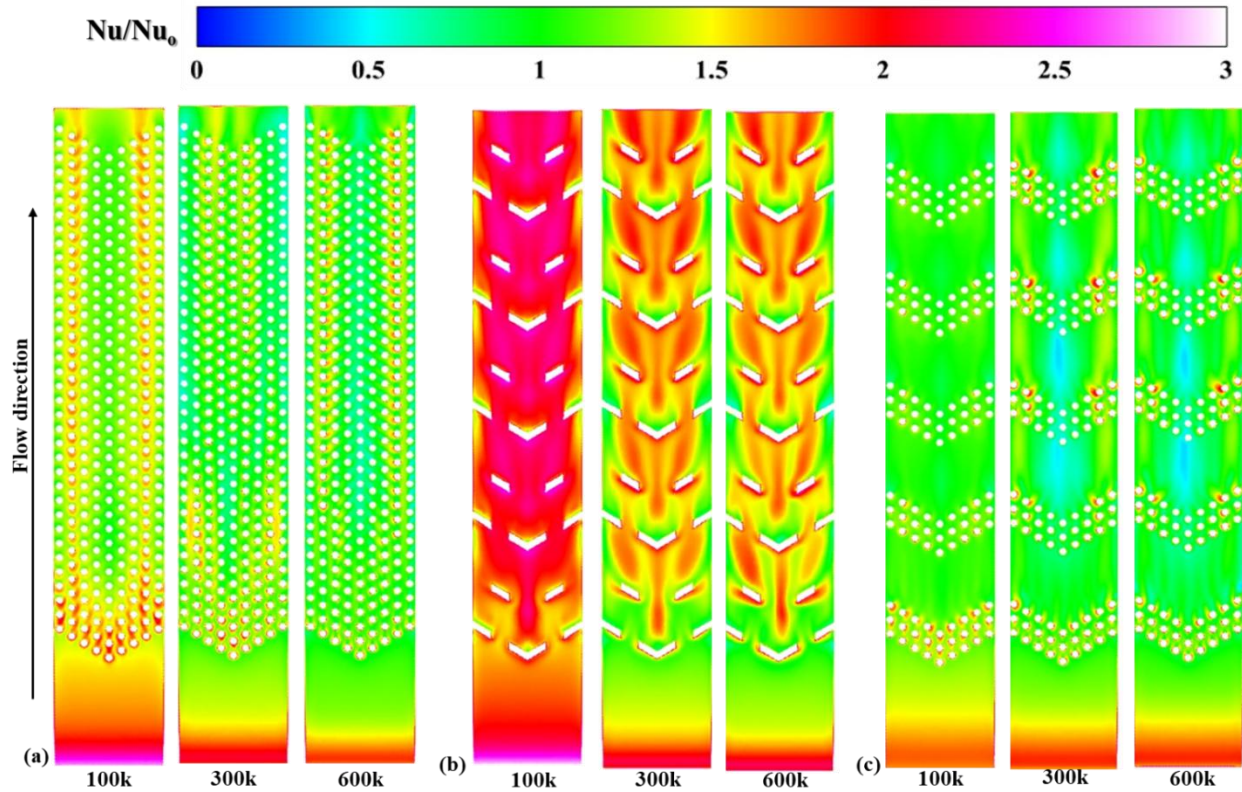


Figure 39: Normalized Nusselt number contours for (a) CCPF (b) VSDBR (c) BCPF design for three different Reynolds numbers.

Figure 39 presents the normalized Nusselt number contours for three representative Reynolds numbers: 100,000, 300,000, and 600,000. The Nusselt numbers depicted here are obtained through numerical simulations and subsequently normalized using the Dittus-Boelter correlation, which provides an empirical benchmark for fully developed turbulent flow in smooth channels. This normalization facilitates a consistent comparison of heat transfer augmentation across various geometric configurations and flow conditions. For the VSDBR configuration, the maximum heat transfer enhancement is observed further downstream, beyond the initial rib structures. This delayed peak in performance is attributed to the broken and staggered features,

which induce localized turbulence and secondary flows developing more effectively downstream. In contrast, both the CCPF and BCPF configurations exhibit a more uniform distribution of the normalized Nusselt number along the wall, reflecting steadier thermal behavior across the span.

In the VSDBR configuration specifically, the Nusselt number contours are skewed toward the downstream region immediately following the V-shaped ribs, with pronounced enhancement concentrated near the mid-span. However, regions near the corners and sidewalls experience comparatively lower heat transfer due to the absence of strong impingement or vortex-driven transport in these areas. Notably, the flow near the ribbed surface tends to migrate from the inner wall toward the outer wall, aligned with the direction of the ribs. As a result, the heat transfer enhancement in the inter-rib region gradually decays in the spanwise direction, moving from the inner to the outer wall.

While the contours offer qualitative insight into local heat transfer distributions, a more comprehensive understanding is obtained through the accompanying quantitative analysis, which presents the spanwise-averaged normalized Nusselt number as a function of Reynolds number in Figure 40. This integrated analysis approach provides both detailed local features and global trends in thermal performance for each tested configuration. Spanwise-averaged analysis reveals that geometrically periodic features induce periodic distributions in the Nusselt number indicating a strong coupling between surface topology and thermal transport. Across all cases, these periodic patterns become fully developed by the end of region# 3, signifying the establishment of stable flow and thermal fields downstream. Notably, the ribs demonstrate similar trends across all tested Reynolds numbers, suggesting a consistent flow response regardless of the flow regime. For all features tested in this study a substantial boost in normalized Nusselt number is observed at  $Re=100,00$  followed by a smoothing effect downstream. Additional but smaller enhancements are recorded at  $Re=300,000$  and  $600,000$  respectively. In contrast, the BCPF also exhibits a periodic heat transfer pattern, albeit with lower amplitude at  $Re=100,000$ . The trend persists at higher Reynolds numbers, although the magnitude of the enhancement is comparatively diminished. These findings underscore the influence of surface periodicity on thermal performance and its dependence on Reynolds number.

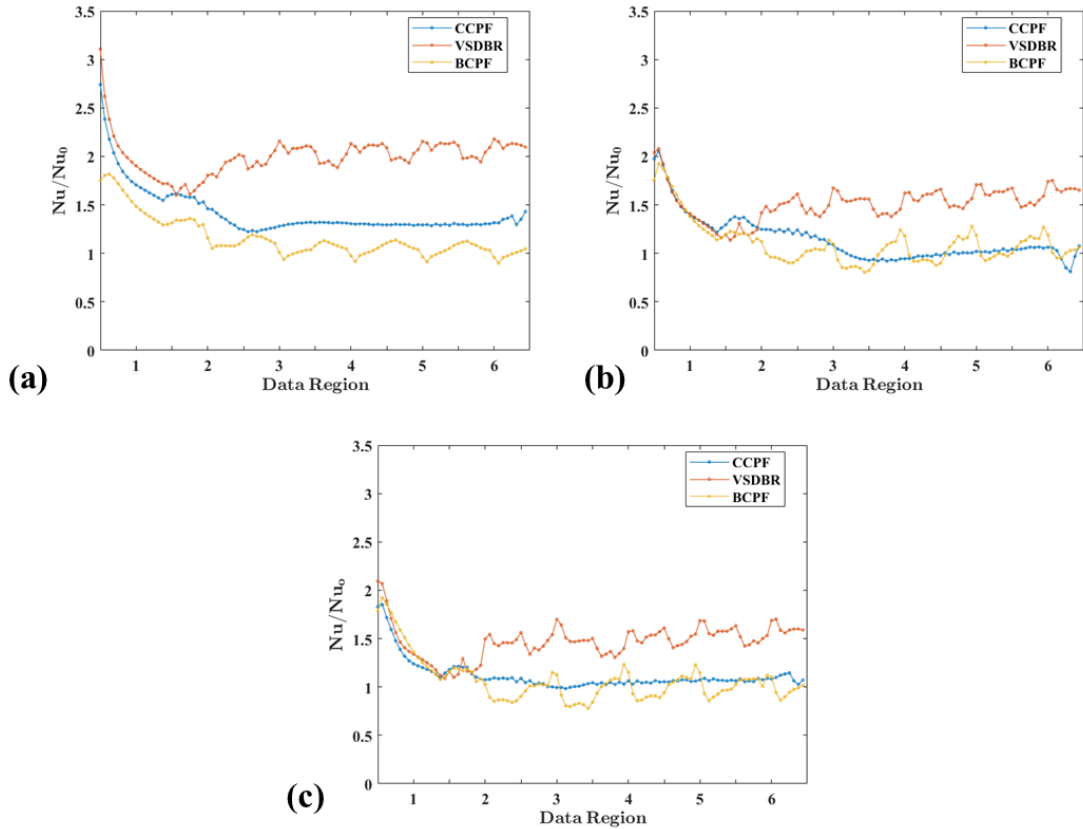


Figure 40: Normalized Nusselt number comparison for three different features tested on (1) 100k, (b) 300k and (c) 600k Reynolds number comparison

To gain deeper insights into the flow physics and mixing characteristics, four distinct cross-sectional planes were analyzed within the final one-third of the test section. These planes were evenly spaced along the region of interest. The corresponding figure Figure 41, Figure 42, Figure 43 presents velocity contours across three different channel configurations – namely, VSDBR, CCPF, and BCPF – at various streamwise positions and Reynolds numbers. A consistent color scale is used to represent velocity magnitude, with red indicating high velocities and blue representing near-zero flow regions (no slip boundary condition).

In the top row, corresponding to upstream locations, all configurations exhibit relatively uniform core flows which show the CCPF configuration. However, near-wall velocity gradients are notably pronounced in the CCPF configuration due to the presence of continuous surface ribs. The middle row, which depicts the VSDBR configuration, reveals significant core distortion and velocity redistribution, especially within the central region of the channel. This configuration is characterized by strong secondary flows and local acceleration near the channel centerline,

indicative of intensified mixing and spanwise momentum transport. These effects are particularly visible near mid-span and are largely absent in the CCPF and BCPF cases, which maintain more symmetrical and less disrupted velocity profiles.

### 3.2. Flow physics and characteristics

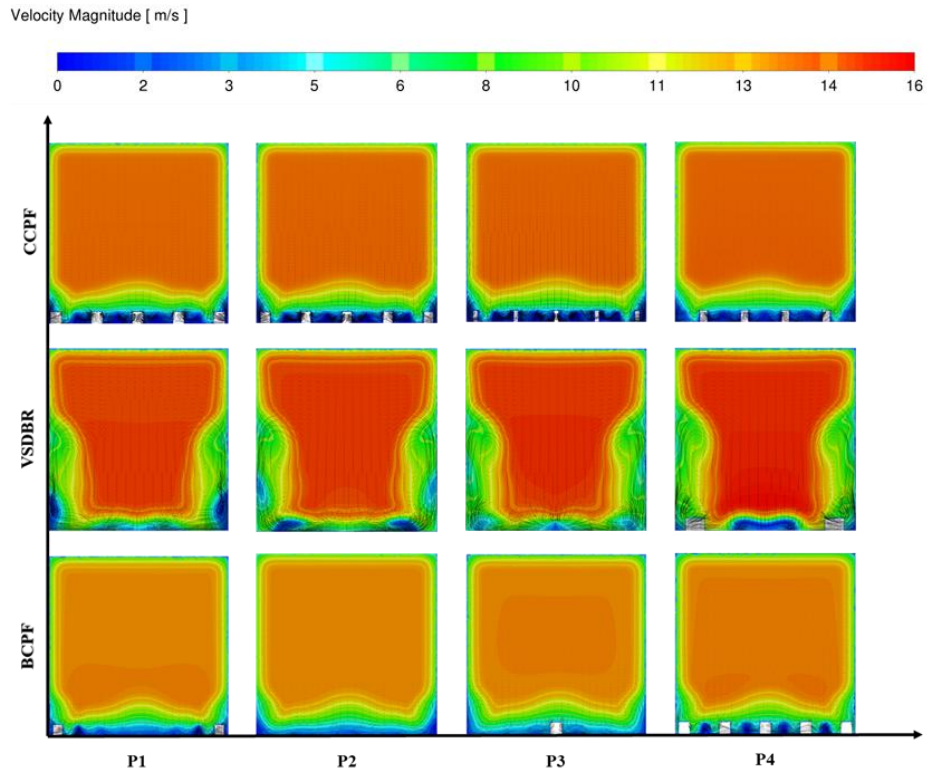


Figure 41: Flow path and velocity distribution on different featured geometry on  $Re = 100k$ .

The VSDBR features placed on a mid-row further accentuates these distinctions, showing that this configuration generates stronger spanwise gradients and corner recirculation zones, whereas the BCPF configuration sustains a more stabilized and uniform core flow. Overall, the figure underscores the role of rib geometry in shaping internal flow development, turbulence intensity, and flow uniformity in ribbed cooling channels. Among the tested designs, the VSDBR configuration produces the most vigorous recirculation, vortex formation, and swirling motion, at any tested Reynolds numbers compared to two other designs. These enhanced characteristics are primarily responsible for the superior thermal performance observed with VSDBR geometry.

It is also evident that in the VSDBR configuration, corner flow vortices progressively develop along the sidewalls and extend upward toward the top wall as the Reynolds number increases from 100,000 to 600,000. This observation suggests that the disrupted rib features not only enhance heat transfer on the bottom wall but also contribute to systematic boundary layer breakdown along the sidewalls. This effect is particularly attributed to the periodic arrangement of the surface features, which promotes a repeating flow disturbance pattern. The growth of large vortices extending nearly to the top wall in the VSDBR case strongly indicates that placing similar rib features on both the top and bottom surfaces – a common practice in cooling turbine blade mid-core regions – could further improve fluid mixing and thermal performance within the channel passage.

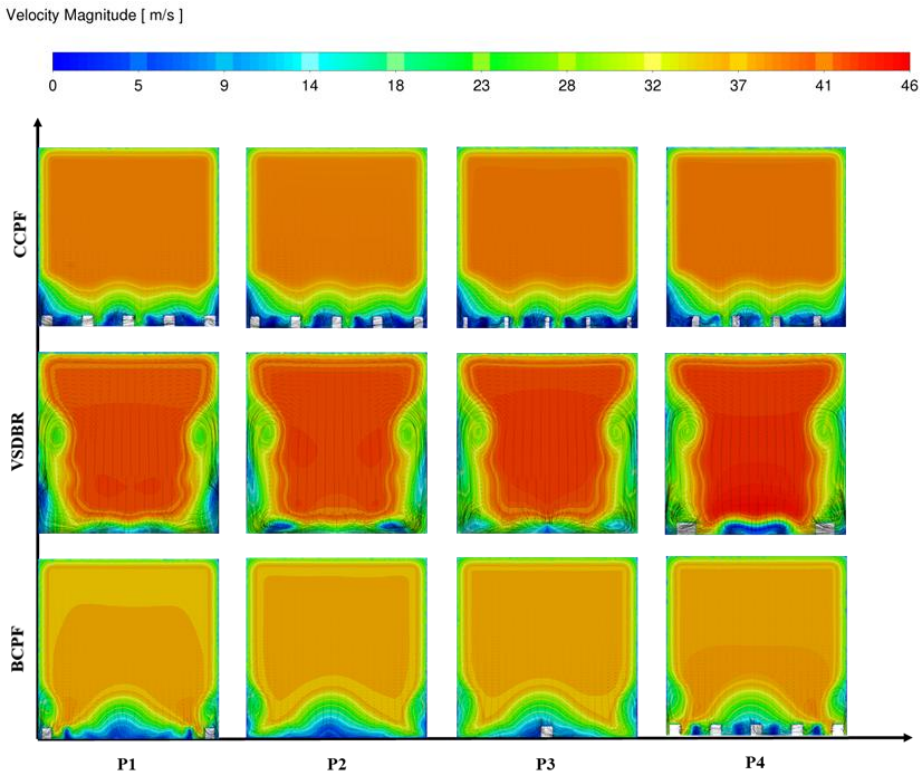


Figure 42: Flow path and velocity distribution on different featured geometry on Re = 300k.

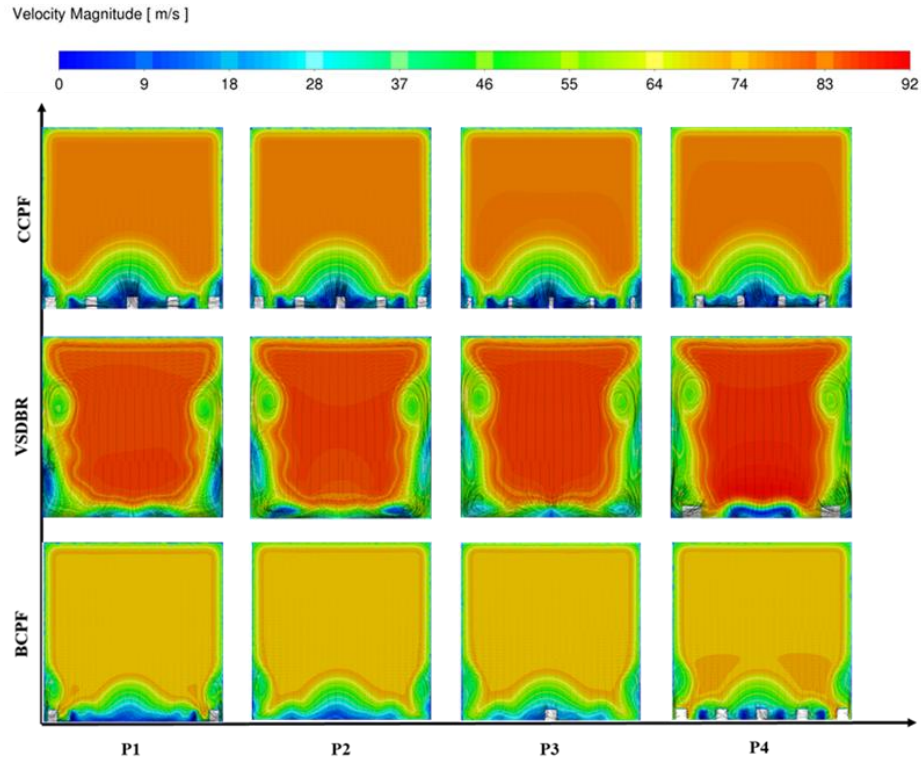


Figure 43: Flow path and velocity distribution on different featured geometry on  $Re = 600k$ .

### 3.3. Frictional performance

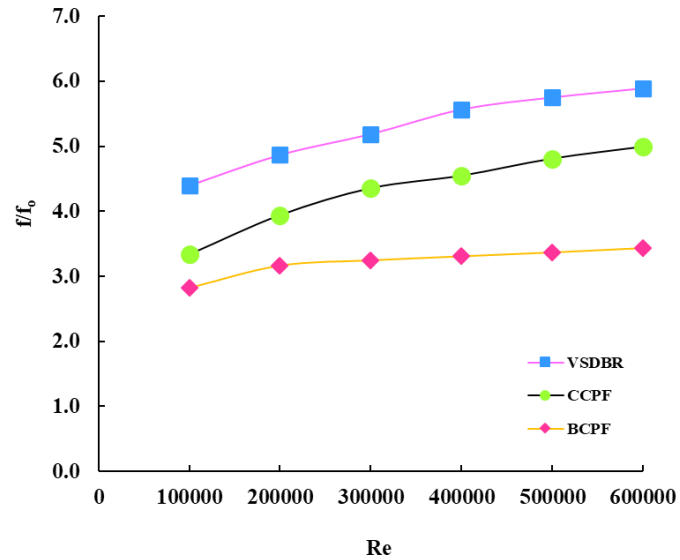


Figure 44: frictional losses (normalized friction) as a function of Reynolds number for three different tested geometry

### 3.4. Overall performance

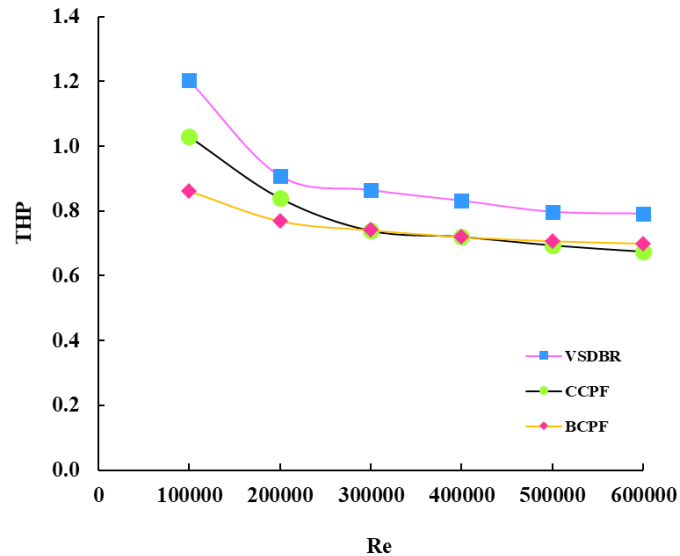


Figure 45: Thermal hydraulic performance for the tested design on a wide range of Reynolds number conditions

However, it is important to recognize that the enhanced vortex formation and improved mixing behavior associated with certain rib geometries come at the cost of increased pressure losses. As a result, a balance must be struck between thermal performance improvements and the accompanying frictional penalties. This trade-off is particularly crucial for mid-core cooling applications in turbine engines, where the available pressure margin is limited, and typically only 10–15% of bypass air is available for internal cooling. While the VSDBR configuration provides superior heat transfer enhancement, on another note as evidenced in Figure 44, it also incurs the highest pressure drop among the three configurations analyzed. In contrast, both fin-based configurations (CCPF and BCPF) exhibit lower frictional penalties. Specifically, the BCPF configuration demonstrates a minimal and nearly linear increase in pressure drop over the Reynolds number range from 100,000 to 600,000. Quantitative results indicate that the pressure losses increased by 34.09% for VSDBR, 51.52% for CCPF, and only 21.55% for BCPF within the same Reynolds number range going from 100,000 to 600,000. These findings reveal that while VSDBR offers the greatest heat transfer enhancement across a wide Reynolds number spectrum, it does so at the highest frictional cost. Conversely, BCPF is the most efficient from a frictional standpoint, followed by VSDBR and then CCPF features.

The high frictional growth observed in the CCPF configuration suggests that continuous fin arrays may not be suitable for high Reynolds number operating conditions. The trade-off between heat transfer augmentation and frictional losses becomes unfavorable, particularly when the entire wall is covered with uninterrupted rib structures. This underscores the importance of optimizing fin distribution based on parametric and thermal-hydraulic performance analysis rather than implementing full-surface coverage.

As illustrated in Figure 45, the thermal hydraulic performance (THP) drops below unity across all configurations as the Reynolds number increases beyond 200,000. Several factors may explain this trend. Firstly, as noted in the validation section, the computational fluid dynamics (CFD) model employed in this study tends to underpredict heat transfer nature, suggesting that the actual THP values could be higher in experimental conditions. Nevertheless, the CFD model offers a reliable comparative framework to assess the relative performance of different geometries under high Reynolds number conditions.

Interestingly, while the BCPF configuration underperforms in the lower Reynolds number regime, it exhibits improved THP compared to CCPF in the 400,000 to 600,000 range. This is likely due to its more favorable flow reattachment behavior. Unlike the fully covered CCPF design, the BCPF configuration leaves sections of the wall exposed, allowing for boundary layer reattachment and stabilization downstream. In high Reynolds number regimes, where the flow becomes increasingly less dependent on surface-induced augmentation, the spacing and periodic placement of features become critical. Therefore, the BCPF design proves advantageous in enabling reattachment zones, whereas the CCPF's continuous coverage prevents such recovery, ultimately hindering its thermal-hydraulic efficiency.

The thermal-hydraulic performance (THP) decreases consistently with increasing Reynolds number across all investigated configurations. This observation confirms two important aspects. First, it aligns with previously published findings in the literature, which demonstrate that THP tends to decline even in lower Reynolds number regimes due to the diminishing relative benefits of turbulence-induced heat transfer augmentation. Second, and more critically, at the extremely high Reynolds numbers considered in this study, achieving high heat transfer performance becomes increasingly challenging. At such conditions, the baseline convective heat transfer is already substantial due to the dominant flow momentum, which limits the relative impact of artificial enhancement mechanisms.

Consequently, the ability to significantly improve THP at high Reynolds numbers is constrained by the growing frictional losses associated with surface modifications and tripping the velocity boundary layer near wall. In such scenarios, even minor increases in pressure drop can outweigh the benefits of thermal enhancement. As a result, careful optimization is required to ensure that the trade-off between improved heat transfer and the associated pressure penalty remains favorable. This underscores the importance of designing flow-enhancing features that maximize mixing and thermal augmentation without incurring excessive friction losses, especially in high-speed internal cooling applications where pressure margins are limited.

#### 4. Conclusion

- VSDBR features exhibits the highest heat transfer enhancement ( $Nu/Nu_0 \approx 2.43$  at  $Re = 100,000$ ) due to strong secondary flows and intense recirculation, but it incurs the greatest frictional penalty (34.09% increase), making it suitable where thermal augmentation is prioritized over pressure efficiency.
- BCPF demonstrates the best thermal-hydraulic balance, showing only a 21.55% rise in frictional loss from  $Re = 100k$  to  $600k$ , while sustaining  $THP > 1$  at high Reynolds numbers, indicating its superior efficiency in extreme flow conditions.
- CCPF provides good heat transfer at lower  $Re$ , but perform badly by 51.52% friction growth and poor reattachment due to continuous blockage at high  $Re$ , making it less viable for ultra-high-speed internal cooling systems.
- Flow field and contour analysis confirm that geometric breaks, such as in VSDBR and BCPF, promote vortex formation and boundary layer reattachment, enhancing heat transfer uniformity. These findings are backed by mesh-independent CFD simulations with  $< 0.5\%$  deviation, ensuring high numerical accuracy.

## REFERENCES

- [1] S. Han, J. C., Dutta, S., and Ekkad, Gas Turbine Heat Transfer and Cooling Technology, Secodn Edi, CRC Press, Boca Raton, FL., 2012.
- [2] J.C. Han, Y.M. Zhang, High performance heat transfer ducts with parallel broken and V-shaped broken ribs, *Int. J. Heat Mass Transf.* 35 (1992) 513–523. [https://doi.org/10.1016/0017-9310\(92\)90286-2](https://doi.org/10.1016/0017-9310(92)90286-2).
- [3] S. V. Ekkad, J.C. Han, Detailed heat transfer distributions in two-pass square channels with rib turbulators, *Int. J. Heat Mass Transf.* 40 (1997) 2525–2537. [https://doi.org/10.1016/S0017-9310\(96\)00318-3](https://doi.org/10.1016/S0017-9310(96)00318-3).
- [4] R. Kamali, A.R. Binesh, The importance of rib shape effects on the local heat transfer and flow friction characteristics of square ducts with ribbed internal surfaces, *Int. Commun. Heat Mass Transf.* 35 (2008) 1032–1040. <https://doi.org/10.1016/j.icheatmasstransfer.2008.04.012>.
- [5] A.P. Rallabandi, H. Yang, J.C. Han, Heat transfer and pressure drop correlations for square Channels with 45 deg ribs at high Reynolds numbers, *J. Heat Transfer.* 131 (2009) 1–10. <https://doi.org/10.1115/1.3090818>.
- [6] T. Alam, R.P. Saini, J.S. Saini, Use of turbulators for heat transfer augmentation in an air duct - A review, *Renew. Energy.* 62 (2014) 689–715. <https://doi.org/10.1016/j.renene.2013.08.024>.
- [7] S. Baek, D. Kook, C. Kim, M. Bang, W. Hwang, Investigation of the relationship between the 3D flow structure and surface heat transfer within a realistic gas turbine blade trailing edge internal serpentine cooling channel, *Int. J. Heat Mass Transf.* 198 (2022) 123357. <https://doi.org/10.1016/j.ijheatmasstransfer.2022.123357>.
- [8] A.P. Rallabandi, N. Alkhamis, J.C. Han, Heat transfer and pressure drop measurements for a square channel with 45 deg round-edged ribs at high reynolds numbers, *J. Turbomach.* 133 (2011) 1–10. <https://doi.org/10.1115/1.4001243>.
- [9] A. Rallabandi, J. Lei, J.C. Han, S. Azad, C.P. Lee, Heat transfer measurements in rotating blade-shape serpentine coolant passage with Ribbed Walls at high reynolds numbers, *J. Turbomach.* 136 (2014) 1–9. <https://doi.org/10.1115/1.4026945>.
- [10] P. Singh, Y. Ji, S. V. Ekkad, Experimental and numerical investigation of heat and fluid flow in a square duct featuring criss-cross rib patterns, *Appl. Therm. Eng.* 128 (2018) 415–

425. <https://doi.org/10.1016/j.applthermaleng.2017.09.036>.
- [11] P. Singh, B.V. Ravi, S. V. Ekkad, Experimental and numerical study of heat transfer due to developing flow in a two-pass rib roughened square duct, *Int. J. Heat Mass Transf.* 102 (2016) 1245–1256. <https://doi.org/10.1016/j.ijheatmasstransfer.2016.07.015>.
- [12] B.V. Ravi, P. Singh, S. V. Ekkad, Numerical investigation of turbulent flow and heat transfer in two-pass ribbed channels, *Int. J. Therm. Sci.* 112 (2017) 31–43. <https://doi.org/10.1016/j.ijthermalsci.2016.09.034>.
- [13] A. Berber, M. Gürdal, Estimation of forced heat convection in a rectangular channel with curved-winglet vortex generator: A machine learning approach, *Therm. Sci. Eng. Prog.* 37 (2023) 101563. <https://doi.org/10.1016/j.tsep.2022.101563>.
- [14] M. Zhang, P. Singh, S. V. Ekkad, Rib Turbulator Heat Transfer Enhancements at Very High Reynolds Numbers, *J. Therm. Sci. Eng. Appl.* 11 (2019) 1–9. <https://doi.org/10.1115/1.4043465>.
- [15] J. Xing, S. Han, Y. Song, N. An, L. Zhou, L. Li, H. Zhang, X. Du, Improving internal cooling performance of turbine blade with steam in channel with rhombus-patterned biomimetic ribs: A numerical investigation, *Therm. Sci. Eng. Prog.* 40 (2023). <https://doi.org/10.1016/j.tsep.2023.101789>.
- [16] N. Pandya, S. V. Ekkad, Advanced Thermal Performance of Broken V-Shaped Ribs for Gas Turbine Blade Internal Cooling at High Reynolds Numbers, *AIAA SciTech Forum Expo. 2024.* (2024) 1–12. <https://doi.org/10.2514/6.2024-2759>.
- [17] I.L. Chen, I. Sahin, L.M. Wright, J.C. Han, R. Krewinkel, Heat Transfer in a Rotating, Blade-Shaped, Two-Pass Cooling Channel With Various 45-Deg Rib Orientations, *J. Therm. Sci. Eng. Appl.* 14 (2022) 1–14. <https://doi.org/10.1115/1.4053741>.
- [18] M. Maurer, J. von Wolfersdorf, M. Gritsch, An experimental and numerical study of heat transfer and pressure loss in a rectangular channel with v-shaped ribs, *J. Turbomach.* 129 (2007) 800–808. <https://doi.org/10.1115/1.2720507>.
- [19] I. V. Shevchuk, S.C. Jenkins, B. Weigand, J. Von Wolfersdorf, S.O. Neumann, M. Schnieder, Validation and analysis of numerical results for a varying aspect ratio two-pass internal cooling channel, *J. Heat Transfer.* 133 (2011). <https://doi.org/10.1115/1.4003080>.
- [20] F.R. Menter, R. Sechner, A. Matyushenko, Best Practice: RANS Turbulence Modeling in ANSYS CFD, (2021) 2–95. <https://www.ansys.com/resource-center/technical-paper/best->

practice-rans-turbulence-modeling-in-ansys-cfd.

- [21] A.S. Yadav, J.L. Bhagoria, Heat transfer and fluid flow analysis of solar air heater: A review of CFD approach, *Renew. Sustain. Energy Rev.* 23 (2013) 60–79. <https://doi.org/10.1016/j.rser.2013.02.035>.
- [22] V.K. Garg, Heat Transfer in Gas Turbines, Management. (2001) 42–44.
- [23] J.C. Han, J.S. Park, Developing heat transfer in rectangular channels with rib turbulators, *Int. J. Heat Mass Transf.* 31 (1988) 183–195. [https://doi.org/10.1016/0017-9310\(88\)90235-9](https://doi.org/10.1016/0017-9310(88)90235-9).
- [24] Y.M. Zhang, J.C. Han, J.A. Parsons, C.P. Lee, Surface heating effect on local heat transfer in a rotating two-pass square channel with 60° angled rib turbulators, *ASME 1993 Int. Gas Turbine Aeroengine Congr. Expo. GT 1993.* 3B (1993) 272–280. <https://doi.org/10.1115/93-GT-336>.
- [25] G.S. Azad, M.J. Uddin, J.C. Han, H.K. Moon, B. Glezer, Heat transfer in a two-pass rectangular rotating channel with 45-deg angleb rib turbulators, *J. Turbomach.* 124 (2002) 251–259. <https://doi.org/10.1115/1.1450569>.
- [26] P. Singh, Development of Advanced Internal Cooling Technologies for Gas Turbine Airfoils under Stationary and Rotating Conditions, (2017).
- [27] P. Singh, J. Pandit, S. V. Ekkad, Characterization of heat transfer enhancement and frictional losses in a two-pass square duct featuring unique combinations of rib turbulators and cylindrical dimples, *Int. J. Heat Mass Transf.* 106 (2017) 629–647. <https://doi.org/10.1016/j.ijheatmasstransfer.2016.09.037>.
- [28] P. Singh, S. Ekkad, Experimental study of heat transfer augmentation in a two-pass channel featuring V-shaped ribs and cylindrical dimples, *Appl. Therm. Eng.* 116 (2017) 205–216. <https://doi.org/10.1016/j.applthermaleng.2017.01.098>.
- [29] C. Thianpong, P. Promvongse, S. Skullong, P. Promthaisong, M.E. Nakhchi, Numerical heat transfer study of square duct equipped with novel flapped V-baffles, *Int. J. Therm. Sci.* 197 (2024) 108819. <https://doi.org/10.1016/j.ijthermalsci.2023.108819>.
- [30] B.X. Zhang, L.Q. Wang, W. Lu, J.H. Xu, Y.B. Wang, Y.R. Yang, X.D. Wang, Performance evaluation and enhancement of turbulent flow and convective heat transfer characteristics for turbine blade internal cooling, *Phys. Fluids.* 36 (2024). <https://doi.org/10.1063/5.0191021>.

- [31] C.T. Dinh, T.M. Nguyen, T.D. Vu, S.G. Park, Q.H. Nguyen, Numerical investigation of truncated-root rib on heat transfer performance of internal cooling turbine blades, *Phys. Fluids*. 33 (2021). <https://doi.org/10.1063/5.0054149>.
- [32] I.L. Chen, I. Sahin, L.M. Wright, J.C. Han, R. Krewinkel, Heat transfer in a rotating, two-pass, variable aspect ratio cooling channel with profiled v-shaped ribs, *J. Turbomach.* 143 (2021) 1–13. <https://doi.org/10.1115/1.4050447>.
- [33] A. Kumar, M. Pathak, Flow and heat transfer characteristics of gas turbine blade channels with compound V-rib-dimple structures, *Int. Commun. Heat Mass Transf.* 157 (2024) 107823. <https://doi.org/10.1016/j.icheatmasstransfer.2024.107823>.
- [34] X. Fang, Z. Yang, B.C. Wang, M.F. Tachie, D.J. Bergstrom, Large-eddy simulation of turbulent flow and structures in a square duct roughened with perpendicular and V-shaped ribs, *Phys. Fluids*. 29 (2017). <https://doi.org/10.1063/1.4985715>.
- [35] N. Pandya, S. V Ekkad, HIGH-PERFORMANCE BROKEN RIBS AND RIBS WITH FINS FOR HIGH REYNOLDS, (2024) 1–10.
- [36] J.-C. Han, L.M. Wright, *Experimental Methods in Heat Transfer and Fluid Mechanics*, CRC Press, 2020. <https://doi.org/10.1201/9781003021179>.
- [37] R.J. Moffat, Using uncertainty analysis in the planning of an experiment, *J. Fluids Eng. Trans. ASME*. 107 (1985) 173–178. <https://doi.org/10.1115/1.3242452>.
- [38] M.E. Taslim, T. Li, D.M. Kercher, Darryl E. Metzger Memorial Session Paper: Experimental Heat Transfer and Friction in Channels Roughened With Angled, V-Shaped, and Discrete Ribs on Two Opposite Walls, *J. Turbomach.* 118 (1996) 20–28. <https://doi.org/10.1115/1.2836602>.
- [39] A. Kumar, R.P. Saini, J.S. Saini, Heat and fluid flow characteristics of roughened solar air heater ducts - A review, *Renew. Energy*. 47 (2012) 77–94. <https://doi.org/10.1016/j.renene.2012.04.001>.
- [40] H. Yan, Z. Chen, F. Zeng, L. Luo, W. Du, L. Guo, Flow and heat transfer characteristics of a return-flow impingement cooling scheme with varied target surface curvature for turbine blade leading edge, *Appl. Therm. Eng.* 254 (2024) 123904. <https://doi.org/10.1016/j.applthermaleng.2024.123904>.
- [41] L. Wang, C. Lv, X. Liu, J. Mao, D. Zhang, Y. Liu, M. Li, Research on improving heat transfer performance by using wavy ribs with different cross sections, *Appl. Therm. Eng.*

- 257 (2024) 124397. <https://doi.org/10.1016/j.applthermaleng.2024.124397>.
- [42] Y. Jia, Y. Liu, H. Xing, Z. Meng, W. Yin, S. Zhao, Experimental and numerical investigations on film cooling performances with spiral-channel holes for a turbine vane, *Appl. Therm. Eng.* 256 (2024) 124124. <https://doi.org/10.1016/j.applthermaleng.2024.124124>.
- [43] P. Promvong, S. Sripattanapipat, C. Thianpong, S. Skullong, P. Promthaisong, M.E. Nakhchi, Enhanced thermal effectiveness of square duct with V-type double-baffles: Numerical study, *Int. Commun. Heat Mass Transf.* 157 (2024) 107727. <https://doi.org/10.1016/j.icheatmasstransfer.2024.107727>.
- [44] J. Luo, A. Alghamdi, F. Aldawi, H. Moria, A. Mouldi, H. Loukil, A.F. Deifalla, S.P. Ghoushchi, Thermal-frictional behavior of new special shape twisted tape and helical coiled wire turbulators in engine heat exchangers system, *Case Stud. Therm. Eng.* 53 (2024) 103877. <https://doi.org/10.1016/j.csite.2023.103877>.
- [45] A. Srivastav, R. Maithani, S. Sharma, Investigation of heat transfer and friction characteristics of solar air heater through an array of submerged impinging jets, *Renew. Energy.* 227 (2024) 120588. <https://doi.org/10.1016/j.renene.2024.120588>.
- [46] R. Zhang, Z. Xiang, S. Han, X. Huang, L. Zhou, L. Li, H. Zhang, X. Du, Numerical study of the film cooling effectiveness and flow loss of a shark-skin-inspired composite structure, *Int. J. Therm. Sci.* 204 (2024). <https://doi.org/10.1016/j.ijthermalsci.2024.109248>.
- [47] S. Mhetras, J.C. Han, M. Huth, Heat transfer and pressure loss measurements in a turbulated high aspect ratio channel with large reynolds number flows, *J. Therm. Sci. Eng. Appl.* 6 (2014). <https://doi.org/10.1115/1.4027299>.
- [48] O. Labbé, Large-eddy-simulation of flow and heat transfer in a ribbed duct, *Comput. Fluids.* 76 (2013) 23–32. <https://doi.org/10.1016/j.compfluid.2013.01.023>.
- [49] M.S. Vázquez, O. Métais, Large-eddy simulation of the turbulent flow through a heated square duct, *J. Fluid Mech.* 453 (2002) 201–238. <https://doi.org/10.1017/S0022112001006887>.
- [50] S. Patil, D. Tafti, Large-eddy simulation with zonal near wall treatment of flow and heat transfer in a ribbed duct for the internal cooling of turbine blades, *J. Turbomach.* 135 (2013) 1–11. <https://doi.org/10.1115/1.4006640>.

## **APPENDICES**

